Università degli studi di Milano
Facoltà di scienze Matematiche, Fisiche e Naturali
Dipartimento di Fisica
Corso di Laurea in Fisica

Laser apparatus for exciting Positronium in AEGIS Positronium spectroscopy experiment

UNIVERSITÀ DEGLI STUDI DI MILANO

Coordinator: Dr. Simone CIALDI

Advisor: Dr. Fabrizio CASTELLI

Master thesis of:
Ruggero CARAVITA
Serial number 790836

Academic Year 2011-2012

Table of contents

1 Introduction and motivation

One of the recent and most promising research avenues in physics is the antimatter research community's current effort to exploit achievements in producing and cooling down bunches of more than 10^7 antiprotons in the Antiproton Decelerator facility at CERN, in order to produce significant amounts of cold, neutral, antimatter atoms. As a result, systematic studies of the atomic-physics scale properties of antimatter, such as gravity or atomic spectrum, might be feasible.

The production of large quantities of cold, neutral, antimatter atoms to perform such studies is, indeed, an extremely complex task, mainly because of the difficulties of storing and handling antimatter. For instance, a typical electromagnetic Penning trap, suitable for antimatter storage, requires an ultra-high vacuum environment with an intense magnetic field and an overall temperature close to absolute zero. Critical working conditions like these (commonly found around the AD facility) can easily overwhelm even the most cutting-edge technologies and they require extremely sophisticated devices. With such constraints, it's imperative to reduce complexity as much as it can be, wherever possible.

The easiest-to-produce type of stable, atomic antimatter is, of course, antihydrogen, which happens to be the best choice for most experiments involved in producing cold antimatter (with the exception of the ASACUSA experiment[1], which is specifically working on producing antiprotonic helium). Moreover, antihydrogen is a practical test bench for probing matter/antimatter symmetry, since the energy levels and orbital functions can be analytically solved.

The original method for producing cold antihydrogen atoms, first developed during the ATHENA collaboration[2] and later improved by the ALPHA collaboration[3] and AEGIS collaboration[4], consists of establishing a particular configuration of electric and magnetic fields inside a Penning trap, in order to force a cloud of cold antiprotons and a bunch of positrons into the same space. The capture of positrons from the antiprotons inside the trap produces cold antihydrogen, which is kept inside the trap by a strong multipolar magnetic field coupled with antihydrogen atomic magnetic moment. The main drawback

---

[1] See [ASACUSA 2013]

[2] See [ATHENA 2013]

[3] See [ALPHA 2013]

[4] See [AEGIS 2013] and [AEGIS 2007]

of this method is its low rate of antihydrogen production due to the limited interaction cross-section between antiprotons and positrons.

Different approaches to producing neutral antihydrogen have been proposed in the last ten years by experiments in the AD facility seeking to increase antihydrogen production. One of the most promising, in terms of the amount of antihydrogen produced, is positron capture from an antiproton that interacts with a highly-excited Positronium atom. The main advantage of this approach is the production cross-section's dependence on the fourth power of n, the energy level of the excited Positronium. For instance, the interaction between antiprotons and highly excited Positronium at n = 20, would be $1.6 \cdot 10^5$ times more efficient than interaction with non-excited (n = 1) Positronium. This approach was chosen both by the AEGIS collaboration and by the newly-formed HBAR collaboration to produce bunches of cold antihydrogen for antimatter gravity-coupling measurements.

Since the task of exciting Positronium to high energy levels has not yet been accomplished, it became crucial to the AEGIS collaboration to study the production of highly excited Positronium separately in a dedicated experiment. This dedicated experiment, referred to from here on as the Positronium spectroscopy experiment, is meant to study the excitation of Ps to high energy (Rydberg) levels, outside the cryogenic and ultra-high-vacuum environment of the antihydrogen experiment, to gain control over the excitation mechanism. Ps excitation is accomplished by illumination with pulses of intense laser radiation produced by a wavelength-tunable optical system driven by a terawatt-scale, Q-Switched laser.

The goal of this work is to describe how the optical apparatus used in the AEGIS experiment to excite Positronium to high energy states was completed, tested and commissioned. The theory of Positronium excitation is reviewed in detail, as are the optical apparatus that was commissioned and the optical transport line built to carry laser radiation to the experimental region. Moreover, the intrinsic synchronization issues raised by the Q-Switched laser and the consequent planning and construction of a high-precision synchronization device to overcome these constraints are presented.

2 Overview of AEGIS experiment facility

2.1 Towards a theory of quantum gravity

The symmetry between matter and antimatter has been one of the most thoroughly verified strongholds of particle physics. Paul Dirac first suggested the existence of this different kind of matter, with exactly the same properties as matter except for its reversed charge, in his seminal 1928 work introducing the well-known Dirac equation [Dirac 1928]. The Dirac equation, a unification of quantum mechanics, electron spin, and special relativity, allowed both electrons (with negative charge) and anti-electrons (with positive charge) to exist simultaneously. This rather unexpected prediction from Dirac found experimental verification the following year by Dmitri Skobeltsyn, who first observed the anti-electron (or positron) in a Wilson cloud chamber [Close 2010].

The symmetry between matter and antimatter for a wide class of particles was carefully checked throughout the twentieth century, leading to the formulation of the Standard Model of particle physics, which incorporates CPT symmetry between matter and antimatter. It states that either a particle or an antiparticle can be switched to its opposite kind by applying three operators to its spin: charge conjugation (C), parity inversion (P), and time reversal (T).

CPT invariance of the Standard Model, however, is completely independent from the problem of gravitational interaction between matter and antimatter, because CPT invariance requires only that the inertial mass of a particle and that of its relative antiparticle be equal, since it is the only constant appearing in the free particle Dirac equation. It places no restrictions on gravitational mass, because no interaction terms are considered in the free-field equation. The coupling between antiparticles and a gravitational field generated by matter distribution (the Earth, for example) could even be repulsive without any evident contradiction of electrodynamics, as pointed out by [Villata 2011].

Despite the scientific importance of such a fundamental aspect of nature, even after more than fifty years of research into antimatter, no measurement of the coupling of antimatter with gravity has been performed. Two attempts were made, at Stanford and at CERN's Low-Energy Antiproton Ring, using beams of charged antimatter particles: the measurement of gravitational effect, however, was affected by overwhelming systematic errors, due to residual electric and magnetic fields. Only by using neutral antimatter, antihydrogen for instance, could antimatter gravity-coupling measurements be made with the required precision.

2.2 The AEGIS experiment

The AEGIS collaboration[5] was started in 2003 on the ashes of the ATHENA collaboration [6]. Its objective is to measure antimatter gravitational coupling for the first time. As of this writing, the collaboration counts 15 different research institutes with more than 50 active members. After nine years of commissioning, the experiment is finally underway, yielding its first results in trapping antiprotons and cooling them down.

The AEGIS experimental area is physically located at CERN, Geneva, in building 193 (commonly known as AD-HALL) where the Antiproton Decelerator resides. All experiments related to antimatter studies are connected to the AD via magnetic transfer lines and placed in the central area of the ring, which is more than 40 meters in diameter and covers the whole surface of the building (see Figure).

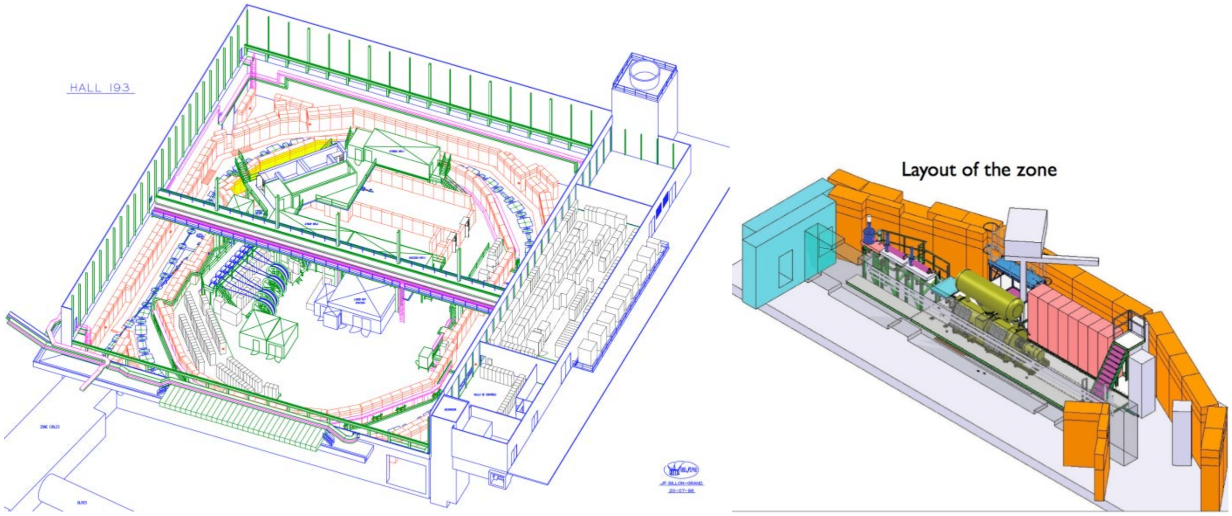

Figure 2-1: In the left image: overview of Antiproton Decelerator Hall; the decelerator elements are shown in blue outside the experimental regions in the middle of the hall and AEGIS experimental area is highlighted in yellow. In the right image: Layout of AEGIS zone as seen from the top floor of AD-HALL.

---

[5] See [AEGIS 2007] and [AEGIS 2013]

[6] See [ATHENA 2013]

The AEGIS experiment facility hosts two separate experiments, both of them physically built over the same transfer line from the Antiproton Decelerator. The main experiment focuses on measuring antihydrogen gravity acceleration (the antihydrogen experiment, from here on), while the secondary experiment is meant to study laser excitation of Positronium to highly excited states with spectroscopic techniques (the Positronium spectroscopy experiment, from now on).

The following paragraphs give a schematic overview of the experiment. Each primary part of the experiment will be outlined to provide insight into how the apparatus works. The apparatuses of greatest interest to us here are the positron apparatus and the laser apparatus. For these two parts, a more detailed description is given.

2.2.1 The antihydrogen experiment

The primary scientific goal of AEGIS is to exploit the availability of cold charged antiprotons coming from AD to produce a beam of cold antihydrogen. After this, the coupling of antihydrogen with Earth's gravitational field is determined by measuring the vertical displacement due to free fall after free horizonal propagation inside a vacuum beam pipe. The detection itself is carried out by a Moireé deflectometer.

Schematically, the steps to produce a beam of antihydrogen and measure its gravitational acceleration are the following:

1. Production and accumulation of positrons (e^+) from the decay of a radioactive ^{22}Na source;
2. Capture and accumulation of the antiproton beam coming from AD;
3. Cool-down of the antiprotons to fractions of Kelvin via electron-antiproton sympathetic cooling;
4. Production of thermalized (ortho-)Positronium (Ps) by implantation of positrons in the Positronium converter, a nanostructured porous silica target;
5. Two-step laser excitation of Positronium (Ps) to Rydberg states (Ps^*);
6. Formation of cold Rydberg antihydrogen ($\overline{H}^*$) via charged exchange of the e^+ between Positronium and antiprotons;

7. Acceleration of the resulting antihydrogen atoms with non-uniform electric fields coupling with the atomic electric dipole moment;
8. Measurement of vertical displacement due to gravitational acceleration into a Moireé deflectometer.

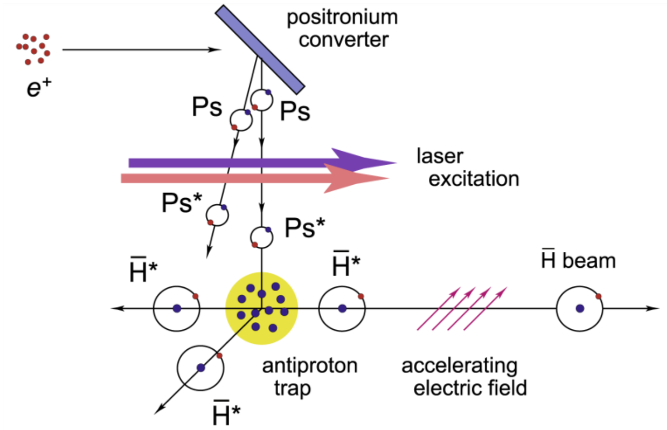

Figure 2-2: Antihydrogen production scheme in AEGIS experiment, courtesy of [Kellerbauer 2008]

2.2.2 The Positronium spectroscopy experiment

The main goal of the Positronium spectroscopy experiment is to excite Ps at Rydberg states with principal number $n > 23$ using the same two step laser excitation mechanism used in the previous experimental project.

This experiment acts like a workbench for studying Ps excitation in a simpler environment than the antihydrogen trap. Moreover Rydberg Ps excitation is of a paramount importance for studying atoms under the combined action of electric and magnetic fields, both external or induced. In fact, being Ps the most lighter atom known, the effects of induced motional Stark shifts are overwhelming over the others, deeply affecting the energy level structure.

In particular, here a new technique for exciting Ps to Rydberg levels will be applied, using the $1 \rightarrow 3$ transition followed by a $3 \rightarrow n > 20$ transition, instead of the $1 \rightarrow 2$ transition precedently exploited to produce Ps^*.

Schematically, the steps to produce Rydberg Ps are the following:

1. Production and accumulation of positrons (e^+) from the decay of a radioactive ^{22}Na source;
2. Production of thermalized (ortho-) Ps by implantation of positrons in the Positronium converter, a nanostructured porous silica target;
3. Two-step laser excitation of Ps to Rydberg states (Ps^*);
4. Ionization of the Ps cloud to measure the excited fraction.

Many innovative studies can be performed with the Ps apparatus online besides the measurement of the excited fraction of Ps. These include

- Reconstruction of the Time of Flight distributions of the Ps cloud;
- Measurement of the angular distribution of the Ps cloud emerging from the converter as a function of the geometrical structure of the nanoporous structure;
- Studies of the implantation and diffusion of positrons inside the converter;
- Studies of different nanoporous structures for the improvement of conversion efficiency;
- Laser cooling of excited Ps^*.

2.2.3 Organizing the experimental area

For the purpose of clarity, The AEGIS facility can be logically divided into three different regions:

1. The first region is shared between both experiments, and includes the positron source, the Positronium converter and the laser apparatus;
2. The second region includes the components needed exclusively by the spectroscopy experiment, and includes the positron accelerating transfer line and the experimental chamber;
3. The third region includes the components related to the antihydrogen experiment, and includes the antiproton beam line and two different trapping system: the first to catch and cool-down the antiprotons, the second to hold antiprotons in place while Ps is produced, excited and sent in the direction of the antiprotons.

The detailed technical drawings showing the organization of the experimental area can be found in appendix [DRAWING-1].

2.3 The shared components

Three different apparatuses are shared between both experiments:

1. the positron apparatus, including the radioactive ^{22}Na source, the positron trap and the positron accumulator;
2. the Positronium converter, consisting in a nanostructured silica foil with semi-regular nanometric pores;
3. the laser system to perform the two-step Positronium excitation to Rydberg levels.

2.3.1 Producing a collimated beam of positrons

Positrons are spontaneously produced by unstable isotopes incurring in β^+ decay. An effective choice for Positronium production is the isotope ^{22}Na, which has a relatively long half-life ($\tau = 2.6y$). The decay follow the reaction

$$^{22}Na \rightarrow {}^{22}Ne + e^+ + \nu_e \tag{2.1}$$

Typical sources used for positron production are in the order of 50 ÷ 100 mBq . Several commercial systems exist to produce a stable beam of positrons, the most common being the Surko-type used both by AEGIS and ALPHA experiments (the latter being inherithed from ATHENA experiment).

AEGIS positron source consists in a 1 cm in diameter, 50 mCi ^{22}Na tablet installed on a metallic support cooled down to 5.5 K via an helium-pump refrigerator (this component is often referred to as the *coldhead*). In front of the source, a parabolic cone is installed. A thin layer of frozen Neon is deposited on the cone surface, acting as a moderator for the outcoming positrons with energy of ~ 0.2 MeV.

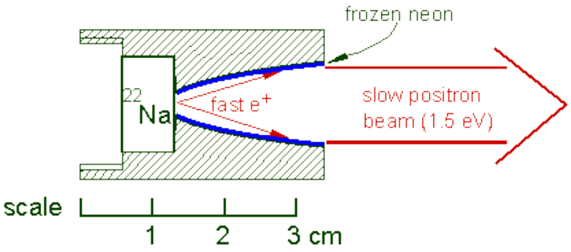

Figure 2-3: Scheme of the positron source element, courtesy of [UCSD 2013]

The resulting energy of the emerging positrons is approximatively 1.5 ± 1 eV, with a conversion efficiency of 0.1% with respect to the total amount of positrons emitted by the radioactive source. The positron beam is then conducted by a magnetic transfer line into the positron trap to be cooled down. The principle used for thermalizing the positrons is the energy loss by random collisions with inhert gas molecules (ordinary molecular nitrogen N_2). The trap is divided in three regions with decreasing pressure of cooling gas and decreasing electric potential to store the captured positrons in a well-like potential.

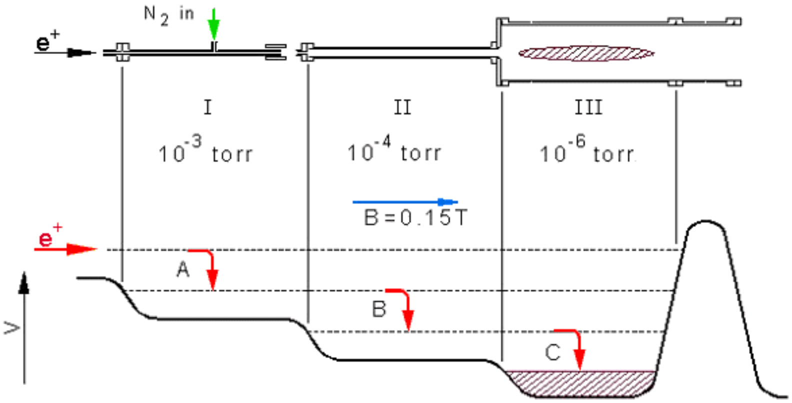

Figure 2-4: Reference design of the positron trapping element, courtesy of [UCSD 2013]

After the cool-down the positrons are moved to the accumulator, the last trapping region with very low pressure and high magnetic field where cold positrons are accumulated forming a non-neutral plasma. An electric rotating wall is placed inside the trap to shrink radially the positron plasma, thus reducing the fraction colliding and annihilating with the trap internal surface. The amount of stored positrons with such technique usually increases by a factor ~ 2 (see Figure 2-5).

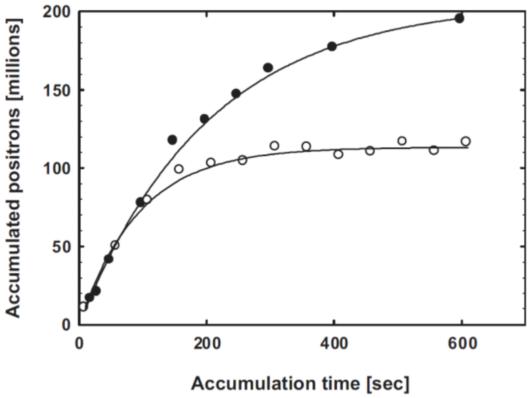

Figure 2-5: Accumulated positron number inside the accumulator as a function of accumulation time with the rotating wall enabled (black points) and disabled (white points). The use of the rotating wall to shrink the positron plasma increases the accumulation time by a factor 4 and the accumulated amount by a factor 2. The asymptotic value is reached in both conditions when the number of annihilating positrons per unit time equals the number of captured and cooled positrons.

With a magnetic field of 1.2 T and the rotating wall turned on, a maximum of ~ 120 s storage time has been achieved with $\sim 10^5$ positrons stored inside the accumulator.

After the period of accumulation, the accumulator is rapidly opened and the positrons extracted by applying a linear-increasing potential difference on the trap electrodes. A positron bunch is thus formed, ready to be transported by a magnetic transfer line towards the experimental region.

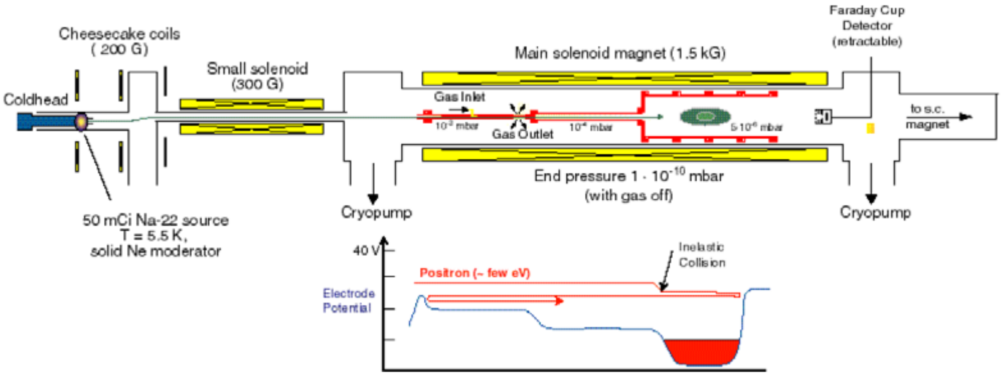

Figure 2-6: Schematics of AEGIS positron apparatus.

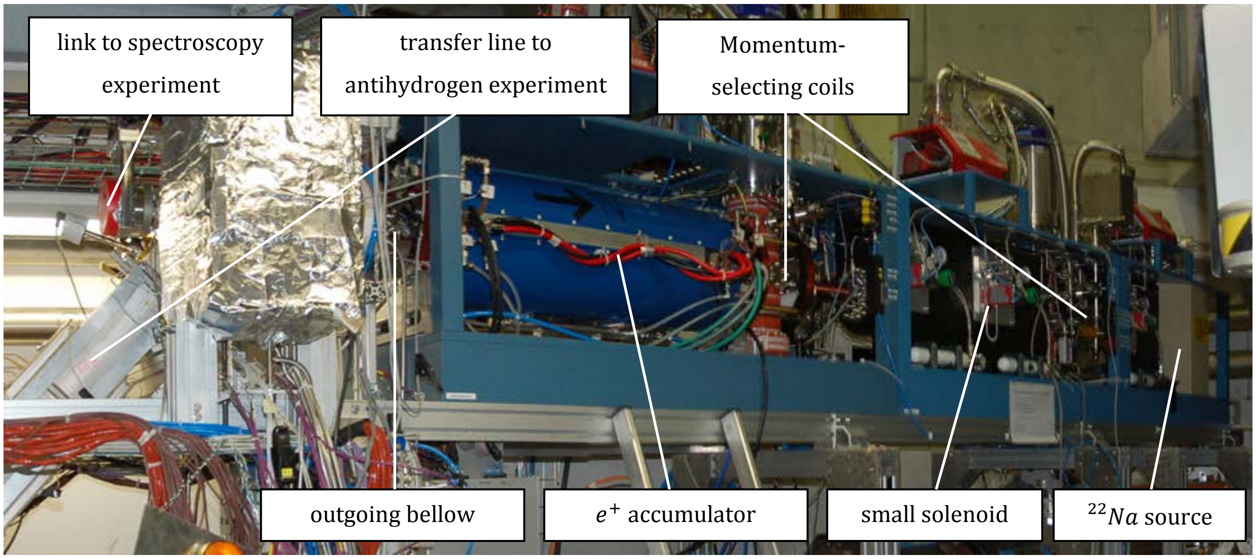

Figure 2-7: Photograph of AEGIS positron apparatus. Three separate elements are distinguishable: the coldhead with the momentum-selecting coils, the trap magnet and the accumulator magnet.

In Figure 2-7 a schematic of the current AEGIS positron apparatus is shown, together with a photograph of its current realization in the AEGIS zone.

2.3.2 Positronium production in nanostructured porous silica targets

Positronium is produced by a positron by electron capture within a material. Typically, insulators are preferred to metals and semiconductors, because the high free electron density shields the implantation process: most of the Ps produced from these materials is actually diffused from the first surface layers. Viceversa in insulators Positronium is usually formed in the bulk of the material; after formation, it diffuses to the surface and is released into vacuum.

Insulators offer the possibility of thermalizing the produced Positronium at the price of a lower production rate. If the insulating material is made porous, Ps will be preferably emitted into internal porosities rather than on the material surface, negligible with respect to the overall surface of the pores. Although some Positronium is lost because of pickoff annihilations with electrons on the walls of the pores, a significant fraction of the produced ortho-Ps bounces repeatedly on the pore surface without annihilating, progressively thermalizing itself with the material. If pores are made cylindrical in shape with an open end, Positronium can reach the surface of the material by climbing up in the pore.

After the extraction of the positron beam from the accumulator, a magnetic transfer line guides the bunch of positrons to the Positronium converter, in which a positron captures a free electron and forms a bound state, i.e. a Ps atom. In the case of both AEGIS experiments, the converter consists in a thin silicon layer, first made porous by electrochemical etching and after oxidized at high temperature. The virtues of such material for Positronium conversion have been thoroughly studied in [Mariazzi 2010 PRB].

The pores on the surface on average have a cylindrical structure of $\sim 5\ nm$ in diameter and $> 1\ \mu m$ length with non-flat internal surface. Positrons are accelerated by the transfer line to be implanted into the converter surface. Typical implantation energies spans between $0.1 \div 10$ keV depending on the needed implantatation depth to maximize the yield of the Positronium converter.

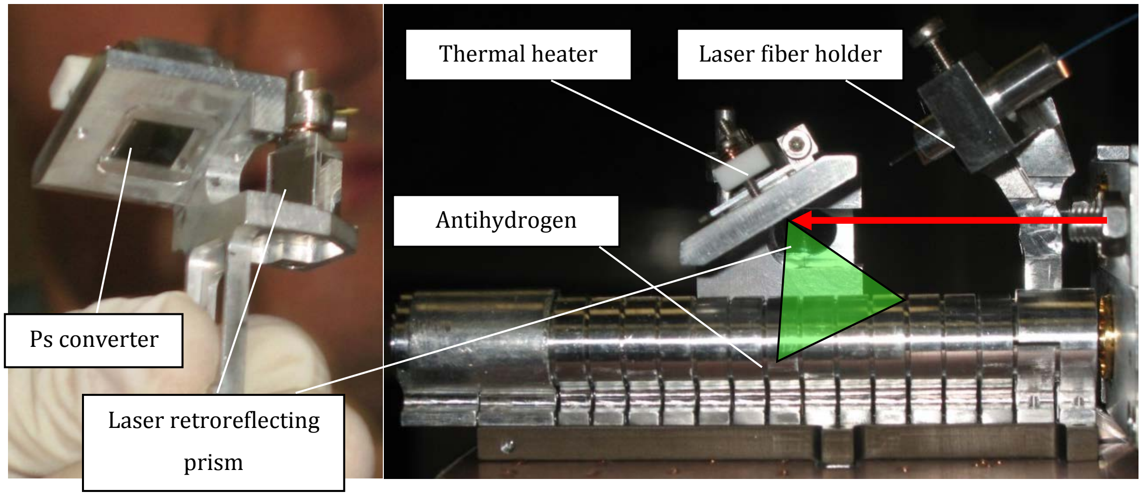

Figure 2-8: The Ps converter before being installed (left) and after being installed in the antihydrogen experiment above the antihydrogen formation trap with a fiber holder already in place (right). The positron beam coming out the launch trap on the right side is implanted in the Ps converter (red arrow) that diffuses Ps atoms in the direction of the antihydrogen trap (green cone). The distribution of emitted Ps from the converter has not been measured yet.

After implantation of the positron beam, Ps is formed on the internal surface of the pores with high momentum. The para-Ps fraction of the produced Ps annihilates in the very short time of $0.125\,ns$ and only the long-lived ortho-Ps fraction is relevant to the current experiments. Ortho-Ps atoms are produced at high temperature, then thermalize by frequent collisions with the hole walls and propagate in the pores reaching the surface. Finally, a cloud of Ps atoms emerges: a fraction of them has a Maxwellian velocity distribution centered on the converter temperature.

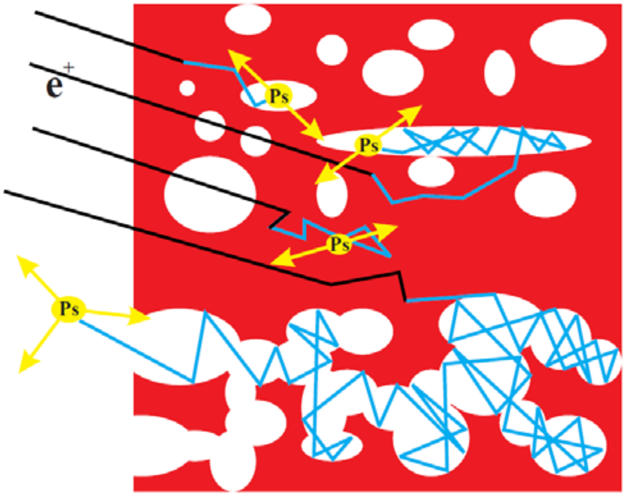

Figure 2-9: Scheme of Ps formation in porous silica targets, scourtesy of [Gidley 2006]

Empirical studies conducted by the Trento and Milano group shows that the best yields of thermalized Ps are obtained with 1 keV implantation energy, corresponding to ~25 nm implantation depth. In these conditions, the thermalized ortho-Ps fraction reaches 45% of the total ortho-Ps produced in the converter (see [Mariazzi 2010 PRB], [Mariazzi 2010 PRL]).

The main diagnostic tool to measure the implantation and production efficiency is a scintillating crystal placed close to the Positronium converter (CsI, PbF_2 and BaF_2 are the common choices, depending by the sensibility and the temporal resolution required by the measurement). It detects the γ rays caused by the spontaneous annihilation of the para-Positronium inside the converter via the reaction

$$\left(e^{+}+e^{-}\right)_{S=0} \rightarrow \gamma+\gamma \tag{2.2}$$

The signature of the produced γ rays is very sharp: in a $2 \to 2$ reaction the energies and momenta of the outgoing particles are constrained by the process cinematic. Each γ in the final state must carry half of the energy of the initial Ps, thus being produced at $511 keV$. Moreover, since para-Ps half-life is so short ($142\, ps$), within a very accurate approximation all para-Ps decays immediately after being produced, giving an important tool for determining the implantation depth of e^+, the amount of Ps produced and the precise timing of the implantation.

The amount of ortho-Ps produced can be reconstructed noticing that para-Ps and ortho-Ps are synthesized inside the converter in quantities proportional to the factors $1 / 4$ and $3 / 4$ respectively: measuring the total amount of annihilating para-Ps is a robust method to estimate the total amount of ortho-Ps produced inside the converter. By comparing this value with ortho-Ps decay measurements outside the converter, it's possible to calculate the fraction of ortho-Ps lost inside the converter and the *conversion efficiency*.

A more detailed discussion about Positronium production in porous silica targets is given in Chapter 4.

2.3.3 Excitation of Positronium to Rydberg levels

The excitation of Ps to Rydberg levels in the AEGIS experiment is by means of nanosecond laser pulses impinging the cloud exited from the Positronium converter. Exciting Ps with high efficiency directly from the ground state to Rydberg levels is above the present technological capabilities. It would require extremely deep UV radiation in the range of 180 − 185 nm, that is extremely difficult to realize with commercial equipment. Moreover, most of the available optical components, such as lenses and prisms, has high absorption rates for such wavelenghts.

A more effective solution implies two different pulses of laser radiation with different wavelengths shining contemporaneously on the Positronium. The first pulse excites Ps from the ground state to one of the first excited states (in the literature $n = 2$ is the most common choice, see for instance [Cassidy 2012]; for the present experiment we have chosen to work with $n = 3$ for the reasons discussed in [Castelli 2009]); the second gives a second kick to the excited Ps and carries out the transition to Rydberg levels. The theoretical analysis on Positronium excitation by laser pulses is given in Chapter 4

AEGIS laser equipment takes care of producing the two pulses to saturate the transitions $1 \rightarrow 3$ and $3 \rightarrow 20 \div 25$. The first pulse has wavelength of $205\ nm$, the second has wavelength in the range $1650 \div 1750\ nm$ depending on the target Rydberg state. The apparatus is physically placed on a laser table sideways of the trap region.

The laser system is composed by pulsed Q-Switched[7] Nd:YAG laser which has the role of a pump for the whole apparatus, and moreover performs second harmonic generation (SHG) and fourth harmonic generation (FHG). Then two separate optical systems perform a sequence of optical parametric generation (OPG), optical parametric amplification (OPA) and frequency sum to produce the right wavelengths and allow the user to modify at runtime the target Rydberg level. For a fully detailed description of the laser apparatus see Chapter 5.

After producing the requested wavelengths, a transport line takes care to carry the laser pulses to the experimental area. In the case of the spectroscopy experiment, the two pulses are superimposed and transported by the same optical system. Vice versa, in the antihydrogen experiment the two radiations follow different paths. The UV radiation is carried into the experiment via a prism optical line, while the IR radiation is transported via optical fibers. Moreover, a synchronization optical line is needed to adjust the delay introduced by index of refraction of the fiber, which is substantially different from the one of the vacuum.

The tuning of the laser system layout and the transport of the radiation pulses inside the experiments has been a matter of study and physical realization for the whole period of this thesis. The present work focuses (in Chapter 6) on the description of the laser transport line inside the spectroscopy experiment; for the description of the transport line inside the antihydrogen experiment, see [Cerchiari 2013].

---

[7] For an overview on Q-Switched lasers, see Chapter 3.

2.4 The antihydrogen experiment apparatus

The antihydrogen experiment is composed of a single cryostat containing two different high magnetic field regions: the 5 Tesla region, used to catch the antiprotons coming from AD, and the 1 Tesla region where the formation of antihydrogen is realized Each magnetic field is generated by a superconducting magnet cooled down by liquid helium to 5 K. Two different vacuum regions are distinguished in the cryostat: the insulation vacuum of $10^{-8}\ mbar$ in the outer region of the cryostat (the OVC) and the ultra-high vacuum vessel (the UHV) of $10^{-13}\ mbar$ in the internal experimental region.

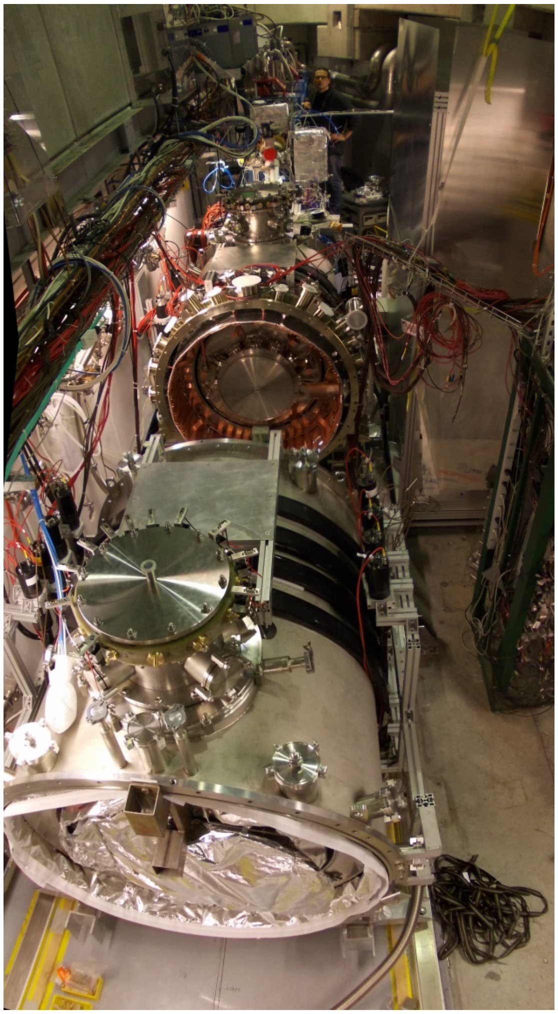

Figure 2-10: The AEGIS antihydrogen apparatus before the final assembly. The two regions of the cryostat are clearly distinguishable: the upper cylindrical apparatus is the 5T region (closer to AD beam line); the lower and separated cylindrical apparatus is the 1T region. Inside the connecting flange its visible an inner flange separating the OVC region to the UHV region.

2.4.1 Trapping the antiprotons, positrons, and antihydrogen

The preparation of antiprotons to produce antihydrogen consists of several steps that are performed in a sequence of traps starting from the beam line of AD and ending in the production region. See Figure 2-12 and [DRAWING 1] for a visual reference on the trapping system.

1. **5T catching trap:** the first trap is a Malberg-Penning cylindrical trap that captures the $5\,MeV$ antiproton beam from AD and the positron bunch from the positron transfer line. While positrons are directly transferred to the 1T region, antiprotons need to be cooled to a much lower temperature to be manageable: a titanium degrader is used to select a low energy fraction of the incoming antiprotons. Usually, 10^4 antiprotons are collected from the degrader. After the capture, electrons are injected in the central region of the trap to perform stochastic cooling of the antiprotons. The principle of stochastic cooling consists in transferring heat from antiprotons to electrons by collisions. These particles are used because they have the same electrical charge of antiprotons, hence avoiding annihilations. Since electrons have a 2000 times lower mass than antiprotons, they dissipate their heat via bremsstrahlung much more efficiently than antiprotons. With stochastic cooling, temperatures of few eV can be obtained within a few tenths of second.
2. **5T accumulation trap:** a second Penning trap is present in the 5T region to store the cooled antiprotons in order to collect a bunch with sufficient density to interact with the excited Positronium cloud. The antiproton cloud is squeezed radially by a rotating wall with the same technique used with the positron cloud in the accumulator.
3. **1T antiproton stopping trap:** the antiproton stopping trap is used to receive the antiproton bunch from the 5T accumulation trap and squeeze the cloud radius to fit into the antihydrogen formation trap.
4. **1T diocotron trap:** this trap is placed before the 1T antiproton stopping trap on the same beam axis. It is used to catch the positron beam received from the 5T region, and also to move the bunch off the beam axis to align it with the positron accumulation launch trap, that is placed vertically over the antiproton stopping trap

in front of the Positronium converter. Moving the hot plasma of positrons off-axis is a tricky operation. The proposal of AEGIS collaboration is to exploit the diocotron plasma mode to accelerate radially the hot plasma in a spiraling motion and move it to the launch trap when the correct position is reached. INFN Genova group demonstrated the feasibility of such technique using an hot electron plasma.

5. **1T positron launch trap:** the positron launch trap is placed exactly above the 1T antiproton stopping trap. It receives the off-axis positron beam from the diocotron trap and squeezes the cloud both radially and longitudinally to compact the positron packet as much as possible in the beam direction. Finally, accelerates the cloud to the required energy to perform the implantation in the Positronium converter (usually around $7\,keV$). The launch time of the positrons is synchronized with the laser apparatus in order the Positronium cloud emerging from the converter to be hit by the laser light pulse.
6. **1T antihydrogen formation trap:** before the positrons leave the launch trap, all the antiprotons contained in the stopping trap are moved and stored into a tiny trap made of aluminum electrodes with small holes on the upper surface right under the Positronium converter. The excited Positronium moving downward from the converter enters the trap from the tiny holes and interacts with the stored antiprotons to form the antihydrogen (see Figure 2-2).

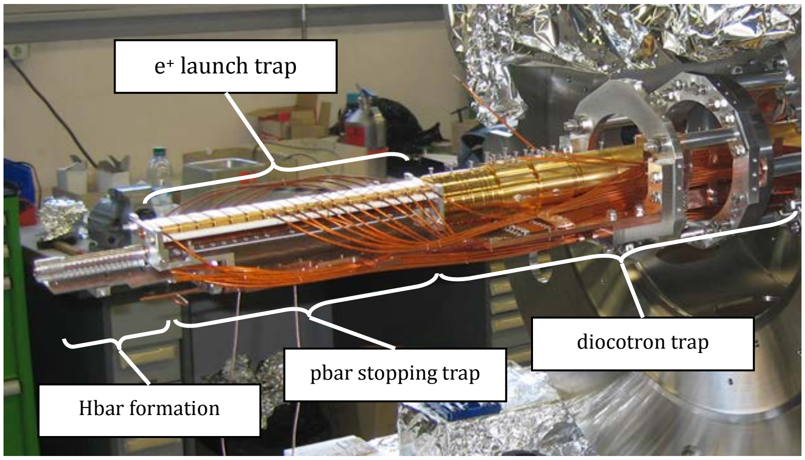

Figure 2-11: AEGIS 1T region trap system. The beam line coming from the 5T region enters from the top-right on the image. The first trap on the line is the diocotron trap, moving the positrons to the launch trap (on the top). Under the launch trap there is the antiproton stopping trap that prepares the bunch for the antihydrogen formation trap, on the left end of the trap.

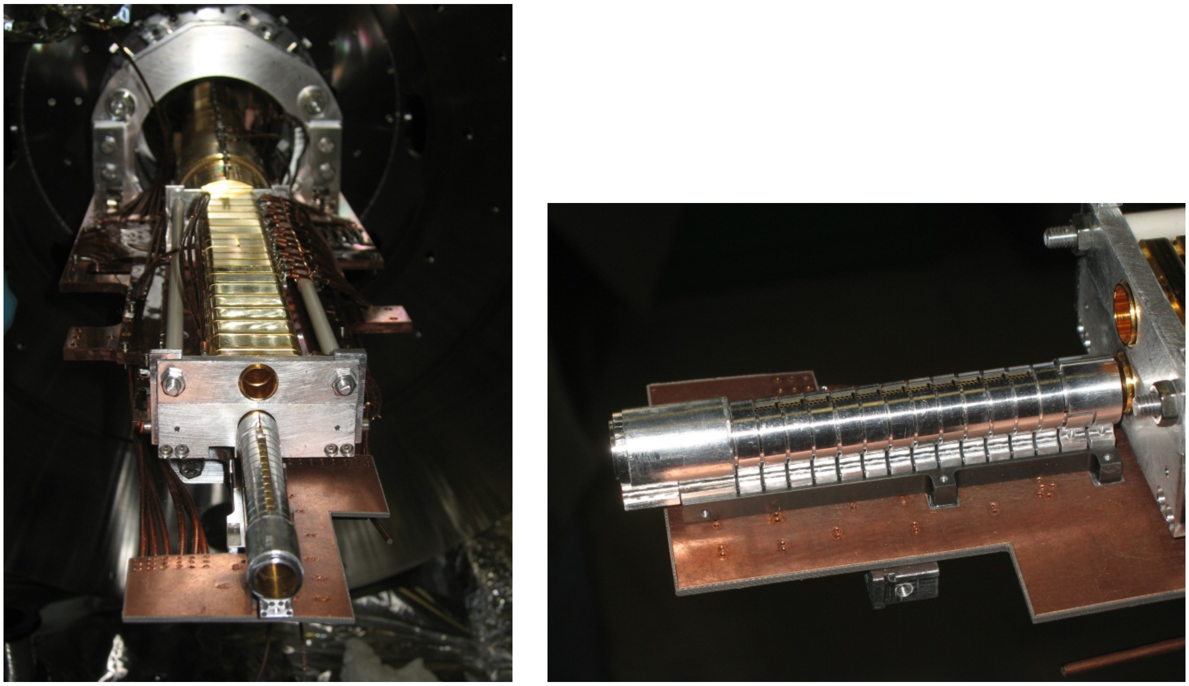

Figure 2-12: Front and side view of the antihydrogen formation region. In the front image (left) it's clearly visible the different vertical position of the positron launch trap with respect to the antiproton beam axis. In the side image (right) shows the antihydrogen formation trap with the holes on the top side clearly visible to let the excited Ps come inside.

2.4.2 Antihydrogen production

Antihydrogen is produced in AEGIS by the charge exchange reaction

$$Ps^* + \overline{p} \rightarrow \overline{H}^* + e^- \tag{2.3}$$

Where Ps^* and H^* are high excited states of Ps and H, respectively.

The use of this reaction to produce antihydrogen has been demonstrated by the ATRAP collaboration in 2006 [Storry 2004]. The main reason to choose this reaction to produce antihydrogen is the very large cross section of interaction between $\overline{p}$ and Ps^* at Rydberg states, since $\sigma_{CE} \propto n^4$ where n is the principal quantum number of the excited Ps.

A numerical study on the exact value of the cross section has been carried out before the proposal of the experiment (see [AEGIS 2007 pp. 31-36]). The results obtained are synthetically the following:

1. The cross section of interaction is approximated by the power law

   $$\sigma_{CE} = A \cdot n^B \tag{2.4}$$

   where

   $$\begin{aligned} A &= \left(1.964 \pm 0.045\right) \cdot 10^{-9}\, cm^2 \\ B &= 4.22 \pm 0.23 \end{aligned} \tag{2.5}$$

   in agreement with the expected exponent 4;
2. The interaction between antiproton and Rydberg Positronium produces Rydberg antihydrogen at an higher Rydberg level;
3. The antihydrogen is produced at very low temperature;
4. In AEGIS working conditions the maximum acceptable Ps speed to produce antihydrogen is

   $$v_{Ps} = 10^5\, m \,/\, s \tag{2.6}$$

   thus setting an upper bound to the maximum energy of the Ps. The temperature range in K below to the maximum speed is

$$T_{Ps} \leq 660\,K \tag{2.7}$$

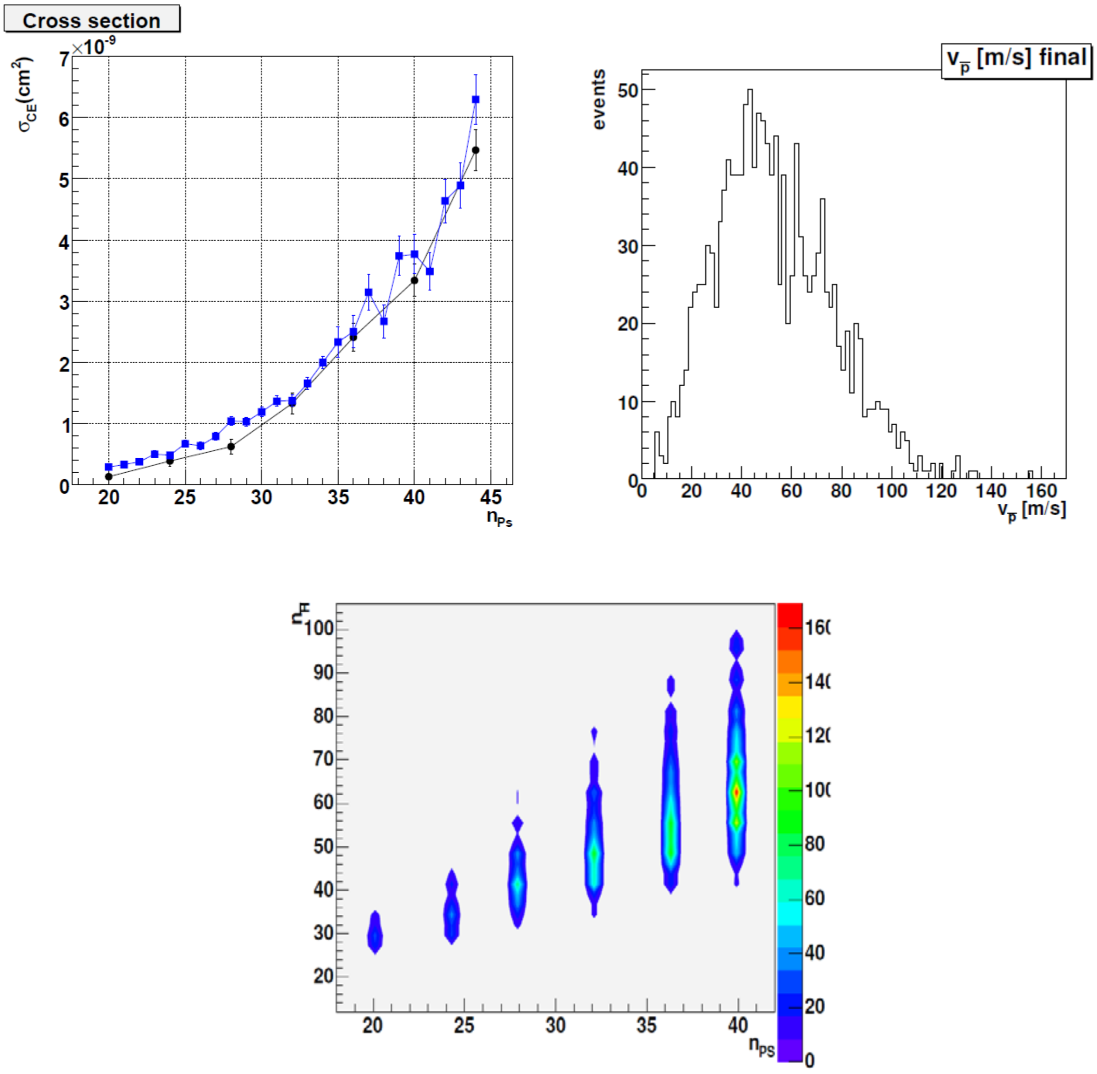

Figure 2-13: Results of the numerical simulation of charge exchange reaction. The first graph (top left) shows the reaction cross section σ_{CE} vs the princial quantum number n_{PS} of the Ps in AEGIS for a chosen orbital quantum number $l = 2$ (black line) and with random l (blue line), showing that the reaction rate is independent from l. The second graph (top right) shows the velocity distribution of the produced antihydrogen. The third graph (below) shows the distributions the principal quantum numbers n_R of produced antihydrogen atoms as a function of n_{PS}.

2.4.3 Gravitational acceleration measurements

AEGIS exploits a Moiré deflectometer to perform the measurement of the vertical caused by the gravitational acceleration of an antihydrogen beam travelling in the horizontal direction. In some respect, the apparatus is similar to a Mach-Zehnder matter wave interferometer with three identical gratings placed at equal distance from each other: in the Mach-Zehnder the first two gratings produce an interference pattern on a moveable third grating that is placed in front of a detector. Moving the third grating in the vertical direction allows reconstructing the diffraction pattern from the gratings; for example, the vertical displacement associated to the maximum signal would correspond to the vertical displacement of the beam due to the free fall

$$\delta = -gT^2 \tag{2.8}$$

where T is the time of flight between each pair of gratings.

In the Moiré deflectometer the interference pattern is purely cinematic, formed by the particle trajectories crossing the gratings, and it is not produced by diffraction. In fact, the grating period d and relative position L are chosen so that $d^2 / L >> \lambda_{dB}$ with λ_{dB} being the De Broglie wavelength.

The third grating is removed in favor of a position-sensitive detector (for instance, a pixel detector) measuring the shadow pattern of the atoms that come out of the first two gratings. This type of detector overcomes some limitations of the original Mach-Zehnder-like configuration, for instance the need of very low beam divergence. Most characteristics of interferometer are retained, in particular the vertical displacement of the resulting pattern due to free fall.

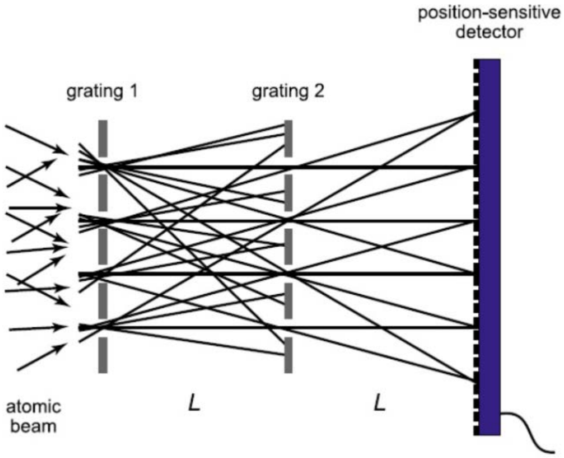

Figure 2-14: Scheme of the Moireé deflectometer used to measure the displacement due to gravitational acceleration of antihydrogen.

After the antihydrogen is formed in the last trap, a gradient of electric fields accelerates the cloud to a speed of $25-80\,m\,/\,s$. The expected vertical displacement can be easily calculated from (2.8). Numerical simulations performed by [Kellerbauer 2008] show that about 10^5 atoms of antihydrogen at a temperature of $100\,mK$ are required to measure the gravitational acceleration to 1% relative precision.

2.5 The Positronium spectroscopy experiment apparatus

The AEGIS apparatus for the production of an intense beam of positrons offers the interesting possibility to perform studies on the formation of Positronium and its laser excitation. For this purpose, a controlled environment independent from the main apparatus has been built by the Trento group: a vacuum chamber with a compact accelerating beam line where the positron bunch reach energies up to $10\,keV$ and is implanted in the converter (see Figure 2-15).

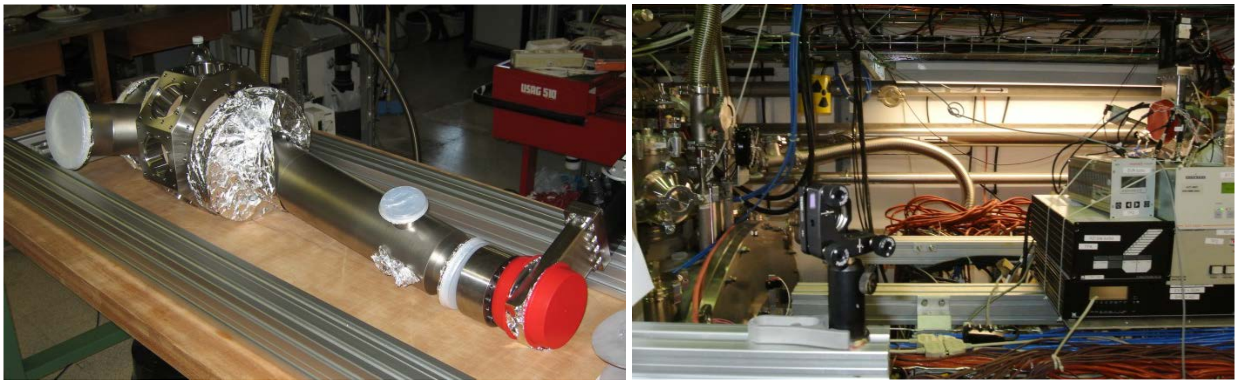

Figure 2-15: The Positronium experiment chamber under construction in the Trento Ps laboratory (left) and its mounting site at CERN above the antiproton beam line (right). The chamber will be installed on the right side of the rail to fit to the red actuator flange already in position. In the central region of the photograph there is the last mirror of the laser transport line ready to send the radiation inside the chamber from one of the viewports in the octagonal bellow.

The positrons come first in the transport line from the accumulator stage. The transport line is made of a sequence of insulated cylindrical electrodes, each connected to a high voltage external source, which accelerates the positrons with an electric field gradient. The regular increasing potential is generated connecting a high tension generator to a battery of resistors of the same resistance value connected in sequence, each causing the same potential drop (Figure 2-16).

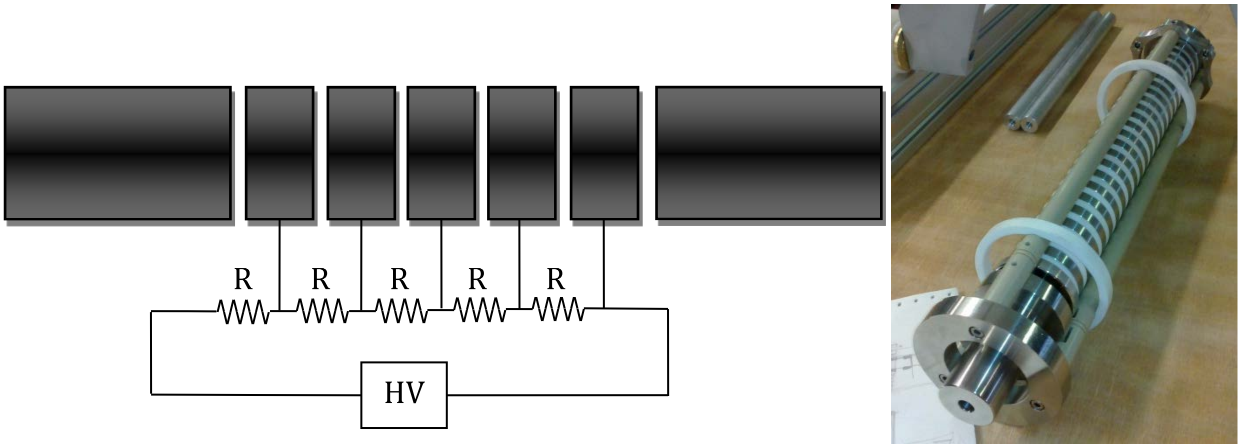

Figure 2-16: Scheme and photograph of the Ps acceleration transport line before the spectroscopy experiment

The Positronium converter is installed in the middle of an octagonal bellow with two viewport on the sides to let the laser radiation come in. While the converter region is kept at high vacuum and a low temperature to perform the experiments, a heater is installed on the back of the target to raise the temperature above 50 °C to remove the superficial ice that spontaneously collects on the silica when the temperature is below 70 K. This temperature cycle is called *annealing*.

The main diagnostic tool to detect how much Positronium is formed in the converter is a movable CsI scintillator outside the bellow.

3 Elements of laser physics

3.1 What is a laser?

The word "laser," an acronym for light amplification by stimulated emission of radiation, came into the common language to generically denote any device that produces a collimated light beam. In fact, an actual laser is distinguished from a regular thermal light source (even if collimated) by the very characteristics that make it such an extremely valuable scientific and technologic instrument.

Strictly speaking, a laser is an electromagnetic device meant to produce a collimated light beam with specific properties (directionality, monochromaticity, coherence, and high brilliance). It exploits the effect of stimulated emission of many materials under particular excitation conditions (population inversion of the energetic levels) to amplify a stationary light pulse built-up inside a resonant cavity.

Structurally, most lasers are composed of a resonant cavity (*cavity*, for short) made of two mirrors in front of each other with a piece of the emitting material in the middle (the *active medium*, AM). One of the two mirrors (the output coupler) is chosen to be slightly transmissive (usually more than 90% of the radiation is reflected, with the rest transmitted); the fraction of the light that comes out the cavity from the partially reflective mirror forms the *laser beam*.

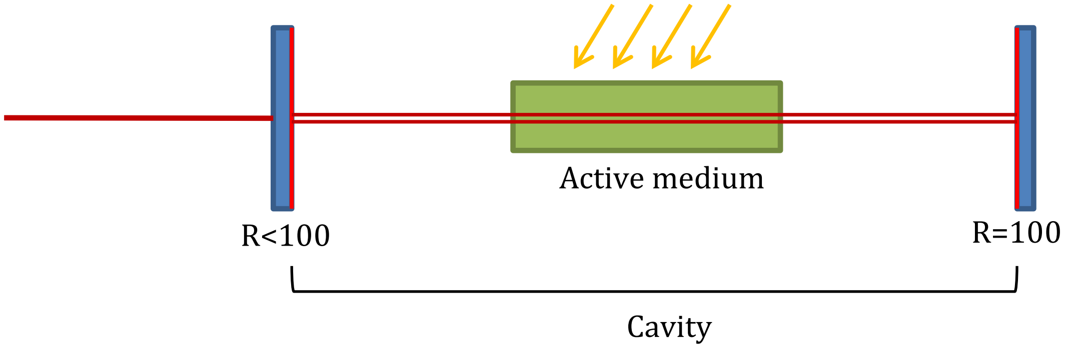

Figure 3-1: Simplified scheme of a laser cavity. The active medium (green) is externally pumped to obtain population inversion. In working conditions, it amplifies the stable light mode that forms inside the cavity. The two mirrors (blue) form the resonant cavity, which is tuned to the frequency of the stimulated emission. One of the two mirrors (the output coupler) has a transmission coefficient in the order of a few percent to let some radiation out of the cavity, forming the laser beam.

3.2 Characteristics of laser radiation

Let's take a closer look at the laser-light properties mentioned above:

- **Monochromaticity:** The laser cavity acts as an optical resonator with its own eigenfunctions, or modes, both in the longitudinal and transversal directions, each characterized by a precise oscillation frequency and line width. Longitudinal modes, in particular, are equally spaced in spectrum by the *free-spectral range* frequency $c \,/\, 2L$, where L is the effective length of the cavity (see the Free spectral range paragraph for a more exhaustive discussion). The active medium amplifies all the modes whose oscillation frequency falls within the gain line, which is usually well wider than the proper line width of single modes. Laser cavities oscillating on a single mode (usually longitudinal, if not specified) are called single mode lasers. The spectral line width of the produced radiation by a single mode cavity is caused primarily by the phase fluctuations of the electric field inside the cavity or by technical effects such as vibrations of the cavity (negligible for most pulsed lasers because mechanical vibrations happen on a completely different time scale). A neat example of single mode laser is the He-Ne gas, whose line width is extremely small, in the order of $\propto kHz$. In the case of a multi-mode laser, monochromaticity is a concept less stringent, related to the number of oscillating modes and their relative phase. If no mode-locking is present in the cavity, then the sum of the modes is completely incoherent. The resulting emission wavelength and line width correspond to the mode superposition. Otherwise, if mode-locking is present, the resulting pulse is short in time and thus wide in the spectrum: the condition of quasi-monochromaticity no longer holds well. Generally speaking, short duration of laser pulses limits the minimum line width due to phase fluctuations also in the case of Q-Switched lasers: for a $\tau \sim 4\,ns$ pulsed laser, like the AEGIS one, one has $\Delta\nu > 250\,MHz$.
- **Spatial coherency:** spatial coherency is a property of wave fronts of electromagnetic waves. It is defined considering wave fronts at different times. Consider a wave front for which, at the beginning $t = 0$, there exist a precise phase

relation between electric fields in any two points: for instance, if in all the points of the wave front the electric field exhibit the same phase. If this phase relation between different points of the wave front is the same at every time, then the wave exhibit perfect spatial coherence.

- **Temporal coherency:** temporal coherency is also a property of wave fronts of electromagnetic waves, but differently from spatial coherency it is due to the phase correlation between the same points on the wave front at different times. With an ideal amplification stage inside the laser cavity, free of any de-phasing effect, the phase of the electric field in a point inside would stay the same for infinite time (perfectly stationary mode). In a real condition, some de-phasing effects inside the AM can abruptly change the phase of the mode living in the cavity (vibrations of the AM crystal, collisions, spontaneous emission…). The characteristic time of phase correlation of a point in the cavity is known as *coherency time*.
- **Directionality:** in the case of most laser cavities, for example a plane parallel one, directionality is a consequence of the orientation of the mirrors, because only a wave propagating in a direction orthogonal to them can live inside the cavity. The minimum divergence of a finite-size beam with perfect spatial coherency is given by its diffraction limit, usually written as $\vartheta = \beta\lambda / D$ where D is a suitably defined beam diameter and β a numerical factor. Beams with partial spatial coherency have greater divergence at constant diameter. The coherence area S, smaller that the beam area $A \propto D^2$, acts as a limiting aperture in the diffraction limit, leading to $\vartheta = \beta\lambda / \sqrt{S}$.

3.3 Laser operation

In the first paragraph a review on the interactions between radiation and atoms is given to introduce the phenomena acting inside the laser active medium. A description of the laser operation is then given in the following paragraph, together with the simple theoretical model of the rate equations that describes the laser dynamics.

3.3.1 Absorption, spontaneous emission and stimulated emission

Three classes of phenomena can happen when the electromagnetic field interacts with atoms.

1. **Absorption:** the atom jumps from its initial state to an excited state absorbing a photon of the field, i.e. an energy quantum carried by the radiation;

$$E_1 + \gamma \longrightarrow E_2 \tag{3.1}$$

2. **Spontaneous emission:** an atom, at the beginning in an excited state, emits a photon decaying to a lower energy state;

$$E_2 \longrightarrow E_1 + \gamma \tag{3.2}$$

3. **Stimulated emission:** an atom, at the beginning in an excited state, is forced by an external photon of the field to decay and emit a new photon with the same wavelength and phase as the interacting photon. The external photon doesn't provide any energy, but only acts as stimulus. In order this process to happen, the energy of the incoming photons must match at best the energy difference between the initial and final state.

$$E_2 + \gamma \longrightarrow E_1 + \gamma + \gamma \tag{3.3}$$

A simple mathematical description of absorption, spontaneous emission and stimulated emission can be work out just by writing the balance equations for the given processes, as pointed out by [Einstein 1917]. Let's define N_1 as the number of atoms (population) in the interaction volume V (in the case of lasers, V is the volume of the AM) for the lower energy level (*population*, from now on) and N_2 as the population for the higher energy level. An electromagnetic field of energy density ρ is present in the whole volume of interaction. The energy density is proportional to the population of photons ϕ by

$$\rho = \frac{h\nu}{V} \cdot \phi \tag{3.4}$$

The effect of absorption on the populations is described by the equations

$$\begin{aligned}\frac{\partial N_1}{\partial t} &= -B_{12}\rho N_1 \\ \frac{\partial N_2}{\partial t} &= B_{12}\rho N_1\end{aligned} \tag{3.5}$$

That is, the variation of the population over the time is given by the amount of photons in the volume times the amount of absorbing atoms in the volume times a coefficient that contains the probability of an absorption event. The effect of stimulated emission on the populations is described exactly by the backwards equations (the extra forcing photon has not to be taken into account when calculating the populations, since it's not modified during the process)

$$\begin{aligned}\frac{\partial N_1}{\partial t} &= B_{21}\rho N_2 \\ \frac{\partial N_2}{\partial t} &= -B_{21}\rho N_2\end{aligned} \tag{3.6}$$

It can be shown with thermodynamic arguments that $B_{12} = B_{21}$ (when energy levels are not degenerate), or just note that the crossing symmetry of quantum electrodynamics should hold also at the level of atomic physics.

Only the spontaneous emission is described by slightly different equations

$$\begin{aligned}\frac{\partial N_1}{\partial t} &= AN_2 \\ \frac{\partial N_2}{\partial t} &= -AN_2\end{aligned} \tag{3.7}$$

where A , the coefficient of spontaneous emission, represents the probability in the unit time (or the number of events per unit time) that an excited atom in the E_2 level incurs in spontaneous decay to level E_1 without external perturbation. For simplicity, we can recognize A to be a characteristic decay time $\tau = \frac{1}{A}$ for excited population.

A relation linking A and B can demonstrated, again with thermodynamic arguments. On the other hand the explicit expression of these coefficients cannot be given with these simple arguments. It can be derived, for instance, by exploiting the semi-classical theory of radiation-atom interaction. The knowledge of one of the coefficients is then sufficient, using the thermodynamic relations, to derive the others.

3.3.2 Four-level laser operation

For the purpose of this thesis, only the operation details of a four-level laser scheme will be described to give some insights on the Q-Switched Nd:YAG $1064\,nm$ cavity that constitutes the master laser of AEGIS optical system.

Laser operation is driven by the stimulated emission of radiation that happens inside the active medium when some photons of the stationary mode of the cavity interact with the excited atoms in the AM. The laser medium receives energy from an external power source, usually called *pump*, which takes care of providing the required *population inversion* condition. This means that the numerical density of atoms in an excited state is greater than the numerical density of atoms in a lower state of a specific extent called inversion threshold. In order the population inversion condition to be established, a careful choice of the transition line must be made.

Let’s consider a level transition with very long spontaneous emission time. An example of material often used as active medium in IR lasers is Nd:YAG, an Yttrium Aluminum Garnet crystal (YAG) doped with 1% of Neodymium ions (Nd^{3+}), that is the crystal used as AM inside AEGIS laser. Besides other optical transition, it has a metastable transition owing to the crystal field splitting, with wavelength $1064\,nm$ and the very long spontaneous emission time of $\tau = 0.23\,ms$.

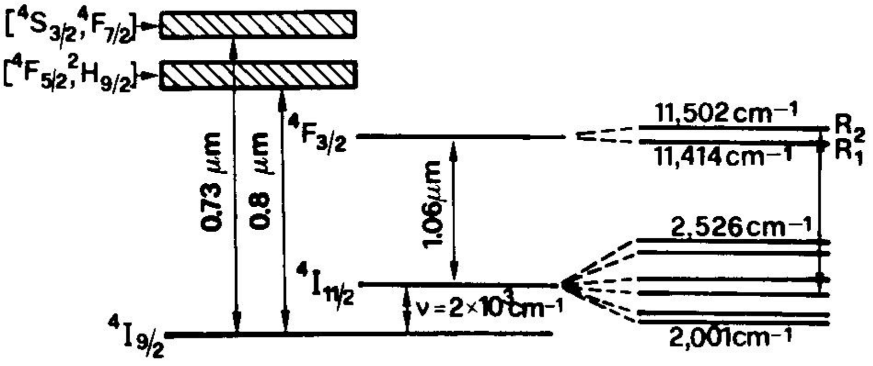

Figure 3-2: Scheme of Nd:YAG levels, courtesy of [Svelto 2010].

An external light (often from semiconductor laser diodes) source shines radiation at $\lambda = 808\,nm$ on the YAG crystal, thus exciting the Nd ions with the transitions

$$\begin{aligned} {}^4I_{9/2} &\longrightarrow {}^4F_{5/2} \\ {}^4I_{9/2} &\longrightarrow {}^2H_{9/2} \end{aligned} \tag{3.8}$$

Shortly after the excitation, the atoms decay non-radiatively very quickly to the level ${}^4F_{3/2}$ and find the forbidden transition

$${}^4F_{3/2} \longrightarrow {}^4I_{11/2} \tag{3.9}$$

The population of ${}^4F_{3/2}$ increases as the pumping operates because the spontaneous transition decay time is long. The few atoms reaching the level ${}^4I_{11/2}$ incur again in a very fast decay to the ground level.

$${}^4I_{11/2} \longrightarrow {}^4I_{9/2} \tag{3.10}$$

This transition keeps the population of the level ${}^4I_{11/2}$ at a very low level, transferring quickly the atoms to the ground state. Within this scheme a population inversion between levels ${}^4F_{3/2} \rightarrow {}^4I_{11/2}$ is realized. As mentioned above, the Nd:YAG laser works on this optical transition. The key to understand the laser operation is in the dependency of the stimulated emission rate on the intensity of the radiation shining on the AM.

At the moment of turning on the laser, the spontaneous emission effect is predominant over the stimulated emission because there are no photons in the cavity to interact with the active medium. Spontaneous emission causes the AM to shine radiation at all allowed wavelengths inside the cavity, including a little of photons on the laser wavelength $1064\,nm$. These photons bounce on the mirrors, re-enter in the AM and incur in the stimulated emission effect producing new photons with the same wavelength and phase. The more photons are entering in the AM, the more photons are produced by stimulated emission incrementing the whole number of photons in the cavity.

The number of photons progressively increases up to around the equilibrium level. Then it begins to oscillate around the equilibrium level with the so called relaxing oscillations, which are progressively damped until the number of photons stabilizes at the equilibrium level, where the gain of the active medium equals the losses of the cavity.

3.3.3 Rate equations

The equations of population dynamics (3.5), (3.6), (3.7) already offer a valid starting point to develop a theory for the laser operation. To complete the description of the laser cavity two aspects have yet to be considered: the loss of photons by the cavity and the pumping.

Before proceeding, we need to rewrite the equations in terms of the number of photons currently living in the cavity, ϕ, instead of the electromagnetic energy density inside the active medium volume. This way, it becomes feasible to add a loss term to the differential equations describing the number of photons in the cavity. Noting that $\rho \propto \phi$ and absorbing the proportionality factor redefining the constants A, B_{12} into new empirically determined parameters A_0, B_0, we can write the rate equation for the population of photons inside the cavity as:

$$\frac{\partial \phi}{\partial t} = B_0 V \phi N_2 + A_0 N_2 \tag{3.11}$$

The spontaneous emission term can be neglected in most practical cases. Besides that only a very small fraction of spontaneously emitted photons can contribute to the cavity mode for geometrical reasons, the spontaneous emission term does not depend by ϕ, which is rapidly growing as the laser power increases.

Let's introduce now the losses of the cavity in the rate equations model. There are two kinds of losses in a laser cavity:

1. **Desired losses:** the output coupler relatively low reflectivity introduces some losses due to the transmission of a small fraction of the cavity photons. These losses are desired, clearly, otherwise no radiation would come out of the device;
2. **Undesired losses:** even in the best tuned cavity some undesired losses are present, due to the presence of a non-perfectly transmitting medium in the cavity (air), due to unwanted absorption by mirrors, or due to diffraction by the edges of the active medium.

Both contributions can be managed in the same way, introducing a non-null probability that a photon exits the cavity in the unit time because of the losses. Let's call this probability $1 / \tau_c$, where τ_c is the characteristic time of permanence inside the cavity. The differential equation is thus rewritten as

$$\frac{\partial \phi}{\partial t} = B_0 V \phi N_2 - \frac{1}{\tau_c}\phi \tag{3.12}$$

The second differential equation describing the laser behavior is the dynamical equation of the population of the excited level rewritten in terms of ϕ. If we include all the terms coming from of absorption, stimulated emission and spontaneous emission (3.5), (3.6), (3.7), then the differential equation takes the form

$$\frac{\partial N_2}{\partial t} = B_0 \phi N_1 - B_0 \phi N_2 - \frac{1}{\tau} N_2 \tag{3.13}$$

First, notice that for a four level laser the term proportional to N_1, the population of the intermediate level, is negligible. In fact, it is always very low because of the fast transition towards the ground state. This is not the case for a three levels laser: in this case the term

N_1 cannot be neglected and a third equation describing the dynamics of N_1 is needed to complete the system. The quantity $N_2 - N_1$ is the *population inversion*: it is clear now why the active medium must be kept in this condition in order the laser to work. No amplification is provided from the AM if the population inversion is not established.

Secondly, we can introduce easily the pump contribution by thinking of it as a constant source of population inversion, increasing the population in N_2 at a constant rate proportional to the power dissipated by the pumping system. Calling the pump ratio R, we have then

$$\frac{\partial N_2}{\partial t} = R - B_0 \phi N_2 - \frac{1}{\tau} N_2 \tag{3.14}$$

Equation (3.14), together with (3.12) are called the *rate equations* for a four level laser. Despite of their simplicity, they describe very accurately the dynamics of a laser.

In the following paragraphs the rate equations will be solved numerically and analytically (up to a certain degree of approximation) to deduce the transient behavior of a Q-Switched laser like the AEGIS one.

3.4 Unstable cavities

The rate equations presented in the last paragraph give a valid model to describe the dynamical behavior of the laser, but give no information neither about the spatial structure of the stationary mode formed inside the cavity nor about its temporal/spectral characteristics. The resonant cavity acts twice on the stationary mode: it imposes the wavelength of the amplified mode depending on its spectral characteristics and imposes a precise spatial structure to the mode. We will postpone to the next paragraph the discussion on the time and spectral characteristics of the pulse.

The easiest way to see why a resonant optical cavity has a discrete number of resonating modes, both longitudinal and transverse, is to notice its similarity to a wave guide. First of all, the underlying equations are the same (the Maxwell equations). Secondly, both a wave guide and a laser cavity have walls beyond which the radiation is dumped out that imposes boundary conditions: in the case of the wave guide, the external surface of the guide; for the optical cavity, the borders of the active medium, which is limited in space, and the reflecting mirrors placed along the preferred propagation direction. In both cases the radiation is free to propagate without any source or active element acting on it and then reflect on walls and/or mirrors of the guide/cavity.

As for the wave guides, also for the optical cavities the allowed transversal modes are only the eigenfunctions of the Laplacian operator with the boundary conditions imposed by the external walls. For instance, the complete set of transversal eigenfunctions that can be formed in a cylindrical cavity are the Hermite polynomials multiplied to a Gaussian kernel (see example in Figure 3-3).

It's not the goal of this work to present a full treatment of the eigenfunctions of a laser cavity. The only important aspect worth to mention is that the AEGIS laser uses an instable cavity to increment the beam transversal size. An instable cavity doesn't allow the laser to operate in continuous mode since the planar shape (or even convex, as in the case of AEGIS) of the reflecting mirrors introduces heavy losses. It is an effective choice, however, in the case of an intense pulsed laser where only a few round trips are made inside the cavity before the power is completely depleted. The eigenfunctions of an instable cavity are much spatially expanded with respect to those of a stable cavity.

In the case of AEGIS pump laser, the fundamental mode (a top-hat function) is so wide that it covers the whole area of active medium; the main advantage of using a single transverse mode laser being the possibility of focusing it with a very small focus.

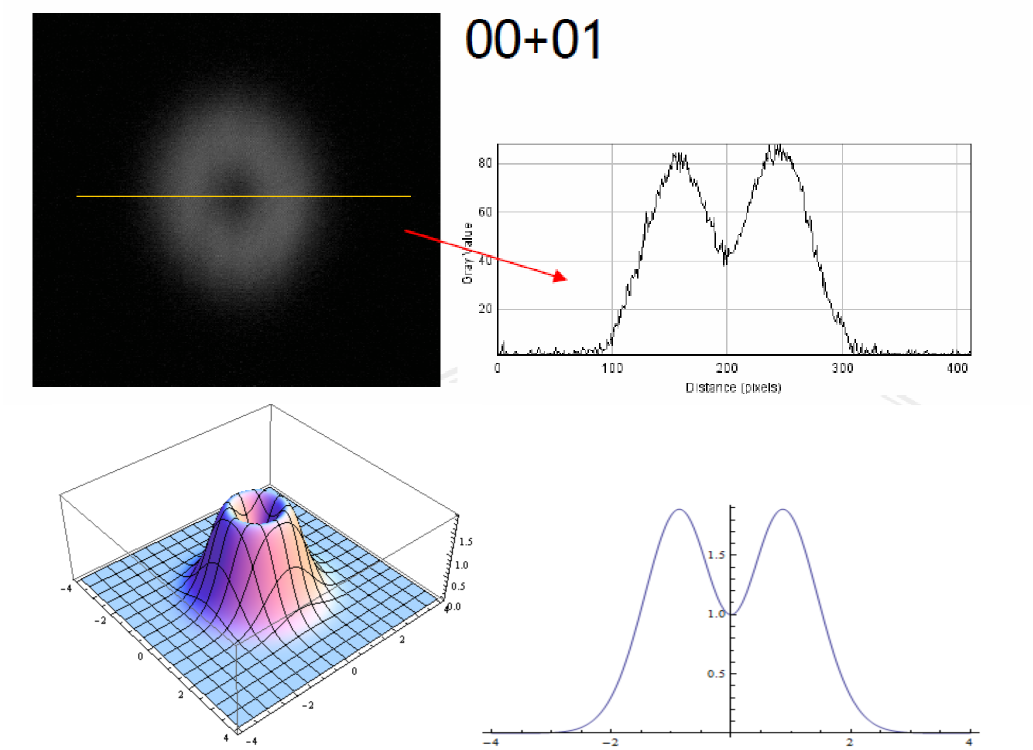

Figure 3-3: Comparison between the measured intensity profile of a cylindrical Nd:YAG laser pumped to the second transversal mode with the expected profile obtained summing the first two cavity eigenfunctions. The two images on the top show the beam profile and its horizontal section; the two images on the bottom show the incoherent superimposition of the first two Hermite polynomials (arbitrary units).

3.5 Free spectral range

If we place a fast photodiode in front of the laser cavity, we would notice that the detected waveform is periodic with period T_{FSR}.

This happens because the lasing mode the cavity is stationary, being built on the round-trip condition: the electric field must be identical in amplitude and phase after a full round trip in the cavity frontwards and backwards. In other words, it has to be periodic in time with a period equal to the time needed to travel twice the linear length L of the cavity (from mirror to mirror and back again).

The inverse of the round trip time of the pulse inside the cavity is called *free spectral range*, because it coincides with the frequency difference between longitudinal radiation modes of the cavity, which compose the stationary laser mode.

$$\nu_{FSR} = \frac{1}{T_{FSR}} = \frac{c}{2L_{eff}} \tag{3.15}$$

The free spectral range is an effective tool to measure the cavity effective length (i.e. taking care of the active medium index of refraction). This method was implied to measure the cavity length of AEGIS pump cavity (see Chapter 5).

3.6 Q-Switched laser modality

The Q-Switched laser modality is one of the most common techniques to operate a laser cavity in pulsed regime, widely used when an intense and energetic laser pulse is needed. With respect to other types of pulsed lasers, like for instance the mode-locking lasers, Q-Switched pulses don't reach extremely low time durations and high powers: a typical pulse length is in the order of a few ns with respect to mode-lockers that can easily reach the ps scale or even fs. On the other hand, Q-Switched pulses are much more energetic than mode-locking pulses, making a Q-Switched laser the right choice if an highly energetic laser pulse is required (as in the case of Ps excitation).

The working principle of Q-Switched lasers consists in modulating the cavity losses as a function of time. Enhancing the cavity losses causes all the photons living in the cavity to be dumped, thus allowing the active medium to be charged by the pump at the maximum level of population inversion without any consumption due to stimulated emission. When the maximum level is reached, the losses are abruptly lowered to the working value allowing the formation of a huge amount of photons in the cavity that rapidly discharge the active medium and form the giant pulse.

The two most common ways to perform cavity losses modulation are:

1. **Acusto-optical modulation:** a quartz crystal with a piezoelectric oscillator is placed inside the cavity. A stationary acoustical mode is established in the crystal with a pilot electric wave on the piezoelectric; the acoustic wave causes a sinusoidal variation of density of the crystal that induces also a sinusoidal variation of the index of refraction. The crystal acts as a sinusoidal phase grating diffracting a fraction of the beam at different angles outside the cavity, thus increasing the

cavity losses. The diffracting power of the crystal, as well as the induced losses, can adjusted changing the amplitude of the acoustic mode in the crystal.

2. **Electro-optical modulation:** this technique is based on the Pockels effect, which is the ability of some material to rotate the polarization of an incoming wave when subjected to an external electric field: the electric field alters the crystalline structure of the cell that becomes birefringent, thus acting as a quarter wave plate. A Brewster plate placed after the Pockels cell reflects the fraction of rotated polarization outside the cavity inducing the losses.

The AEGIS laser cavity uses a Pockels cell to modulate the losses during operation. In the next paragraphs we will work out a mathematical model starting from the laser rate equations (3.12) and (3.14) to determine and discuss the characteristics of the AEGIS pump laser.

Three phases characterizes the Q-Switched laser operation:

1. Storing energy in active medium by external pumping;
2. Release of the giant pulse;
3. Dead time to restore initial conditions.

3.6.1 Pumping the active medium

Let us consider the rate equations for the laser cavity (3.12) and (3.14).

$$\begin{aligned}\frac{dN_2}{dt} &= R - B_0\phi N_2 - \frac{1}{\tau}N_2\\ \frac{d\phi}{dt} &= B_0 V\phi N_2 - \frac{1}{\tau_c}\phi\end{aligned} \tag{3.16}$$

At the beginning of the cycle, the active medium is fully depleted and the cavity contains no photons.

$$\begin{aligned}N_2\left(0\right) &= 0\\ \phi\left(0\right) &= 0\end{aligned} \tag{3.17}$$

Then the pump is activated while the high losses keep the number of photons low. The term proportional to ϕ in the differential equation for N_2 is thus negligible, then

$$\frac{dN_2}{dt} = R - \frac{1}{\tau} N_2 \tag{3.18}$$

The solution of this equation can be found with standard methods and fixing the boundary conditions. The result is

$$N_2(t) = R\tau\left(1 - e^{-\frac{t}{\tau}}\right) \tag{3.19}$$

As expected, the population inversion saturates: it reaches the 95% of its asymptotical value, $R\tau$, after the time $\approx 3\tau$.

3.6.2 Giant pulse formation

After the energy charging is completed and population inversion has reached its asymptotical value, the losses in the cavity are quickly reduced, in a few nanoseconds, to the working condition of the laser. In the rate equations the pump ratio can be neglected because the time scale of the pulse production is orders of magnitude lower than the scale of the pumping process. For the same reason, also the spontaneous emission term doesn't play a relevant role (the time scale is in the order of hundreds of μs instead of ns).

The differential equations are simplified to

$$\begin{cases} \frac{dN_2}{dt} = -B_0\phi N_2 \\ \frac{d\phi}{dt} = B_0 V\phi N_2 - \frac{1}{\tau_c}\phi \\ N_2(0) = R\tau \\ \phi(0) \approx 0 \end{cases} \tag{3.20}$$

The presence of the non-linear term $\propto \phi N_2$ in both equations makes the task of solving analytically the equations rather cumbersome. Two ways can be exploited: the numerical integration of the equations and the use of a very robust and meaningful approximation to reduce the problem to an analytically solvable form.

First, let's integrate the equations numerically to graph the expected time dependence of the population inversion and the number of photons. It is necessary to use a value for

$\phi(0)$ slightly different from 0 (as a matter of fact, a small number of photons is always present in the cavity due to spontaneous emission) when setting the boundary conditions in a numerical solver, otherwise it would fall on the trivial 0 solution.

The numerical solutions obtained in ideal working conditions are shown in Figure 3-4.

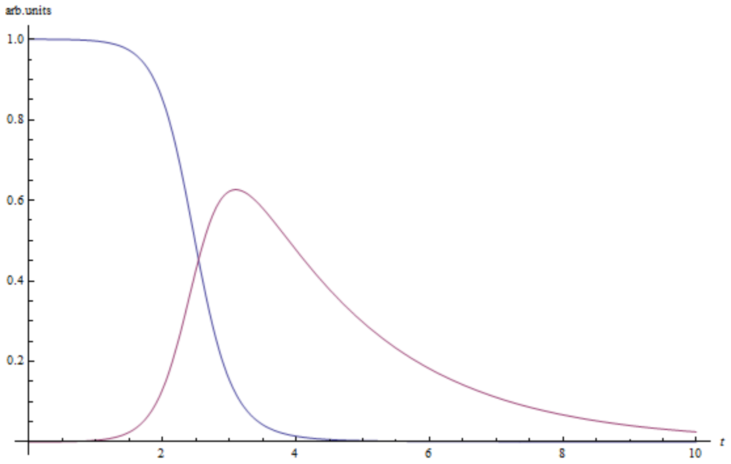

Figure 3-4: Numerical integration of the rate equations under the Q-Switched laser conditions. All the cavity parameters B_0, V, τ, R are set to unity to graph the results, excepting$\tau_c = 2$. The blue curve is the population inversion; the purple curve is the number of photons living in the cavity. Both curves have arbitrary units on the vertical axis.

As expected, the number of photons inside the cavity grows quickly to a maximum value and then decreases smoothly according to the progressive losses of photons by the cavity. The resulting shape is pulse-like, with a temporal length of few nanoseconds. Moreover, the derivative of the population inversion over time is sensibly different from zero only in the region of the peak number of photons. The maximum number of photons in the cavity corresponds to the population inversion for which the gain of the active medium equals the losses of the cavity, which is the same condition that holds for a laser operating at equilibrium in continuous mode.

In order to derive an analytical solution for the rate equations, we must first note that while the laser pulse decreases from its maximum value, the value of the population inversion is very low and not sensibly varying during time. We can reasonably approximate the time derivative of the population inversion to be null in that region,

$$\frac{dN_2}{dt} \approx 0 \tag{3.21}$$

This implies automatically that the other term in the first differential equation is close to zero

$$B_0 \phi N_2 \approx 0 \tag{3.22}$$

As a consequence, we can neglect the same non-linear term also in the differential equation for the number of photons

$$\frac{d\phi}{dt} = \cancel{B_0 V \phi N_2} - \frac{1}{\tau_c}\phi \tag{3.23}$$

Integrating the resulting equation gives

$$\phi\left(t\right) = \phi_0 e^{-\frac{t}{\tau_c}} \tag{3.24}$$

We expect the pulse to have an exponential decay rate after its maximum driven only by the $1 / \tau_c$ term.

The important thing to note, however, is that the two processes – pulse amplification and pulse decay – are characterized by a very different time scale. The pulse amplification process is predominant until the excited population is near totally depleted and the population inversion reaches a very low value.

At this stage the pulse reaches its maximum level, and the cavity loss term starts to act. Being the population inversion already decreased to a small fraction of the original, the term proportional to the cavity losses doesn’t play any substantial role in determining the temporal profile for the population inversion.

This is a good starting point to derive an analytical solution for the rate equations. We will neglect the term $\propto 1 / \tau_c$ in the rate equations, determine the temporal profile of N_2 in this approximation, and use the result to solve the differential equations in the general case.

3.6.3 Analytical derivation of the shape of the pulse in $\tau_c \rightarrow \infty$ approximation

Let us consider the rate equations neglecting the term proportional to $1/\tau_c$ as described above.

$$\begin{aligned} \frac{dN_2}{dt} &= -B_0 \phi N_2 \\ \frac{d\phi}{dt} &= B_0 V \phi N_2 \end{aligned} \tag{3.25}$$

Rearranging the differentials and taking the ratio of the two equations we obtain a solvable differential equation that bounds ϕ to N_2.

$$\begin{aligned} &\begin{cases} dN_2 = -B_0 \phi N_2 dt \\ d\phi = B_0 V \phi N_2 dt \end{cases} \\ &\frac{d\phi}{dN_2} = -V \end{aligned} \tag{3.26}$$

The solution is simply

$$\phi(t) - \phi(0) = -V\left(N_2(t) - N_2(0)\right) \tag{3.27}$$

Substituting the boundary conditions of eq. (3.20) we have

$$\phi(t) = VR\tau - VN_2(t) \tag{3.28}$$

Substituting eq. (3.28) into (3.25) the differential problem is reduced to solving only one differential equation for N_2.

$$\begin{aligned} \frac{dN_2}{dt} &= -B_0\left(VR\tau - VN_2\right)N_2 \\ &= B_0 V {N_2}^2 - B_0 VR\tau N_2 \end{aligned} \tag{3.29}$$

The differential equation to solve is in the form

$$f'(t) - \alpha f^2(t) + \beta f(t) = 0 \tag{3.30}$$

It can be solved with the ansatz

$$\begin{aligned} f\left(t\right) &= a\left(b+e^{ct}\right)^{n} \\ f'\left(t\right) &= na\left(b+e^{ct}\right)^{n-1} ce^{ct} \\ f^{2}\left(t\right) &= a^{2}\left(b+e^{ct}\right)^{2n} \end{aligned} \tag{3.31}$$

Substituting

$$na\left(b+e^{ct}\right)^{n-1} ce^{ct} - \alpha a^{2}\left(b+e^{ct}\right)^{2n} + \beta a\left(b+e^{ct}\right)^{n} = 0 \tag{3.32}$$

In order the equation to be valid, the maximum order monomial of the first two terms must compensate each other. This implies $n=-1$ to have the same power. With some algebra we obtain

$$\begin{aligned} &-a\frac{1}{\left(b+e^{ct}\right)^{2}} ce^{ct} - \alpha a^{2}\frac{1}{\left(b+e^{ct}\right)^{2}} + \beta a\frac{1}{b+e^{ct}} = 0 \\ &-ace^{ct} - \alpha a^{2} + \beta a\left(b+e^{ct}\right) = 0 \\ &-ace^{ct} - \alpha a^{2} + \beta ab + \beta ae^{ct} = 0 \end{aligned} \tag{3.33}$$

The constant and exponential terms must compensate each other. Thus

$$\begin{aligned} &\alpha a^{2} - \beta ab = 0 \\ &\beta a - ac = 0 \end{aligned} \tag{3.34}$$

That implies

$$\begin{aligned} c &= \beta \\ a &= \beta \\ b &= \alpha \end{aligned} \tag{3.35}$$

Finally, the solution is

$$f\left(t\right) = \frac{\beta}{\alpha + e^{\beta t}} \tag{3.36}$$

which in terms of the original parameters

$$N_{2}\left(t\right) = \frac{R\tau}{1+\exp\left(B_{0}VR\tau t\right)} \tag{3.37}$$

From this expression we can derive $\phi(t)$ substituting (3.37) in (3.28).

$$\begin{aligned}\phi(t) &= VR\tau - \frac{VR\tau}{1+\exp(B_0 VR\tau t)} \\ &= \frac{VR\tau}{1+\exp(-B_0 VR\tau t)}\end{aligned} \tag{3.38}$$

We now see that in this approximation the number of photons in the cavity is not decreasing in time after the maximum is reached, because no loss term is present in the equations (see Figure 3-5).

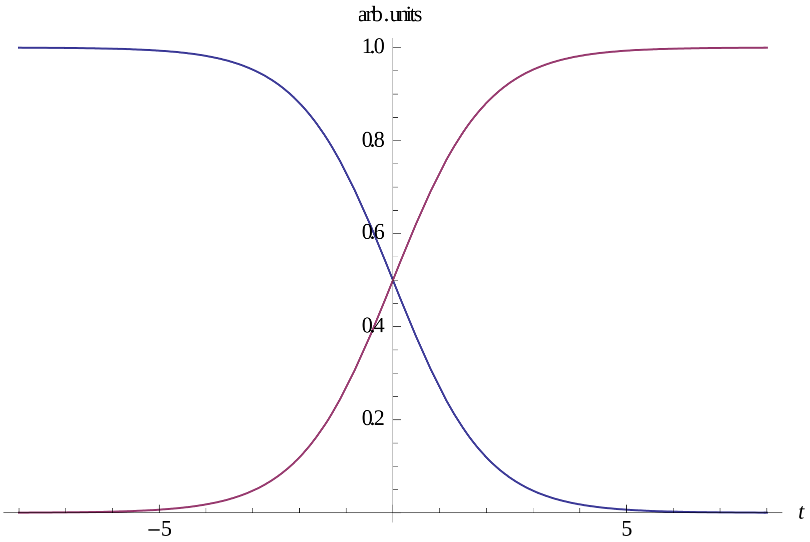

Figure 3-5: Population inversion (blue) and number of photons in cavity (purple) in the approximation of no loss term.

3.6.4 Analytical derivation of the shape of the pulse in the general case

In order to derive the analytical solution for the general problem, the loss term has to be reintroduced in the differential equation for the number of photons. The equation is solved again preserving the same dynamic for the population inversion. It is possible to take rid of the non-linear term in the equation exploiting the first rate equation:

$$\frac{dN_2}{dt} = -B_0 VR^2\tau^2 \frac{\exp(B_0 VR\tau t)}{\left(1+\exp(B_0 VR\tau t)\right)^2} = -B_0 \phi N_2 \tag{3.39}$$

Substitution in the second rate equation of the non-linear term yields a linear differential equation with constant coefficients.

$$\frac{d\phi}{dt} = B_0 V^2 R^2 \tau^2 \frac{\exp\left(B_0 V R \tau t\right)}{\left(1+\exp\left(B_0 V R \tau t\right)\right)^2} - \frac{1}{\tau_c}\phi \tag{3.40}$$

An analytical solution of this complex differential equation can actually be found with Fourier analysis, but this solution is extremely unpractical because of its dependence on the hyper-geometric function ${}_2F_1\left(a,b,c,z\right)$. A simpler solution will be derived below exploiting a further approximation. For reference, the general solution is

$$\phi\left(t\right) = RV\tau\left(1 - \frac{1}{1+\exp\left(B_0 V R \tau t\right)} - \frac{\exp\left(B_0 V R \tau t\right)}{1+B_0 V R \tau \tau_c} \cdot {}_2F_1\left(1, 1+\frac{1}{B_0 V R \tau \tau_c}, 2+\frac{1}{B_0 V R \tau \tau_c}, -e^{B_0 V R \tau t}\right)\right)$$

(3.41)

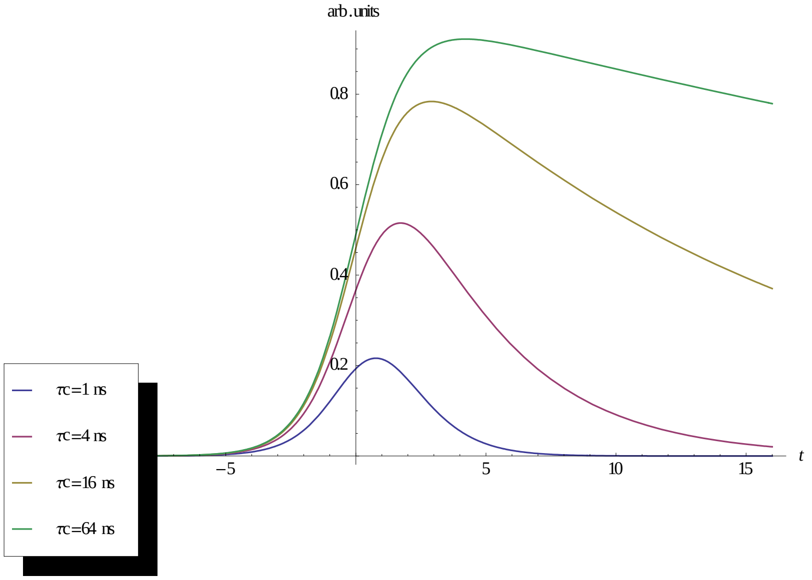

Figure 3-6: Pulse shape for different values of photon permanence time in the cavity τ_c obtained plotting the full analytical solution. All other cavity parameters B_0, V, τ, R are set to unity to graph the result.

For most practical cases, an easier but still quite general solution can be worked out approximating the derivative of the population inversion (3.39) with a Gaussian function, using the relation

$$\frac{e^x}{\left(1+e^x\right)^2} \approx \frac{1}{4}\exp\left(-\frac{x^2}{4}\right) \tag{3.42}$$

This relation can be easily verified using the Taylor series, and it is correct up to a correction of the fourth order.

$$\begin{aligned} \frac{e^x}{\left(1+e^x\right)^2} &= \frac{1}{4}-\frac{1}{16}t^2+\frac{1}{96}t^4+o\left(t^5\right) \\ \frac{1}{4}\exp\left(-\frac{x^2}{4}\right) &= \frac{1}{4}-\frac{1}{16}t^2+\frac{1}{128}t^4+o\left(t^5\right) \end{aligned} \tag{3.43}$$

Applying the relation (3.42) the derivative yields

$$\frac{dN_2}{dt} = -B_0VR^2\tau^2\frac{\exp\left(B_0VR\tau t\right)}{\left(1+\exp\left(B_0VR\tau t\right)\right)^2} \approx -\frac{B_0VR^2\tau^2}{4}\exp\left(-\frac{\left(B_0VR\tau\right)^2t^2}{4}\right) \tag{3.44}$$

Substitution in the second rate equation gives again a linear differential equation with constant coefficients.

$$\frac{d\phi}{dt} = \frac{B_0V^2R^2\tau^2}{4}\exp\left(-\frac{\left(B_0VR\tau\right)^2t^2}{4}\right)-\frac{1}{\tau_c}\phi \tag{3.45}$$

The solution of this differential equation can be found with Fourier analysis. Moving to the Fourier space requires much less computational effort than before, because the Fourier transform of the Gaussian force term is again a Gaussian. Using the Fourier transform of a Gaussian function

$$\int_{-\infty}^{+\infty}\frac{1}{\sqrt{2\pi}}e^{-i\omega\cdot t}e^{-\frac{1}{2}\frac{x^2}{\sigma^2}}dt = \sigma e^{-\frac{1}{2}\omega^2\sigma^2} \tag{3.46}$$

the expression of the differential equation in Fourier space results

$$-i\omega\tilde{\phi}+\frac{1}{\tau_c}\tilde{\phi}=\frac{B_0V^2R^2\tau^2}{4}\frac{\sqrt{2}}{B_0VR\tau}\exp\left(-\frac{\omega^2}{\left(B_0VR\tau\right)^2}\right)$$
$$=\frac{VR\tau}{2\sqrt{2}}\exp\left(-\frac{\omega^2}{\left(B_0VR\tau\right)^2}\right) \tag{3.47}$$

The solution in Fourier space is then

$$\tilde{\phi}=\frac{VR\tau}{2\sqrt{2}}\frac{\tau_c}{1-i\omega\tau_c}\exp\left(-\frac{\omega^2}{\left(B_0VR\tau\right)^2}\right) \tag{3.48}$$

The solution in real space can be found computing the inverse Fourier transform of (3.48) and carefully adjusting the boundary condition to match eq. (3.20). The calculation yields

$$\phi\left(t\right)=\frac{\sqrt{\pi}}{4}RV\tau\exp\left(\frac{1}{\left(B_0VR\tau\tau_c\right)^2}-\frac{t}{\tau_c}\right)\left[1+\operatorname{erf}\left(\frac{B_0VR\tau}{2}t-\frac{1}{B_0VR\tau\tau_c}\right)\right] \tag{3.49}$$

3.6.5 Comparison of analytical and numerical solutions

The approximated solution obtained with the Gaussian model (3.49) describes very well the pulse shape, in particular the raising edge region. However, the pulse maximum is slightly shifted down and in the past because of the removal of $1/\tau_c$ term that alters the time point in which $d\phi/dt=0$. (see Figure 3-7).

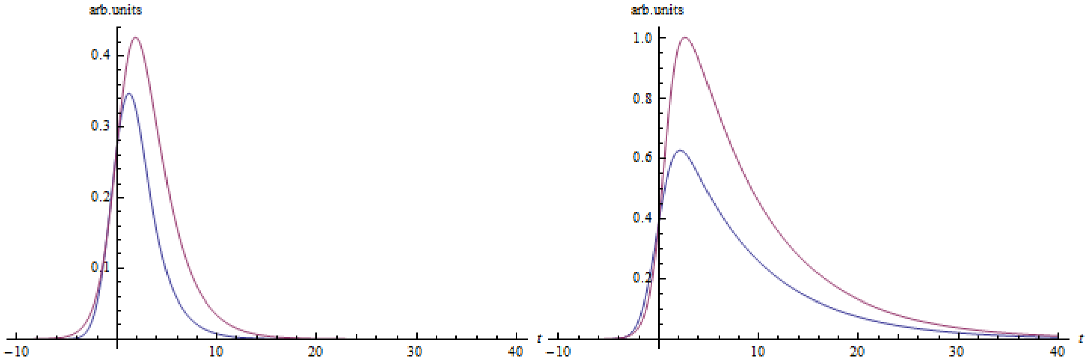

Figure 3-7: Numerical simulations of pulse shapes (purple) versus the analytical Gaussian model (blue) obtained for $\tau_c = 2ns$ and $\tau_c = 8ns$. All other cavity parameters B_0, V, τ, R are set to unity to graph the result.

A correcting scale factor on the vertical axis and a shift in time can be introduced to correct a posteriori the pulse peak position.

$$\phi_{corr}\left(t\right) = A \cdot \phi\left(t + t_0\right) \tag{3.50}$$

The results obtained for the pulse shapes corrected with (3.50) are shown in Figure 3-8. For $\tau_c \rightarrow 1$ the approximation starts to fail: the losses are so high that the population inversion shape is severely altered. In Figure 3-9 the correcting coefficients are plotted against τ_c, showing an asymptotic behavior for $\tau_c \rightarrow +\infty$.

In conclusion, it is possible to use the developed analytical model to fit the experimental data of the laser pulse shape and determine the parameters of the cavity. Note that if the measuring scale is arbitrary in the vertical direction (for example by using an oscilloscope to measure the differential potential of a photodiode), then no correction with a scale factor is needed because the scale is anyway arbitrary.

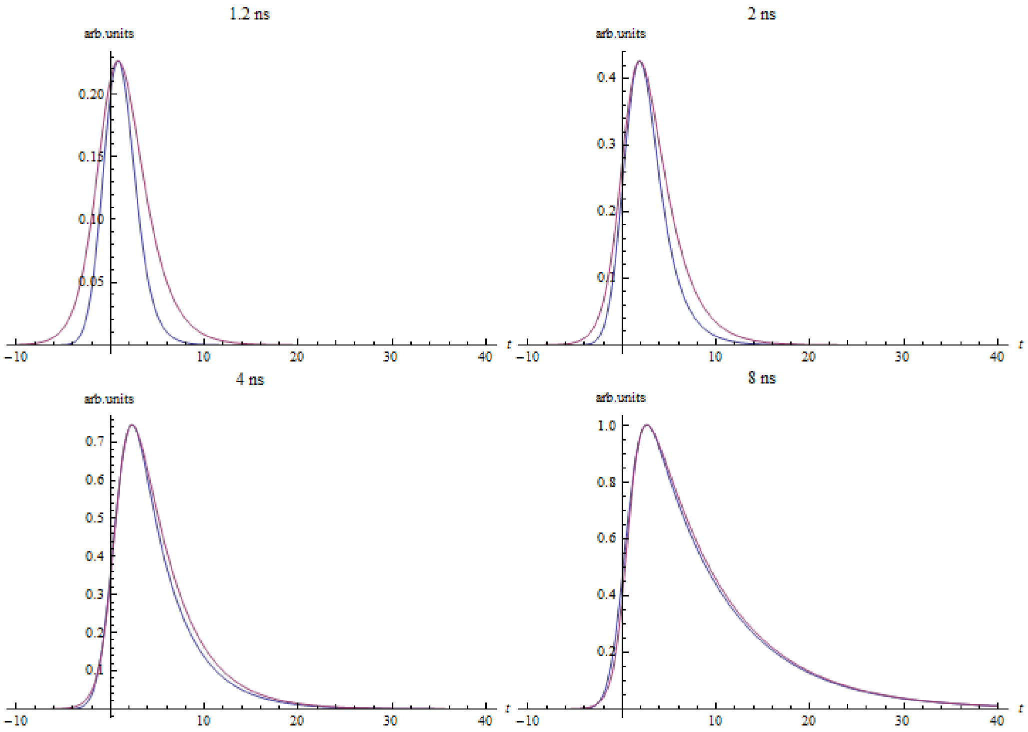

Figure 3-8: Numerical simulations of pulse shapes (purple) versus the analytical Gaussian model (blue) obtained for $\tau_c = 1.2ns, 2ns, 4ns, 8ns$; all other cavity parameters B_0, V, τ, R are set to unity to graph the result. The analytical models have been corrected by an arbitrary scale factor and a time delay to fit precisely the maximum position of the numerical simulations. The simulated pulse shape differs from the analytical model for low values of τ_c, where the approximation of N_2 independent of τ_c is starting to fail.

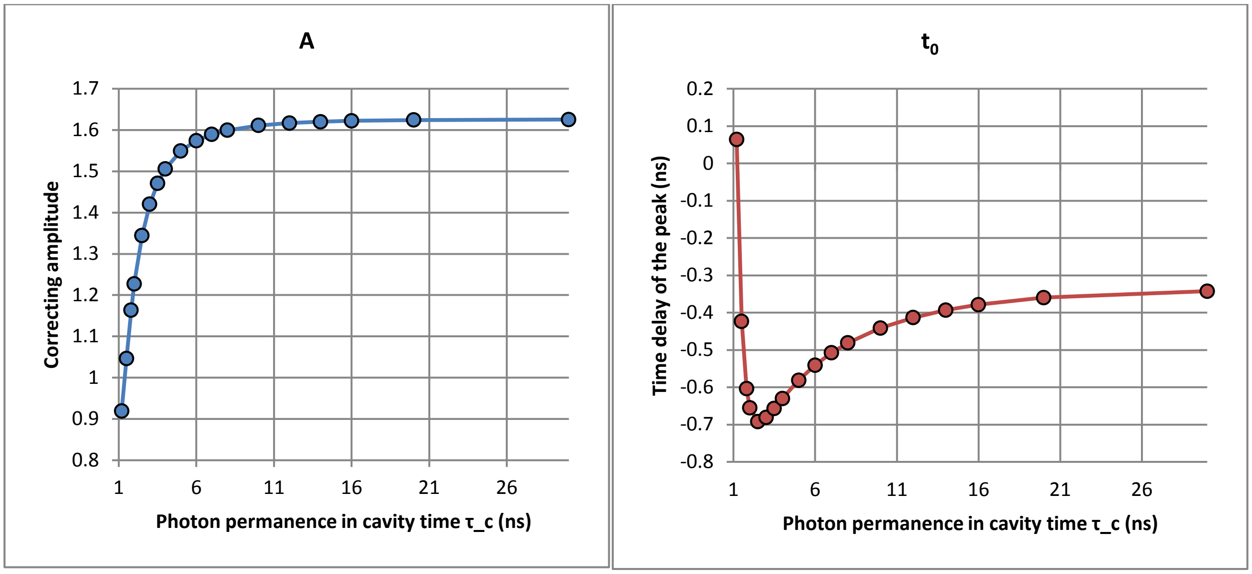

Figure 3-9: Profile for the correcting coefficients A and t_0 as a function of τ_c; all other cavity parameters B_0, V, τ, R are set to unity. For values of $\tau_c \rightarrow 1ns$ both coefficients show a vertical asymptote because the pulse is no more produced by the cavity due to high losses and the approximation of N_2 independent of τ_c clearly fails.

4 Theory of Positronium excitation

4.1 What is Positronium?

The goal of this section is to collect the main theoretical results about Positronium excitation both in weak and strong electric and magnetic fields to motivate the design choices made for the AEGIS laser apparatus. As a secondary goal, this chapter is minded to be a reference guide on the theory of Positronium excitation: most of the theoretical predictions discussed in the present chapter will be useful during the Positronium spectroscopy experiments, to compare the experimental results with the theory.

Positronium, or Ps for brevity, is the lightest bound state of two particles known. Its main characteristics can be synthesized as following:

- Ps is a purely leptonic hydrogenoid atom formed by an electron e^{-} and a positron e^{+} kept together only by electromagnetic interaction;
- Ps is lighter than any stable atom: $m_{Ps} = 2m_e \approx 1.022\,MeV$ compared to hydrogen $m_H = m_p + m_e \approx 938\,MeV$.
- Ps in the ground energy state exists in two different spin configurations: the para-Ps (with spin 0) and the ortho-Ps (with spin 1);
- Ps is an unstable atom that decays spontaneously with different channels depending on the spin configuration: para-Ps decays into two photons with an half-life of $125\,ps$; ortho-Ps decays into three photons with an half-life of $142\,ns$.

4.2 Positronium energy levels

The Hamiltonian describing a Ps atom in a static magnetic field $\mathbf{B} = B\mathbf{z}$, namely

$$\hat{H} = \hat{H}_C + \hat{H}_F + \hat{H}_Z + \hat{H}_{dia} + \hat{H}_{MS} \tag{4.1}$$

is the sum of the following terms:

1. The hydrogen-like term, $\hat{H}_C$, of a two particle system with opposite electric charges $+e$ and $-e$ interacting with a Coulomb potential;
2. A contribution from the spin-orbit and spin-spin interactions, $\hat{H}_F$, that take into account the relativistic effects and produces the fine structure of the atom;

3. The first order $\hat{H}_Z$ and second order $\hat{H}_{dia}$ interactions with the magnetic field, being the Zeeman effect term and the diamagnetic term;
4. The motional Stark effect term, $\hat{H}_{MS}$, that includes the Stark effect due to the electric field induced by the motion of the atom in the external magnetic field.

A common choice for quantum numbers, usually exploited when performing the calculations for the hydrogen energy levels, includes the unperturbed atomic quantum numbers n, l, m and the total spin quantum numbers s, m_s. In the Ps case the bare energy levels are exactly $1/2$ of the corresponding hydrogenic levels due to the reduced mass $m_e \to m_e/2$ governing the dynamics. The energy of the bare energy levels is given by the well-known Balmer formula (see for example [Bethe 1957 sect. 2]). A fine structure energy correction ΔE_F due to relativistic spin-spin and spin-orbital momentum couplings is usually added. The energy structure of Ps up to the first three levels can be found in Figure 4-1.

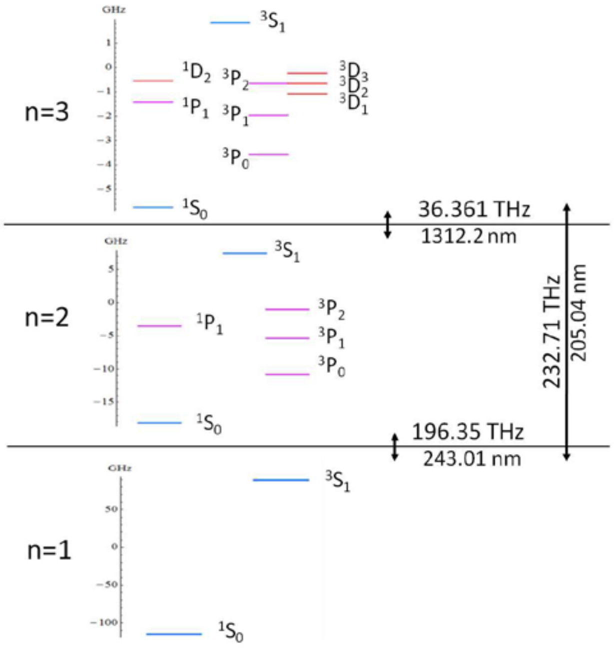

Figure 4-1: Energy level structure of Positronium up to the third excited level without external fields.

However, to properly model the experimental conditions of the spectroscopy experiment, the contributions introduced by the presence of the external magnetic field have to be considered. These new terms cause an enormous increase of complexity to carry on the exact calculations; the exact solution for the energy splitting for arbitrary external magnetic field has been di $\tau = \frac{1}{A}$ discussed by [Villa 2010] for $n \leq 3$, where the number of terms (36) is still under human control.

In fact, there is no real need to perform exact calculations and a simpler perturbative treatment can be enough to grasp the physics and discuss the splitting of energy levels. Within this approximation, a simpler perturbative treatment is enough to discuss the splitting of energy levels. Adding to the energy levels all the possibly relevant correction terms leads to the following energy structure for Ps:

$$E\left(n,l,m,s,m_s\right) = -\frac{m_e c^2 \alpha^2}{2}\frac{1}{2n^2} + \Delta E_F\left(n,l,s\right) + \Delta E_Z\left(s,m_s\right) + \Delta E_{dia}\left(n,l,m\right) + \Delta E_{MS} \tag{4.2}$$

1. The expression for the fine structure energy correction ΔE_F can be derived either from bare Dirac theory (see [Bethe 1957 sect. 23]) or from non-relativistic QED (see [Pineda 1998]).

$$\begin{aligned}
&\Delta E_F\left(n,l,s\right) = -\frac{m_e c^2 \alpha^2}{2}\alpha^2\left[\frac{11}{32n^4} + \left(\varepsilon\left(l,s,j\right) - \frac{1}{2l-1}\right)\frac{1}{n^3}\right] \\
&\varepsilon\left(l,s=0,j\right) = 0 \\
&\varepsilon\left(l,s=1,j\right) = \frac{7}{6}\delta_{l0} + \frac{1-\delta_{l0}}{2\left(2l+1\right)}\begin{Bmatrix} \frac{3l+4}{\left(l+1\right)\left(2l+3\right)} & \text{if} \quad J = l+1 \\ -\frac{1}{l\left(l+1\right)} & \text{if} \quad J = l \\ -\frac{3l-1}{l\left(2l-1\right)} & \text{if} \quad J = l-1 \end{Bmatrix}
\end{aligned} \tag{4.3}$$

This term is $\alpha^2 / n \approx 10^{-4} / n$ smaller than the bare energy level, and can be neglected with respect to magnetic contributions for $n \geq 3$.

2. The Zeeman energy splitting ΔE_Z turns out to be negligible with respect to the motional Stark contribution. First, in the center of mass system the orbital motion terms of positron and electron cancel each other leading to a null contribution from the magnetic interaction with orbital motion. The spin contribution to the energy splitting at its maximum value for $B = 1T$ yields

$$\max_{s,m_s}\left(\Delta E_Z\right) = 4\mu_B B \approx 2.4 \cdot 10^{-4}\, eV \tag{4.4}$$

3. The diamagnetic term plays a significant role only for very high fields $B > 100\,T$.

   With a_0 being the Bohr radius and $f\left(n,l,m\right)$ a numerical factor proportional to n^4, the contribution is

$$\Delta E_{dia}\left(n,l,m\right) = \frac{e^2 B^2 {a_0}^2}{m_e} f\left(n,l,m\right) \tag{4.5}$$

   For Ps it plays a relevant role only for $n > 40$, that is beyond the ionization limit of $n > 27$, resulting in an enhanced ionization probability.

4. The motional Stark energy splitting arises from the coupling of the Ps atom with the induced electric field due to the rest frame drag in the external magnetic field:

$$\mathbf{E}' = \gamma\left(\frac{\mathbf{u}}{c} \times \mathbf{B}\right) \tag{4.6}$$

   This transverse electric field acts on the moving Ps, thus adding an interaction term that can be written as a Stark Hamiltonian.

$$\hat{H}_{MS} = -e\left(\mathbf{r} \cdot \mathbf{E}'\right) \tag{4.7}$$

   Ps is therefore interacting with orthogonal electric and magnetic fields; the matrix elements of $\hat{H}_{MS}$ are different from zero for every value of l and m; no better choice of quantum numbers to analytically solve the problem is currently known. An upper bound on maximum energy splitting can be derived with the usual Stark effect theory, assuming that Ps atoms are in thermal equilibrium at temperature T. This leads to

$$\Delta E_{MS} = 6ea_0 n\left(n-1\right)B\sqrt{\frac{k_B T}{2m_e}} \tag{4.8}$$

At a reference temperature of $T = 100\,K$ and a magnetic field of $B = 1T$ the induced electric field can be higher as $E \approx 275\ V\ /\ cm$, lowering sensibly the ionization limit for Ps with respect to hydrogen. In fact, the ionization starts affecting Ps for $n > 27$, while in the case of hydrogen $n > 87$. This is an upper limit for Rydberg state excitation. More important, the energy splitting ΔE_{MS} becomes dominant over the other splittings for $n > 6$ (see Figure 4-2).

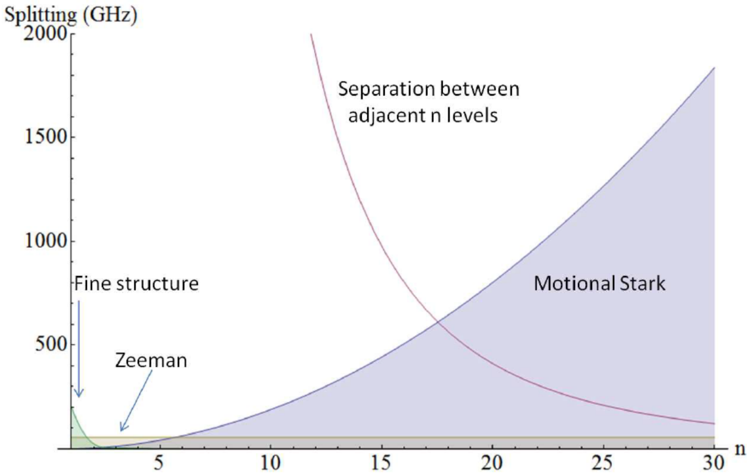

Figure 4-2: Maximum energy splitting due to fine structure (green), Zeeman effect (brown) and motional Stark effect (blue) for 1 T magnetic field and 100 K thermalized Ps. Courtesy of [Villa 2010].

4.3 Exciting Positronium

4.3.1 Exciting Positronium to $n = 3$

The excitation of Positronium to the third excited state is performed via photon absorption by the ortho-Ps atoms produced by the converter in the ground state:

$$Ps + \gamma \longrightarrow Ps^* \tag{4.9}$$

The precise transition wavelength for the absorption process, together with its line width eventually due to Doppler and motional Stark effects, has been carefully calculated by [Castelli 2009] (considering all the possible effects included in (4.2)) and read:

$$\lambda_{1\to 3} = 205.045(2)\,nm \tag{4.10}$$

where $\left(2\right)$ is the uncertainty on the last cipher due to the motional Stark splitting of the sublevels.

Calculations of Positronium excited and ground state dynamics in time is of great interest for the spectroscopy experiment. As explained in the following paragraphs, the detection of the excited fraction of Positronium will be carried out by observing a peak in the lifetime distribution, whose characteristics depend strictly on the amount of atoms produced in each excited sublevel.

In Chapter 3 the rate equations model for the case of a two level atom interacting with a resonant laser pulse is described in details. The model, thanks to its simplicity, has proven to be very effective in describing interaction dynamics. The mathematical framework to describe the excitation of an atomic population to higher energy states can be developed in a very similar fashion, providing that more populations have to be considered, together with level energy splitting and line broadening of the pumping radiation. The leading effect in the rate equations is absorption of a laser photon from a ground state Ps atom that undergoes in the transition to an excited state with the same stored energy as the incoming photon.

There are a total of 36 energy sublevels for $n = 3$, and their degeneracy can be fully removed by the splitting terms (the fine structure term and the Zeeman term, as depicted in Figure 4-2). The effect of the motional Stark term is mainly that of sublevel mixing, allowing transitions otherwise neglected by dipole electric selection rule. Hence, for each sublevel, a different population was considered together with a rate equation describing its dynamics. Two effects play a significant role in the process: the absorption of pump photons and the decay from higher excited states to lower excited states. In Figure 4-3 an example of the excited level populations as a function of time are shown. All the simulations were performed during the experiment design period with a pulse spectral width of $117\,GHz$ and $5\mu J$ pulse energy. Current measurements on the laser apparatus show that the spectral width is $300\,GHz$ and the pulse energy is over $75\mu J$, much above the budgeted conditions. Numerical results obtained with such conditions (see Figure 4-4) show that approximately 65% of the Positronium hit by the laser pulse should be excited to $n = 3$. This increased efficiency, with respect to the 50% efficiency obtained with the two-level theory without the motional Stark effect, is tightly bounded to Positronium velocity. The more velocity, the more motional Stark mixes the levels, having more sublevels with high enough stimulated transition rate to be excited, thus increasing the population fraction on n=3. For Positronium faster than $3 \cdot 10^5\, m/s$ the motional Stark broadening becomes dominant and the spectrum becomes bigger than the laser one. The population fraction on n=3 saturates as portions of the spectrum go beyond laser spectral width.

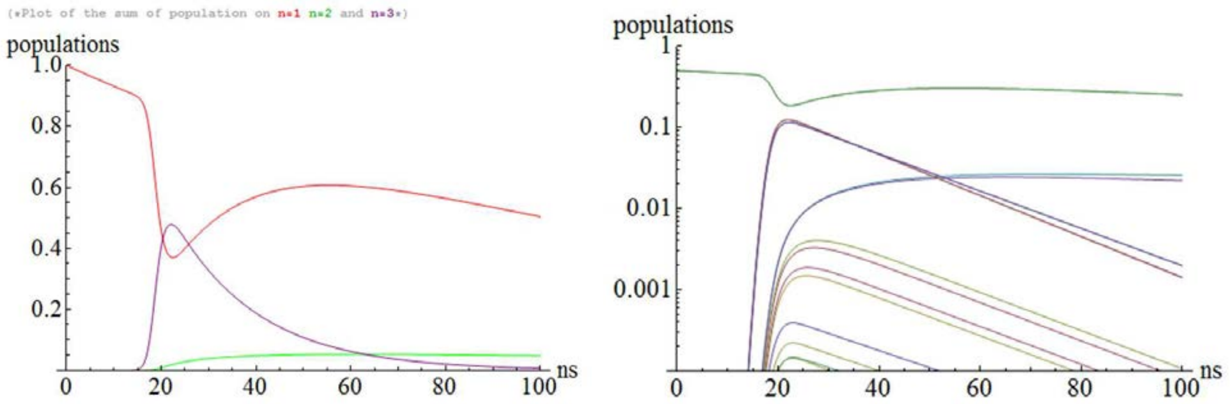

Figure 4-3: Cumulative population for n=1 (red), n=2 (green) and n=3 (purple) obtained summing up the contributions from all the sublevel populations (left) and contributions from each sublevel (right). Simulations are obtained with 5 μJ laser energy, 117 GHz spectrum and, 4 ns pulse and $5 \cdot 10^4\ m/s$ Ps velocity. Courtesy of [Villa 2010].

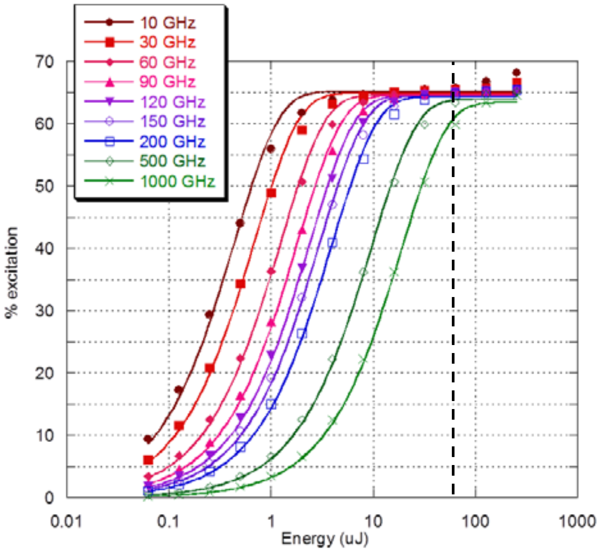

Figure 4-4: Maximum excitation efficiency as a function of pulse energy for different laser spectral widths. All the simulations are obtained in AEGIS working conditions, with 1 T magnetic field and $5 \cdot 10^4 m/s$ Ps velocity. At the present level of pulse energy (dashed black line), all the curves are in the saturation region close to the asymptotic value of 65% excitation efficiency. Courtesy of [Villa 2010]

4.3.2 Exciting Positronium to n > 20

The excitation of Positronium to Rydberg levels is performed starting from the third excited state, again via photon absorption by the ortho-Ps atoms produced by the converter in the ground state. The wavelength of the photon spans in the range $1650 \div 1750\,nm$ depending on the targeted Rydberg level.

Exciting Positronium to Rydberg levels means dealing with a huge number of sublevels (see Figure 4-5). Their degeneracy is totally removed by the various magnetic effects, and in particular by the dominating motional Stark effect which spans sublevel energies over a large line width for $n > 6$.This has the consequence of an interleaving of sublevels belonging to different n shells, as shown in (see Figure 4-2) where the interleaving starts from $n = 16$, at variance with the energy level structure for lower n.

Exact calculations of transition efficiencies in such a forest of sublevels require a significant computational effort beyond the present interest for accuracy.

A simpler rate equations model can be developed in the approximation of a quasi-continuum of energy levels – a sort of Rydberg level band – introducing a density of energy levels per unit frequency. This approximation holds if the Stark effect is high enough to mix all the sublevels from different values of n as shown in Figure 4-5. The calculations thus follow the same guidelines as the optical excitation of a level band.

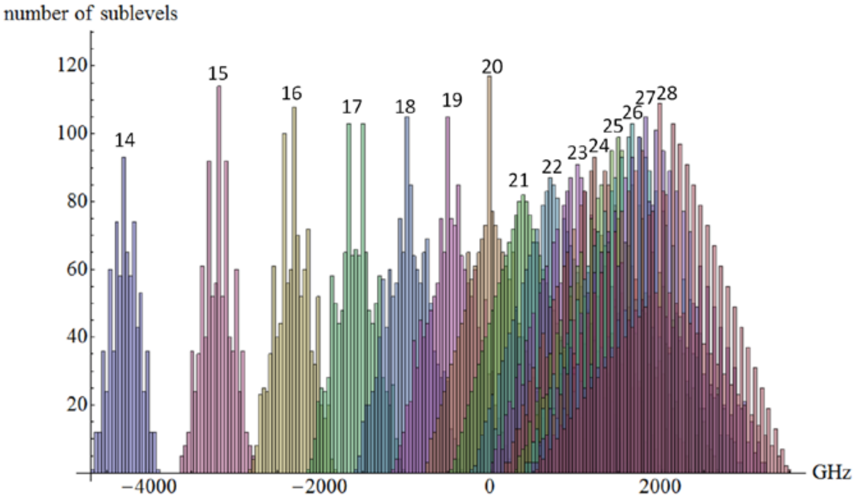

Figure 4-5: Histogram of the number of sublevels between n=14 and n=28; each bin is 40 GHz wide. The histogram is centered on the frequency of the 3 → 20 transition. Courtesy of [Villa 2010].

Results obtained by [Castelli 2009] show that in the Rydberg region of the spectrum the absorption probability is independent of n and the transverse Ps velocity. This is a rather impressive result: the required laser fluence (the energy density per unit squared centimeter) can be almost the same for exciting any interval of the Rydberg level band (see Figure 4-6).

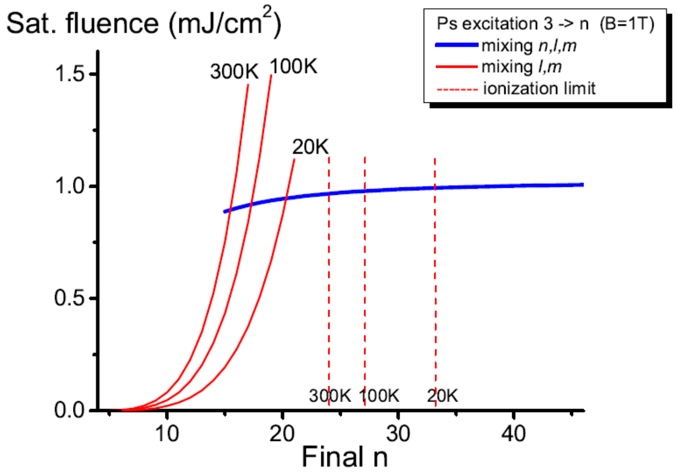

Figure 4-6: Saturation fluence for Rydberg band transitions $3 \rightarrow n$ calculated at different Ps temperatures. The blue curve, obtained mixing all the excited levels, is almost constant in the whole Rydberg levels region. Courtesy of [Castelli 2009]

4.3.3 Required laser-pulse energies

It is practical to define saturation fluence as the total pulse energy for unit target area whereby 43% of excitation efficiency is obtained (see [Castelli 2009]).

For the case $n = 3$, an analytical expression for the saturation fluence can be worked out

$$F_{1\to 3} = \frac{c^2}{B_{1\to 3}} \sqrt{\frac{2\pi^3}{\log(2)}} \frac{\Delta\lambda}{\lambda^2} \tag{4.11}$$

where $B_{1\to 3}$ is the Einstein coefficient for the transition. On the contrary, the Rydberg levels saturation fluence is found to be constant within the continuum energy-band approximation, with a value of

$$F_{3\to R} = 0.9 \div 1.0 \ mJ \ / \ cm^2 \tag{4.12}$$

From equations (4.11) and (4.12) the constraints on the laser pulse energies can be worked out. The laser pulses were assumed to be Gaussian in profile with a spot of $d = 2.8\,mm$ in diameter (FWHM) and a time duration of $\tau = 4\,ns$. The fluence at the peak of the Gaussian was fixed to $F_{peak} = 4F_{sat}$ to saturate the transition in the whole diameter profile. In the following

Table 1 the required energies are summarized.

Transition	Wavelength	Saturation energy
$1 \longrightarrow 3$	$205\,nm$	$32\,\mu J$
$3 \longrightarrow 25$	$1664\,nm$	$350\,\mu J$

Table 1: Energies required from the laser pulse to efficiently excite Positronium saturating the transition.

4.4 Lifetime of Positronium excited states

Positronium excited states have longer lifetimes with respect to the ground state. In order the annihilation process to happen, indeed, the excited Positronium must first decay back to its ground level. This effect of Positronium excitation on the lifetime will be the key for a direct measurement of the gravitational coupling of antimatter on Positronium, as pointed out by [Mills 2002].

Enhanced lifetimes are very useful for the AEGIS antimatter experiment, where the excited Ps cloud must travel in vacuum for a small distance before entering in the antihydrogen formation trap.

The lifetime of hydrogenic excited levels is known in literature. A simple but effective expression to calculate lifetimes in agree with experiments within 10% is (see [Chang 1985])

$$\tau\left(n,l\right) = \frac{3 \cdot 10^{14} \hbar^3}{2\mu\alpha^3 Z^4 e^4} n^3 \left(l + \frac{1}{2}\right)^2 \qquad (4.13)$$

where μ is the reduced mass and Z is the number of positive charges (one, in this case). The factor 10^{14} is introduced to bring the original CGS expression into MKS units. Neglecting higher-order level splitting, because of electric dipole selection rules only transitions with $\Delta l = \pm 1$ can be achieved. Thus, $n = 3$ excited atoms have $l = 1$, while Rydberg excited atoms have $l = 0,2$. In

Table 2 and Figure 4-7 the expected lifetimes for the transitions of interest are summarized.

Energy level configuration (n, l)		Lifetime (ns)	Energy level configuration (n, l)		Lifetime (us)
3	1	11.3			
12	0	80.4	**12**	2	2.01
13	0	102	**13**	2	2.56
14	0	128	**14**	2	3.19
15	0	157	**15**	2	3.93
16	0	191	**16**	2	4.77
17	0	229	**17**	2	5.72
18	0	271	**18**	2	6.79
19	0	319	**19**	2	7.98
20	0	372	**20**	2	9.31
21	0	431	**21**	2	10.8
22	0	496	**22**	2	12.4
23	0	566	**23**	2	14.2
24	0	643	**24**	2	16.1
25	0	727	**25**	2	18.2
26	0	818	**26**	2	20.5
27	0	916	**27**	2	22.9

Table 2: Expected lifetimes within 10% for excited Positronium energy levels. Lifetimes for the l=2 states are given in microseconds.

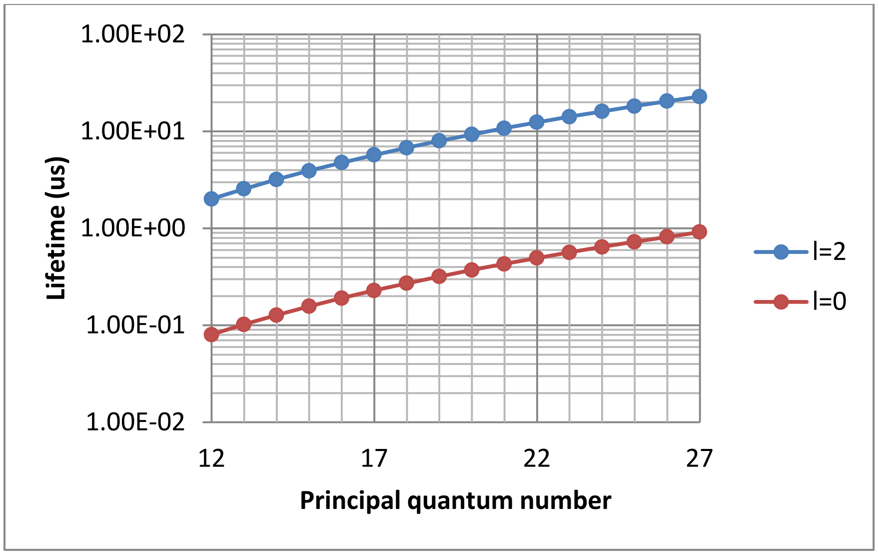

Figure 4-7: Expected excited state lifetimes as a function of the principal quantum number for the two expected values of orbital quantum number

4.5 Measurement of the excited fraction of Positronium from the annihilation peak

The measurement of the excited fraction of Positronium is carried out exploiting the different lifetime of excited atoms. Fast Cherenkov light detectors (PbF_2 or BaF_2, typically) are connected to a multichannel analyzer triggered by the signal from the annihilation peak of the para-Ps inside the converter. They are tuned to detect selectively the $511 keV$ γ-rays produced by the annihilation of para-Ps and histogram the number of annihilations as a function of the delay time from the triggering signal. Without the laser powered on, it is expected to measure a sharp peak corresponding to the annihilation peak inside the converter followed by a long exponentially decreasing tail due to decays of ortho-Ps in the same energy range detected by the scintillators.

In the Positronium spectroscopy experiment, after the UV pulse is turned on, thus pumping the transition $1 \rightarrow 3$, an excess of low-lifetime annihilations is expected. This is mainly caused by the presence of a relatively weak external magnetic field (less than $0.01T$) that induces Zeeman mixing of fine structure sublevel states with m=0. For example, the 1^3S_1

ortho-Ps state can be excited to a third level state with the following (only descriptive) steps:

$$1^3S_1 \xrightarrow{dipole} 3^3P_1 \xrightarrow{mixing} 3^1P_1 \tag{4.14}$$

Then 3^1P_1 decays to 1^1S_1, the para-Ps, annihilating immediately. Thus exciting $n = 3$, as well as higher levels, produces an excess of annihilations in the $511 keV$ channel corresponding to the lifetime of the produced state.

Note that this phenomenon is absent in presence of a strong magnetic field ($0.2T$ or above) because, in this case, fine structure is negligible and spins are “frozen” to their energy sublevel.

Measurements of this kind demonstrating Ps excitation were performed in [Cassidy 2012] using the $1 \to 2 \to 12$ chain of excitations (see Figure 4-8, frame on the left). When the laser UV radiation is turned on, the $n = 2$ level becomes populated and an excess of annihilations in the low lifetime region is observed due to the Zeeman splitting. The excess at low lifetimes is compensated by a long tile in the high lifetime region with a lower number of annihilations. The expected lifetime of $n = 3$ is $\tau_3 = 11.3\ ns$ (see Table 2), that is compatible with an excess of events within the annihilation peak inside the converter.

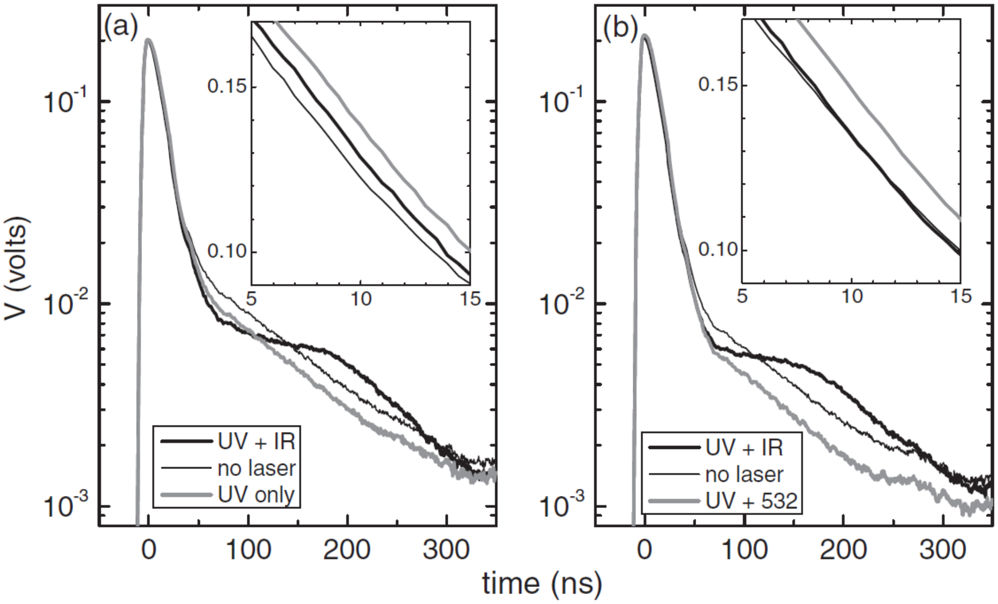

Figure 4-8: Excited Positronium lifetime spectra measured with 0.16 T (left) and 1 T (right) magnetic fields for different laser configurations as indicated in the legend. The selected transitions are 1 → 2 (UV) and 2 → 12 (IR). Courtesy of [Cassidy 2012].

When the IR pulse is turned on, some atoms in $n = 3$ start being excited to $n = 12$. An excess of annihilation events due to the impact of the Ps atom with the walls of the experimental chamber, is expected starting from $80.4\,ns$ up to $2.01\ \mu s$ (black line in Figure 4-8), witnessing the presence of long lifetime (Rydberg) Positronium.

The behavior is similar to the case of a strong magnetic field (see Figure 4-8, frame on the right). Due to the absence of the triplet-singlet mixing, the detection of the n=3 excitation is performed by ionization with a suitable laser pulse.

5 The laser apparatus to excite Positronium

5.1 Requirements

The laser apparatus was developed in order to fulfill the following requirements:

1. Provide an impulse in the UV region of the spectrum with $\lambda = 205.035\,nm$ to match the transition $1 \rightarrow 3$ of Positronium at $100K$ temperature;
2. Provide an impulse in the IR region of the spectrum, where λ is in the range between $1650\,nm$ and $1700\,nm$ to excite Positronium to Rydberg levels up to $n = 27$, the ionization limit;
3. Fulfill the energy requirements summarized in Table 1 for both the impulses;
4. Fulfill the time duration requirements ($\tau = 4\,ns$) to match the numerical simulations of Positronium excitation;
5. Fulfill the fluence requirements of equations **(4.11)** and **(4.12)** with a beam size of $d = 3\,mm$;
6. Provide the correct synchronization of the pulses to excite contemporaneously the Positronium;
7. Provide the correct synchronization of the pulses with very low fluctuation with respect to the Positronium cloud exiting from the converter.

Requirements from 1 to 4 impose constraints over the laser apparatus, which is described in detail in this chapter. Requirements 5 and 6 are relative to the laser transport line, discussed in Chapter 5. The last requirement is fulfilled by introducing the synchronization device, described in Chapter 6.

5.2 Scheme of the apparatus

The source of the laser light in the AEGIS apparatus is a Q-Switched Nd:YAG laser that provides three pulses at three different wavelength, $1064\,nm$, $532\,nm$ and $266\,nm$, corresponding to the first, second and fourth harmonic of the Nd:YAG laser radiation. The internal characteristics of the pump laser are described in the following section. After that, two separate and independent lines take care of producing the required IR and UV wavelengths. The block scheme of AEGIS laser apparatus, shown in Figure 5-1, is made of three different breadboards:

1. **Pump laser breadboard**: the Q-Switched pumped laser is installed on the first breadboard, together with three vertical periscopes to bring the radiation at the correct vertical height and twist the polarization to the horizontal plane.
2. **IR line breadboard**: on the second breadboard, the $1064\,nm$ is converted to the desired IR wavelength in the range $1650-1750\,nm$. The conversion is performed in two stages: first, the correct wavelength is generated within an optical parametric generation crystal (OPG); then, the pulse is amplified by two optical parametric amplification crystals (OPAs). Finally, a dichroic mirror filters the non-useful $1064\,nm$ radiation and leaves only the amplified impulse.
3. **UV line breadboard:** on the third breadboard, the $205\,nm$ radiation is produced performing optical frequency sum in a non-linear crystal, the main source of power being the UV impulse produced by the laser. In order to produce $205\,nm$ the choice of the second frequency is constrained by the sum of reciprocals:

$$\begin{aligned} \frac{1}{205\,nm} &= \frac{1}{266\,nm}+\frac{1}{X\,nm} \\ X &= 894\,nm \end{aligned} \tag{5.1}$$

Thus, an OPG-OPA system similar to the one exploited in the IR breadboard is introduced to produce the $894\,nm$ impulse. The source of power in this case is the $532\,nm$ impulse coming from the laser.

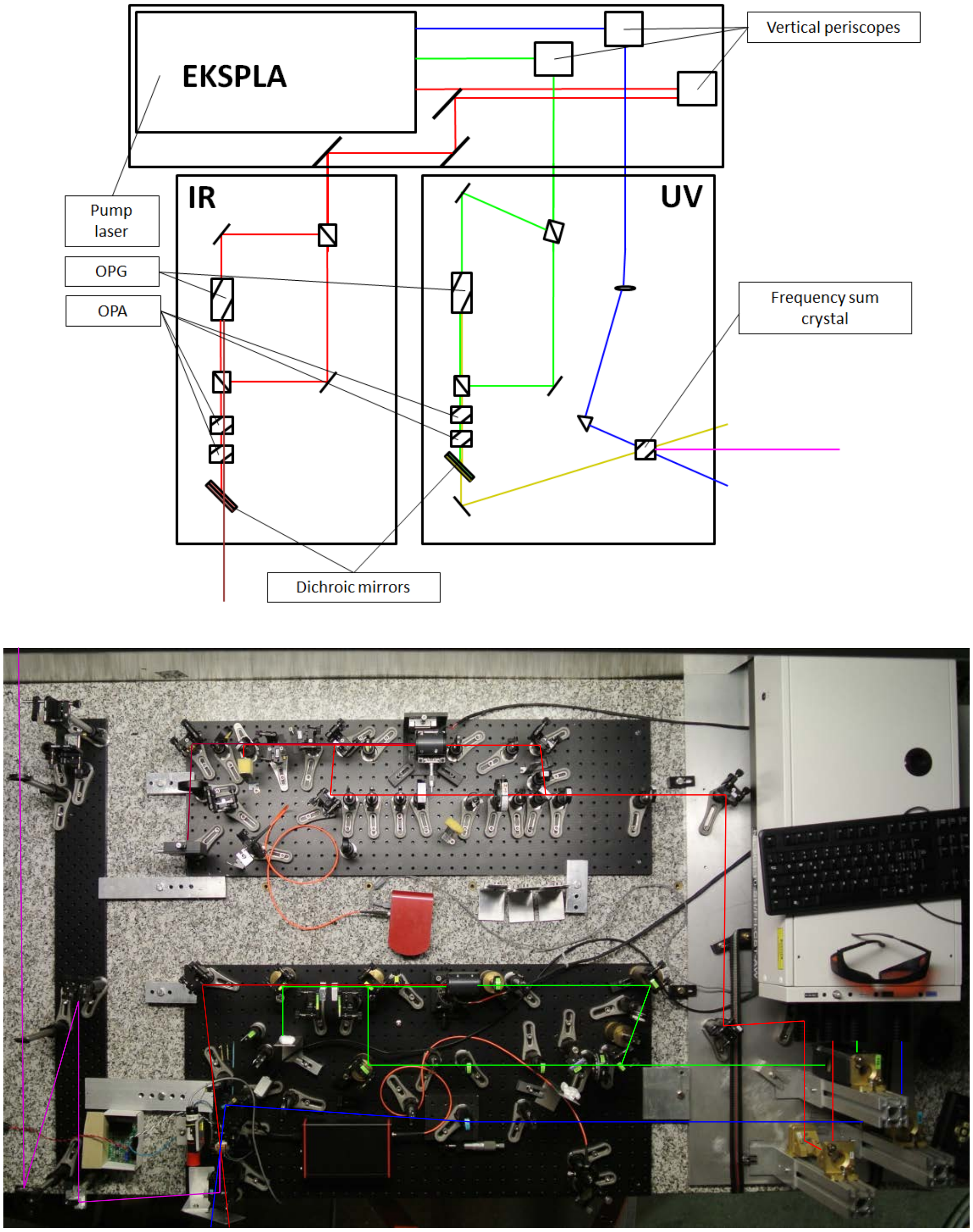

Figure 5-1: Block scheme and photograph of the AEGIS laser apparatus after the commissioning at CERN with the antihydrogen experiment delay line.

5.3 The AEGIS Q-Switched laser

The first macro-component of the laser apparatus is the Q-Switched laser itself. In this paragraph the main characteristics of AEGIS Q-Switched laser are discussed. The principal cavity parameters are determined fitting the analytical model developed in Chapter 3 to the data measured with a fast photodiode. Then, a description of the second and fourth harmonic generator is given including the measured powers obtained with the apparatus.

5.3.1 Overview of the laser

The AEGIS Q-Switched laser is a custom-made IR pumped laser assembly by the Estonian manufacturer EKSPLA, which includes extra-cavity second harmonic generation (SHG) and fourth harmonic generation (FHG) by non-linear KTP crystals. It consists in the following parts, as shown in Figure 5-2:

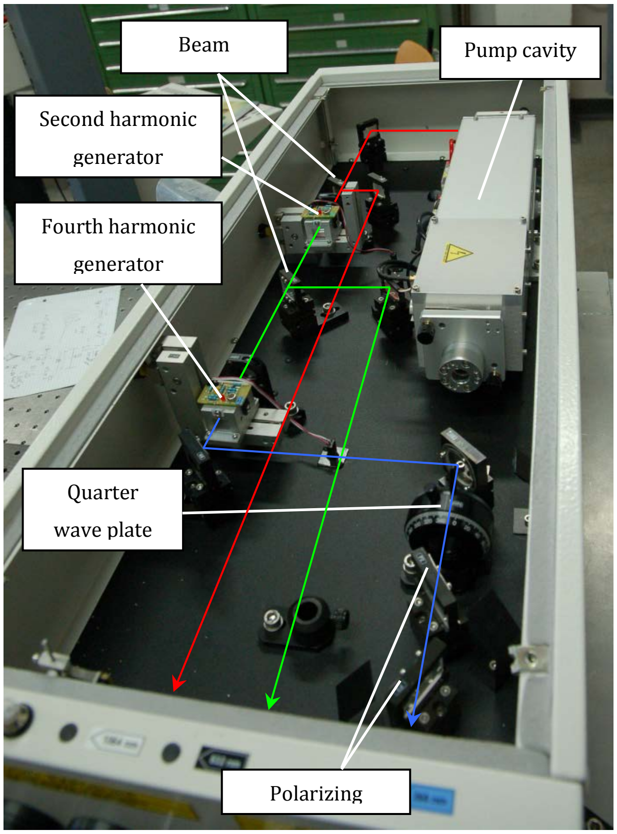

Figure 5-2: Internals of the AEGIS Q-Switched laser

1. **Pump cavity:** it is the active core of the Q-Switched laser. It provides the high-energy laser pulse that excites the non-linear crystals to form the second and the fourth harmonic wavelength;

2. **Beam splitter:** splits 80-20% the energy of the IR pulse. The lower fraction is outputted from the laser; the higher fraction enters in the second harmonic generator;
3. **SHG:** the second harmonic generator is a KTP non-linear crystal, phase matched to convert two photons at $\lambda = 1064\,nm$ into one photon at $\lambda = 532\,nm$;
4. **Beam splitter:** splits 50-50% the energy of the green pulse and transmits the spurious $1064\,nm$ background. Again, the first half is outputted from the laser, while the second half enters in the fourth harmonic generator;
5. **FHG:** the fourth harmonic generator is again a KTP non-linear crystal, phase matched to convert two photons at $\lambda = 532\,nm$ into one photon at $\lambda = 266\,nm$;
6. **UV Polarization adjustment:** before leaving the laser, the polarization of the UV pulse is twisted to the vertical direction by a quarter wave plate and the spurious polarization components filtered away by two Brewster plates.

5.3.2 Laser-cavity characteristics

The pump laser cavity is an EKSPLA NL303-10 Q-Switched Nd:YAG cavity operating in the near-IR at $\lambda = 1064\,nm$. One of the two reflecting mirrors is slightly convex, making the cavity unstable for continuous usage, but very effective for Q-Switched usage: the beam in radial direction is substantially bigger with respect to a stable cavity. The resulting beam is circular with a top-hat profile of $1\,cm$ in diameter, although being a single mode in the radial direction. In

Table 3 the principal characteristics of the cavity are collected.

EKSPLA NL303-10 characteristics	
Active medium	Nd:YAG
Wavelength	$1064\,nm$
Pulse duration	$4.0 \pm 0.3\,ns$ at 100% pump level
Pulse energy (max)	$800\,mJ$
Pump type	High power halogen gas flash lamp
Pump power	Tunable to more than 200 W
Max. operating frequency	10 Hz
Nd:YAG rod length	$114.4 \pm 3.8\,mm$
Nd:YAG rod radius	$3.35 \pm 0.13\,mm$
Effective cavity length (mirror-mirror)	$500 \pm 15\,mm$
Beam radial diameter	$10.0 \pm 0.5\,mm$
Beam radial profile	Top-hat function
Jitter trigger signal-pulse shot	$< 0.3\ ns$ (instrument limited)
Free spectral range	$300 \pm 10\,MHz$
Spatial structure	single modal (top-hat profile)
Spectral structure	multi modal

Table 3: Principal characteristics of the ESKPLA pump cavity

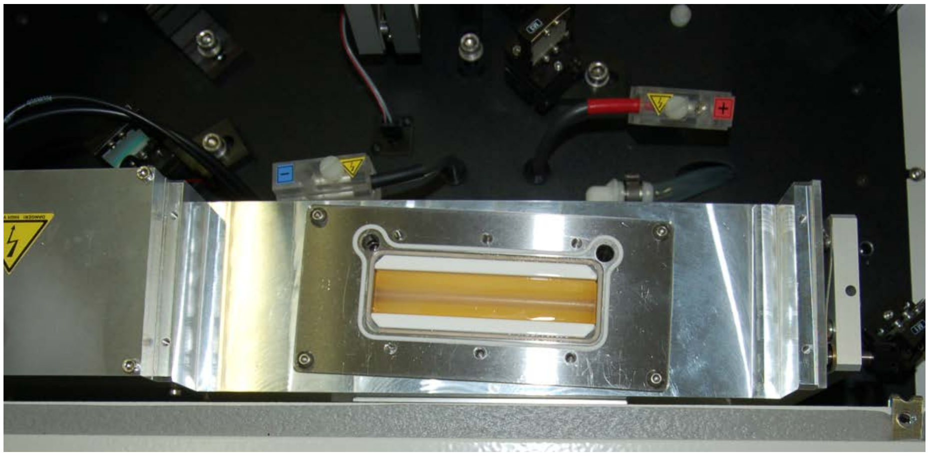

Figure 5-3: The exposed Nd:YAG rod during a service opening of the laser cavity to substitute the flash lamp.

5.3.3 Timing constraints

EKSPLA cavity operates with a constant pulse repetition rate up to $10\,Hz$; the main limiting factor is the time needed to recharge the capacitor pack that provides the power to the flash lamp. Capacitors have high capacity to store enough energy to light the lamp, so the power supply starts recharging them much before the master clock activates the flash lamp. If capacitors don't discharge quickly lighting up the lamp, they progressively heat up because of self-discharge damaging their dielectric film. This imposes a serious constraint on timing: once a repetition rate is established, only little variations can be made at runtime, in the order of 10% or less.

This constraint is the primary reason to decouple the Q-Switched laser clock to the rest of the experimental apparatus. The project and development of the asynchronous decoupling device to synchronize the laser with the rest of the apparatus will be discussed in Chapter 6.

5.3.4 Pulse-shape measurement

Measurements of the cavity pulse shape were obtained placing a fast photodiode close to the cavity output coupler. The photodiode is connected to an $1GHz$ oscilloscope together with the external laser triggering signal that toggles the Pockels cell inside the cavity. The triggering signal is generated by the synchronization device (described in Chapter 6) that exhibits very low jitter between the falling edge of the triggering signal and the rising edge of the detected photodiode signal (further details on the time fluctuation of the signals are given in Chapter 6, together with a detailed discussion about operating the EKSPLA laser with an external triggering signal). The detected signal was digitalized by the oscilloscope and fitted with the theoretical model developed in Chapter 3 (see for schematic).

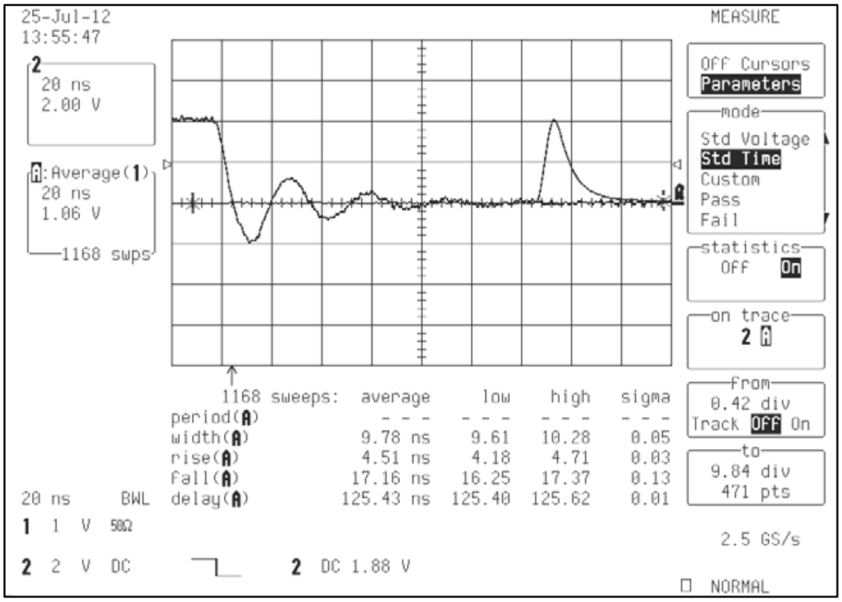

```
1168 sweeps:   average      low     high    sigma
period(A)       - - -       - - -   - - -   - - -
width(A)        9.78 ns     9.61    10.28   0.05
rise(A)         4.51 ns     4.18    4.71    0.03
fall(A)        17.16 ns    16.25    17.37   0.13
delay(A)      125.43 ns   125.40   125.62   0.01
```

Figure 5-4: Laser pulse shape as detected by the oscilloscope. The 125 ns delay time between the trigger (signal on the left) and the pulse (signal on the right) is introduced by the laser power supply and the photodiode cable.

Introducing A as a vertical offset (expected to be null, since it is not predicted by the model), B as an arbitrary scale factor (which depends on the photodiode intensity-to-voltage conversion function) and $C = B_0 V R \tau$, the fitting model is then

$$y = A + B\exp\left(\frac{1}{\left(C \cdot \tau_c\right)^2} - \frac{t - t_0}{\tau_c}\right)\left[1 + erf\left(\frac{C}{2}\left(t - t_0\right) - \frac{1}{C \cdot \tau_c}\right)\right] \tag{5.2}$$

The results of the fitting procedure applied to the data collected in the acquisition shown in Figure 5-4 (averaging 1168 pulses) are collected in Table 4 and Figure 5-5. As expected, the constant offset parameter is compatible with zero, with the obvious meaning that the parameter could be excluded from the fit. The fit correlation parameter R^2 is very close to unity, proving the validity of the theoretical model proposed to analyze the laser pulse shapes in the Q-Switched regime with intense external pump. The absolute value for the delay time t_0 has no significant meaning in this case, because it's affected by the systematic error of the placement of the photodiode on the table and the length of its cable. An accurate measurement of the delay time introduced by the laser power supply was performed using the synchronization device described in Chapter 7 as a pulse generator.

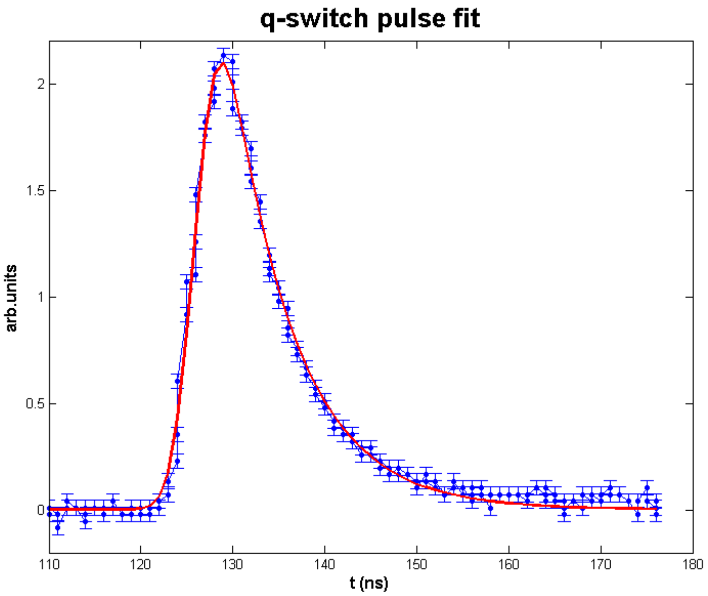

Figure 5-5: Laser pulse shape (blue points) and fit with the theoretical model developed in Chapter 3 (red line). The error on the vertical direction has been estimated measuring the fluctuation of the ground level when the photodiode is not excited by the laser radiation.

Fit parameter	Value
A	0.0033 ± 0.0019
B	1.737 ± 0.019
C	0.701 ± 0.013
τ_c	$7.013 \pm 0.098\ ns$
t_0	$126.165 \pm 0.033\ ns$
R^2	0.989

Table 4: Parameters obtained fitting the laser pulse shape with the theoretical model.

5.3.5 Effective reflectivity of the output coupler

The effective reflectivity of the output coupler, i.e. the fraction of cavity section surface that reflects back the light inside the unstable cavity, can be estimated from the resulting value of τ_c assuming that the undesired losses of the cavity are negligible. This approximation holds in this context because the number of pulse round trips inside the cavity is very low.

A $4\,ns$ pulse is just $120\ cm$ long, which means that in a $50\,cm$ cavity the active medium is depleted after only $1 \div 2$ round trips. Since

$$\frac{1}{\tau_c} = \nu_{FSR}\gamma_1 \tag{5.3}$$

and

$$\gamma_1 = -\log\left(1 - T\right) \tag{5.4}$$

(see [Svelto 2010]), it is possible to obtain an expression for T_{eff} and R_{eff}, the effective transmission and reflection factors of the output coupler, as a function of known parameters.

$$\begin{aligned} R_{eff} &= \exp\left(-\frac{1}{\tau_c \nu_{FSR}}\right) \\ T_{eff} &= 1 - R_{eff} \end{aligned} \tag{5.5}$$

Substituting the fit results yields the effective reflectivity and transmittivity of the output coupler.

$$\begin{aligned} R_{eff} &= 62.2 \pm 1.1\ \% \\ T_{eff} &= 37.8 \pm 1.1\ \% \end{aligned} \tag{5.6}$$

5.3.6 Infrared pulse energy

The energy of the IR pulse outputted by the laser is directly proportional to the pulse power at the end of the cavity. Measuring the IR energy as a function of the pump power allows determining the cavity threshold below which the population inversion is not enough to produce a laser pulse. The pump power can be varied acting on the power supply voltage regulator. The energy was measured with a laser power meter, specifically designed to measure the energy of high-energy Q-Switched lasers, placed in front of the 1064 output window outside the laser apparatus. The resulting data were fitted with a linear model, as shown in Figure 5-6.

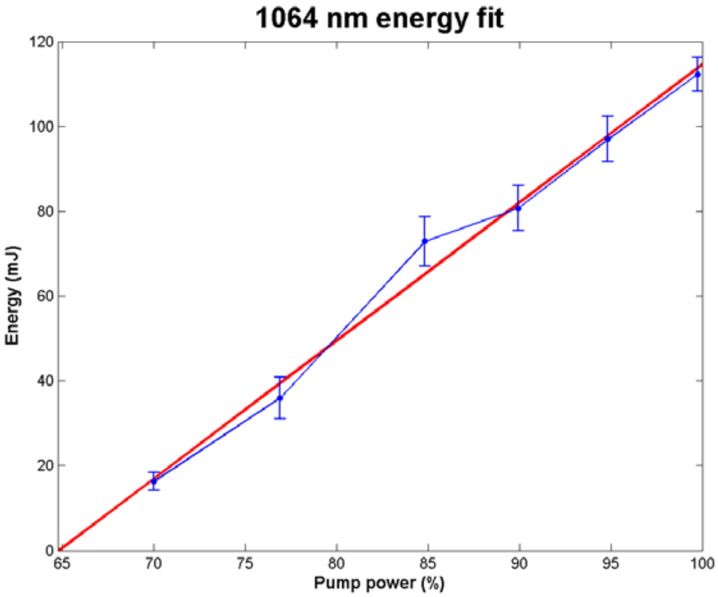

Parameter	Value
Fit model	$y = A + Bx$
A	-211 ± 17
B	3.26 ± 0.20
R^2	0.989
Threshold	$64.8 \pm 6.6\ \%$

Figure 5-6: Energy of the 1064 nm pulse as a function of pump power (blue) and its linear fit (red), extrapolated up to the pump threshold corresponding to 65%. Errors in the horizontal direction are negligible.

The relation is found linear as expected. The linear fit is an useful tool to convert the pump power set on the power supply to a reference energy outputted by the pump cavity.

5.3.7 Second harmonic generation

The second harmonic pulse is generated by a KTP non-linear crystal correctly phase-matched to convert two 1064 nm input photons into one 532 nm output photon. The conversion is non-linear: the intensity of the output pulse depends quadratically on the input intensity. The relation between the IR pulse energy and the green pulse energy is expected to be found quadratic.

The energy of second harmonic pulses was measured as a function of the pump power with the energy meter placed outside the 532 nm output window. Using the linear relation found in the last paragraph, it was possible to convert the pump power in terms of 1064 nm pulse energy: this step is mandatory to properly consider the laser cavity threshold. Fitting the 532 pulse energy with respect to 1064 pulse energy with a power law gives the results shown in Figure 5-7.

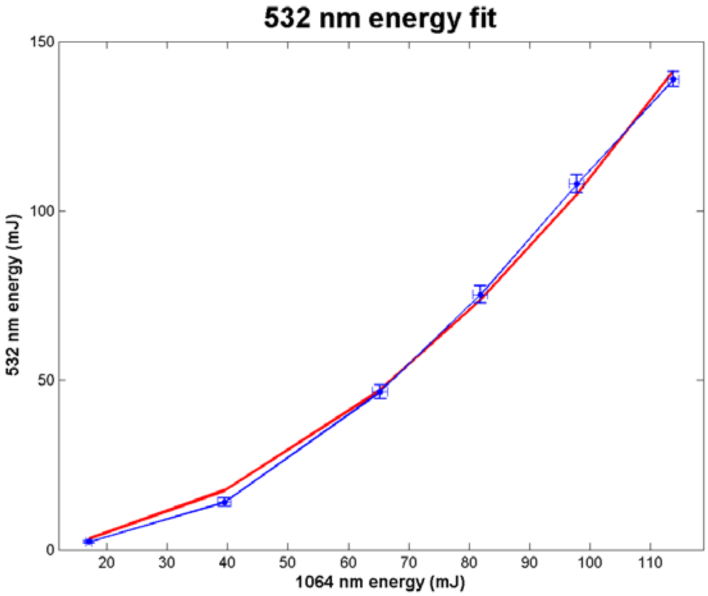

Parameter	Value
Fit model	$y = A \cdot x^B$
A	$\left(12.6 \pm 5.2\right) \cdot 10^{-3}$
B	1.970 ± 0.090
R^2	0.9978

Figure 5-7: Energy of the 532 nm pulse as a function of the 1064 nm pulse energy (blue) and its power-law fit (red).

Although the found exponent matches the expected parabolic behavior up to 0.3σ, this result is unexpected. The pulse duration changes significantly from the maximum power configuration, with pump power close to 100%, to the lowest energy configuration, with pump power around 70%: if the pulse is $\sim 4\,ns$ long at 99%, at 70% it increases to more than $6\,ns$. Clearly, the pulse duration affects the peak power since the energy of the packet is distributed in a longer shape. The non-linear crystal amplification effect depends on the square of the pulse amplitude, thus the generation of $532\,nm$ is expected to be perturbed by this effect.

Results showed that for $532\,nm$ the change in pulse duration doesn't affect significantly the second harmonic generation.

5.3.8 Fourth harmonic generation

Similarly to the second harmonic, the fourth harmonic is generated by a KTP crystal phase-matched to convert two 532 nm input photons into one 266 nm output photon. The intensity of the output UV pulse is expected to be quadratically dependent by the energy of the input green pulse, thus making the intensity of the UV pulse quartically dependent by the energy of the IR pulse.

The energy of the fourth harmonic was measured with the energy meter outside the 266 nm output window. Fitting the measured 266 nm pulse energy with respect to the 532 nm pulse energy gives the results shown in Figure 5-8.

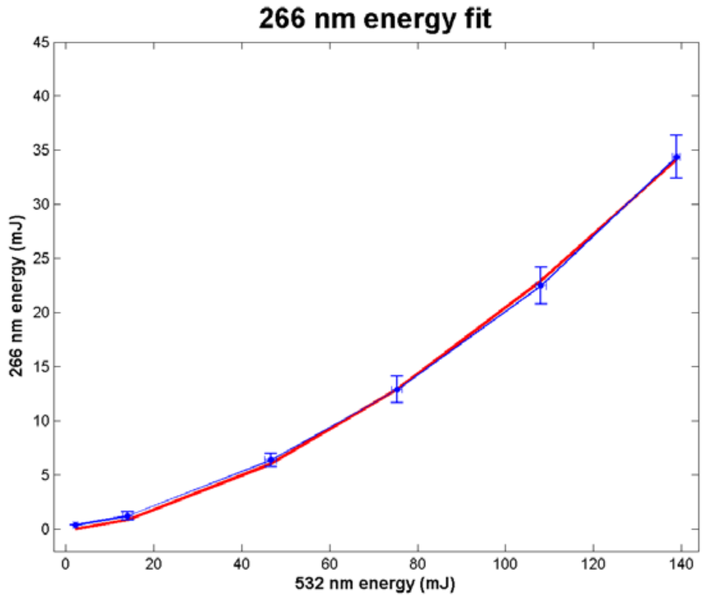

Parameter	**Value**
Fit model	$y = A \cdot x^B$
A	$\left(13.8 \pm 2.9\right) \cdot 10^{-3}$
B	1.584 ± 0.044
R^2	0.99930

Figure 5-8: Energy of the 266 nm pulse as a function of the 532 nm pulse energy (blue) and its power-law fit (red).

Differently from the 532 energy case, here the found exponent is different from the expected value of 2: the two values are not compatible by 9.5σ. In this case, the change of the pulse duration affects significantly the generation. This can be expected, since the fourth harmonic generation depends on the fourth power of the initial $1064\,nm$ amplitude.

In Figure 5-9 a summary of the results obtained in the last paragraphs is shown, concluding the description of the characteristics of the pump laser apparatus.

5.3.9 Flash lamp degradation

The pump flash lamp degrades during the operation at high pump regimes, progressively loosing performance. For reference, a six months old flash lamp operating on average two hours per working day showed a decrease in pump performance about 10%, which become a very significant fraction for the higher harmonics, especially the UV.

For this reason, the pump power was kept at 88% for most of the time. In the following paragraphs, the energy references are given with a pump power of 93%, closer to the AEGIS operation value.

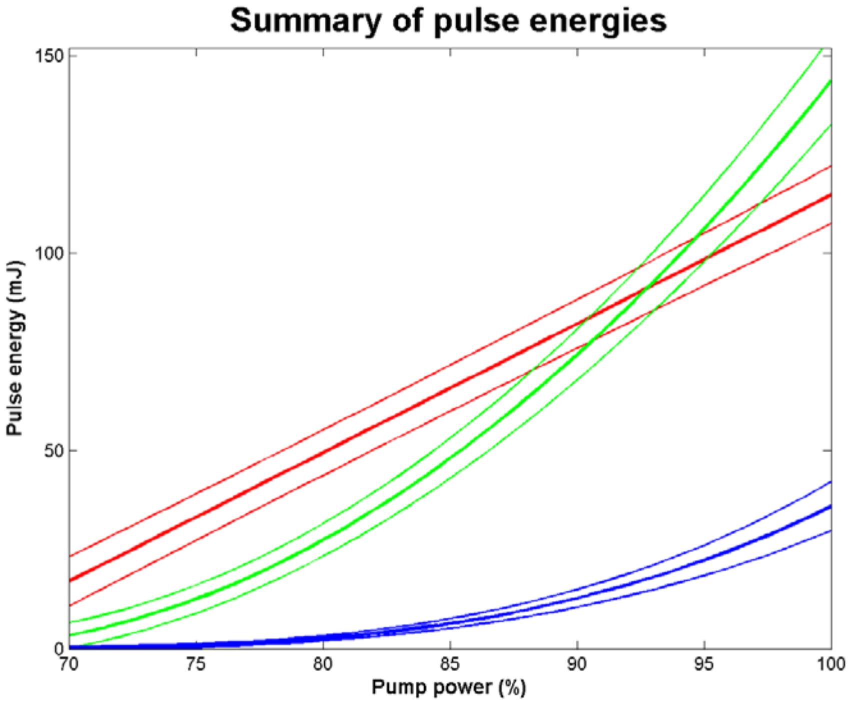

Figure 5-9: Summary of the results obtained by fitting the pulse energies: 1064 nm (red), 532 nm (green) and 266 nm (blue). The energies are shown as a function of the pump power. Above and below each curve two curves expressing the standard deviations of the sample are plotted, corresponding to a confidence level of 68% (one sigma below and one sigma above).

5.3.10 External trigger operation

The laser apparatus can operate either with an internal clock up to 10 Hz fed by the power supply controller or with an external clock fed via a TTL (5 V, 50 ohm terminated) BNC cable. In external clock modality the power supply waits with the capacitor pack charged and ready, until a square-wave trigger signal is received. At the moment of receiving an impulse, the flash lamp is activated while the cavity losses are kept at a high level. The Pockels cell is then switched, reducing the cavity losses and allowing the q-switch pulse formation, after a delay corresponding to the trigger impulse length. In other words, the rising edge of the trigger signal turns on the flash lamp, while the falling edge switches the Pockels cell (see Figure 5-10).

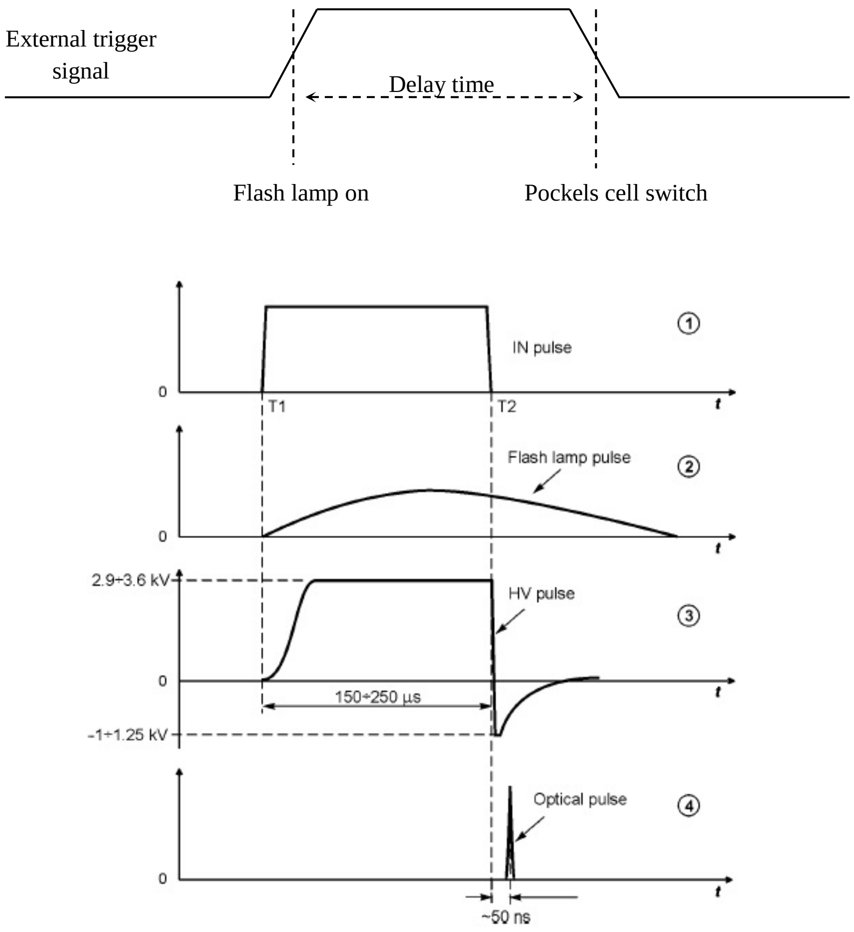

Figure 5-10: Time scheme of the external trigger signal (above) and laser time specifications as reported on the EKSPLA laser operating manual (below).

The output laser power is adjusted varying the trigger pulse duration. The longer the delay, the more the population inversion is discharged by spontaneous emission. Resulting energies as a function of the trigger signal length are reported in Figure 5-11.

In normal operation conditions, the durations to obtain maximum power, adjustment power and no power at all (with the flash lamp still working to discharge the capacitor pack) are:

$$t_{\max} = 220\,\mu s \quad t_{adj} = 400\,\mu s \quad t_{off} = 1000\,\mu s \tag{5.7}$$

Moreover, the laser pulse peak is expected after $t_{pulse} \sim 50\,ns$ from the falling edge of the trigger signal.

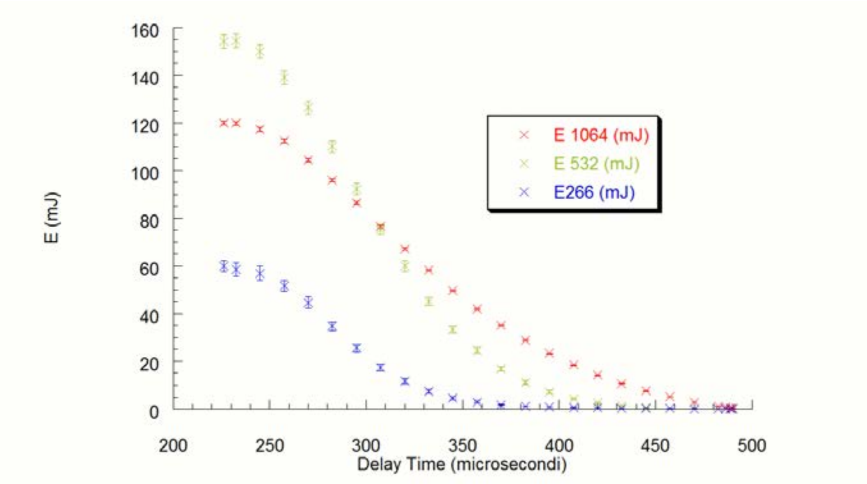

Figure 5-11: Laser energies as a function of the delay time between the flash lamp shot and the Pockels cell switch. Courtesy of [Ferri 2011].

5.4 The ultraviolet beam line

The second macro-component of the laser apparatus is the breadboard containing the components associated to the production of $205\ nm$ UV radiation (see Figure 5-12 for reference). Three different stages can be distinguished:

1. Optical parametric generation of $894\,nm$ radiation from a $532\,nm$ pulse inside a periodically-poled KTP crystal;
2. Optical parametric amplification of the $894\,nm$ seeding pulse using an intense $532\,nm$ pump pulse inside two barium-borate (BBO) crystals;
3. Frequency sum of the resulting $894\,nm$ pulse with the $266\,nm$ pulse inside a BBO crystal, to obtain the required $205\,nm$ pulse.

5.4.1 Optical parametric generation

The generation of the $894\,nm$ pulse happens inside a periodically poled $KTiPO_4$ crystal (usually called PPKTP). The leading effect is the down-conversion of an input photon at $532\,nm$ into two output photons: a signal photon at $894\,nm$ and an idler photon at $1313\,nm$

$$\left(532\,nm\right)_{ord} \xrightarrow{\quad} \left(894\,nm\right)_{ord} + \left(1313\,nm\right)_{ord} \tag{5.8}$$

In order the correct wavelengths to be produced, the crystal has to be kept at high temperature to adapt its refractive index. The temperature is kept at a constant level by a digital temperature controller. A spectrometric survey of the produced beam showed that the correct crystal temperature to produce $894\,nm$ is

$$T = 152.6\,°C \tag{5.9}$$

Since the crystal itself is almost perfectly transparent for all the involved frequencies, all the power of the incoming pulse is equally divided on the outputs. The power ratios are the following:

$$\frac{E_{894}}{E_{532}} = \frac{532}{894} = 0.595 \quad \frac{E_{1313}}{E_{532}} = \frac{532}{1313} = 0.495 \tag{5.10}$$

The crystal introduces a beam divergence that needs to be corrected after the generation with a collimating lens to properly fit in size inside the OPA crystals. The $1313\,nm$ idler signal is removed before entering in the OPA by the dichroic beam splitter, which performs three operations: transmits the $894\,nm$ signal beam without reflecting it backwards or at 90°, reflects backwards the $1313\,nm$ idler beam and reflects by 90° the $532\,nm$ pump beam.

The generation crystal has a low damage threshold, hence the amplification step. The maximum acceptable $532\,nm$ power that can be shined on the PPKTP without damaging it is $E_{\max} = 1.5\,mJ$.

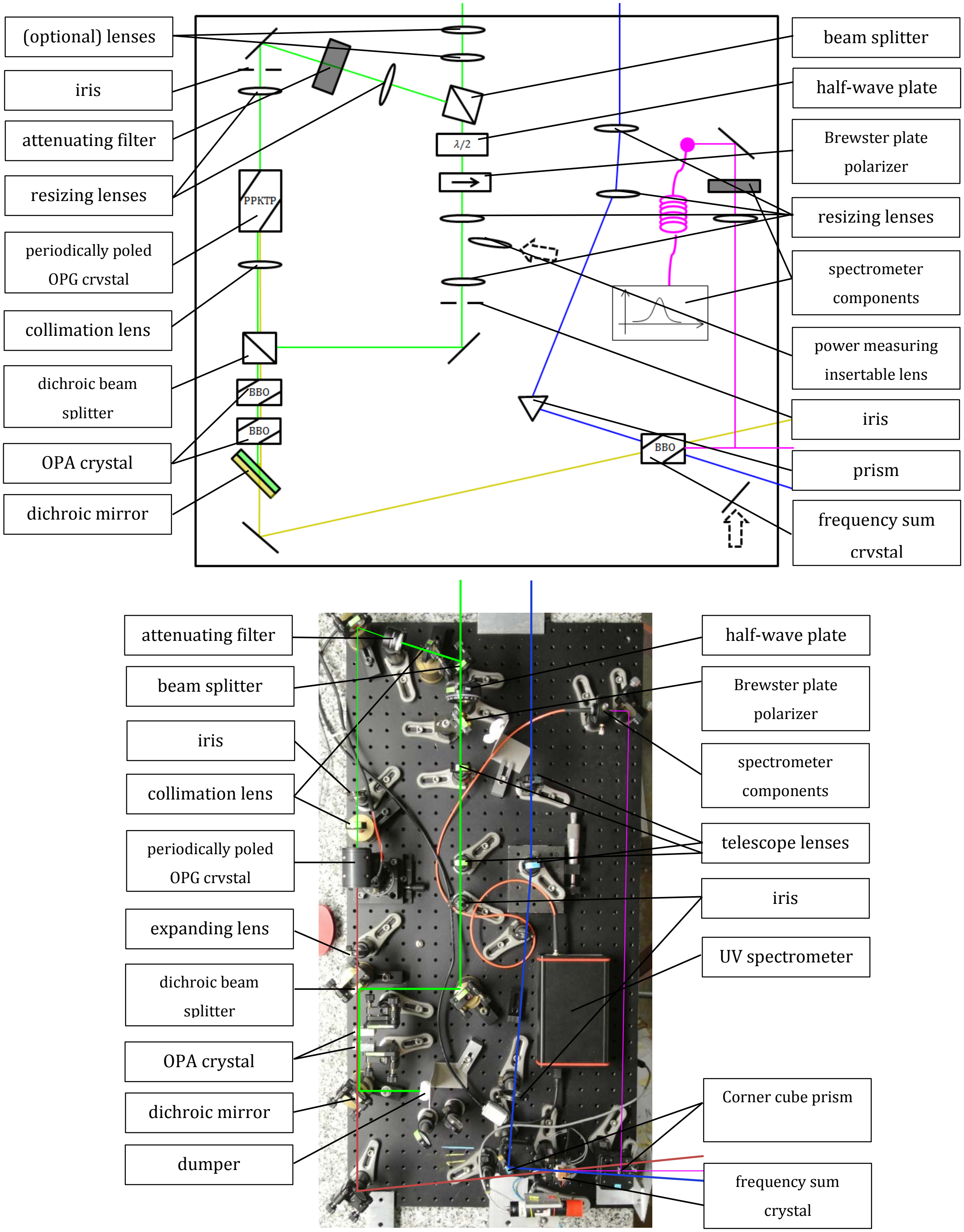

Figure 5-12: Complete schematics and photograph after the commissioning at CERN of the UV breadboard to produce 205 nm radiation.

5.4.2 Optical parametric amplification

The amplification step is performed by two barium borate crystals that make use of the parametric down-conversion effect to amplify the $894\,nm$ seed beam generated in the PPKTP. This step is necessary to have enough power to perform the frequency sum. As for the OPG, the conversion process is

$$\left(532\,nm\right)_{ex\,\mathrm{tr}} \longrightarrow \left(894\,nm\right)_{ord} + \left(1313\,nm\right)_{ord} \tag{5.11}$$

Both crystals need to be rotated at a precise angle with respect to the beam axis to achieve the required type-1 phase-matching: 22.6°. This value depends on the main crystallographic axis direction. Phase-matching the OPA crystals is a delicate task that requires good manual skills; a misalignment in the order of fractions of degree results in a complete loss of the amplification effect.

The BBO crystals have an higher damage threshold with respect to the PPKPT ($500MW\ /\ cm^2$ instead of $200MW\ /\ cm^2$), thus allowing an intense $532\,nm$ pump beam to be used. The maximum acceptable energy with a $2.4\,mm$ pump beam is

$$E_{pump} = 65\,mJ \tag{5.12}$$

In normal operating conditions, a typical value of the pulse energy amplified by the first crystal alone, after optimizing the phase-matching, is

$$E_1 = 7\,mJ \tag{5.13}$$

Introducing the second crystal raises the power up to

$$E_2 = 15\,mJ \tag{5.14}$$

With 93% pump power, a maximum of $18mJ$ of $894\,nm + 1313\,nm$ have been obtained during the test at CERN. The leftover $532\,nm$ pump beam is removed from the beam line after the OPA by a dichroic mirror that reflects it on a plastic dumper.

5.4.3 Frequency sum

The frequency sum is performed inside a BBO crystal stabilized in temperature at 40 °C to reduce the opacization due to ambient moist absorption (BBO is highly hygroscopic). The conversion process is the following:

$$\left(894\,nm\right)_{ord}+\left(266\,nm\right)_{ord}\xrightarrow{\qquad}\left(205\,nm\right)_{ex\,\mathrm{tr}} \tag{5.15}$$

The $894\,nm$ is sent directly on the crystal after the OPA without removing the $1313\,nm$ idler, because the peak power is much lower than the damage threshold. The $266\,nm$ comes directly from the laser after a size adjustment and is reflected by a corner cube prism in the required direction. The maximum acceptable power of $266\,nm$ radiation, with a beam size of $2.4\,mm$ in radius, is

$$E_{UV}=27\,mJ \tag{5.16}$$

Since the pump laser can produce more UV power than the damage ratio, a careful adjustment of the pump power need to be done.

The two beams must enter in the sum crystal with different angles with respect to the crystal face normal to obtain the correct phase matching. The correct alignment angles can be easily calculated imposing the impulse conservation of the involved photons (see Figure 5-13).

$$\begin{aligned}\vartheta_{894}&=6.5^\circ\\ \vartheta_{266}&=1.8^\circ\end{aligned} \tag{5.17}$$

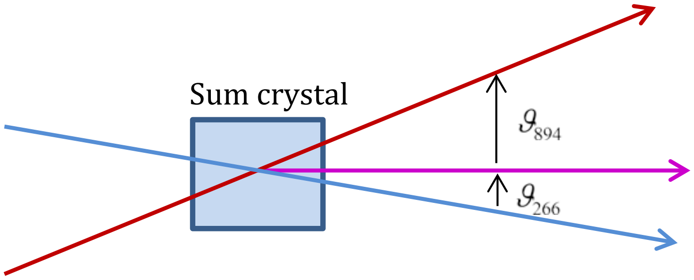

Figure 5-13: Geometrical scheme of the beams inside the frequency sum crystal.

The phase-matching angle to produce $205\,nm$ is $\vartheta_{pm} = 59.6°$. Tiny adjustments of the produced wavelength can be obtained rotating the crystal to a slightly different phase-matching angle (fractions of degree). A diagnostic UV spectrometer was installed to collect the produced pulse and properly align the crystal to produce $205.035\,nm$.

Measuring the produced $205\,nm$ energy as a function of the laser parameters is quite inappropriate, tough, because the produced energy depends significantly by the crystal surface conditions and the laser flash lamp conditions. The produced $205\,nm$ beam can reach energies in the order of $300\,\mu J$ with a brand new sum crystal and $25\,mJ$ of $266\,nm$. A more conservative (but realistic) estimate of the power that can be achieved optimizing the laser parameters with a slightly degraded crystal is in the order of $150\,\mu J$.

5.4.4 Degradation of the sum crystal

Although the overall power of the incoming beams fulfills the maximum threshold requirements, a degradation of the crystal surface was observed during the thesis work. After three months 2 hours a day on average of operation at maximum power, the crystal was found damaged over almost 50% of the usable surface (see Figure 5-14). This behavior is not critical for AEGIS operation, since the laser apparatus shines a full power pulse only once per 300 s on average (depending on the Positronium apparatus). However, during diagnostic operation a low level of 266 energy should be kept in order to preserve the crystal. An effective way to selectively reduce the $266\,nm$ power is to rotate the quarter-wave plate inside the laser close to the UV output window to dump a fraction of the outgoing beam.

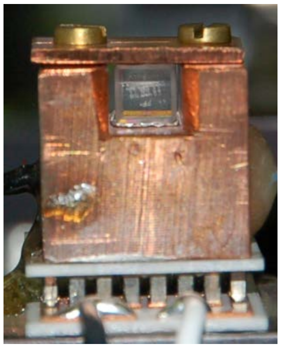

Figure 5-14: Photograph of a severely degraded BBO crystal installed inside the thermalizing copper box. The active thermal element is t small Peltier cell placed below the copper element.

5.5 The infrared beam line

The third macro-component of the laser apparatus is the breadboard containing the components associated to the production of $1650 \div 1700 \ nm$ IR radiation (see Figure 5-16 for reference). The scheme of the pulse production is analogous to the one exploited to produce $894\,nm$ on the ultraviolet breadboard. Two different stages can be distinguished:

1. Optical parametric generation of $1650 \div 1700\,nm$ radiation from a $1064\,nm$ pulse inside a periodically-poled KTP crystal;
2. Optical parametric amplification of the $1650 \div 1700\,nm$ seeding pulse using an intense $1064\,nm$ pump pulse inside two KTP crystals;

5.5.1 Optical parametric generation

The optical parametric generation scheme of $1650 \div 1700\,nm$ pulses is similar to the one used for producing the $894\,nm$ radiation on the UV breadboard. Here the leading effect is the down-conversion of an input photon at $1064\,nm$ into two output photons: a signal photon in the required wavelength range $1650 \div 1700\,nm$ and an idler photon within the range $2996 \div 2844\,nm$. The process is the following.

$$\left(1064\,nm\right)_{ord} \longrightarrow \left(1650 \div 1700\,nm\right)_{ord} + \left(2996 \div 2884\right)_{ord} \tag{5.18}$$

The resulting wavelength can be modified altering the temperature of the PPKTP crystal, thus changing its refractive index. The temperature is kept at a constant level by a digital temperature controller. A spectroscopic survey of the produced wavelengths as a function of the crystal temperature was carried out generating the second harmonic via a $LiNb$ crystal on the beam path. Results are shown in Figure 5-15.

As in the case of ultraviolet, the pulse energy entering in the PPKTP must be no more than $1.5\,mJ$ to preserve the crystal. A typical value for 93% pump power is $E_{93\%} = 1.463 \pm 0.024\,mJ$.

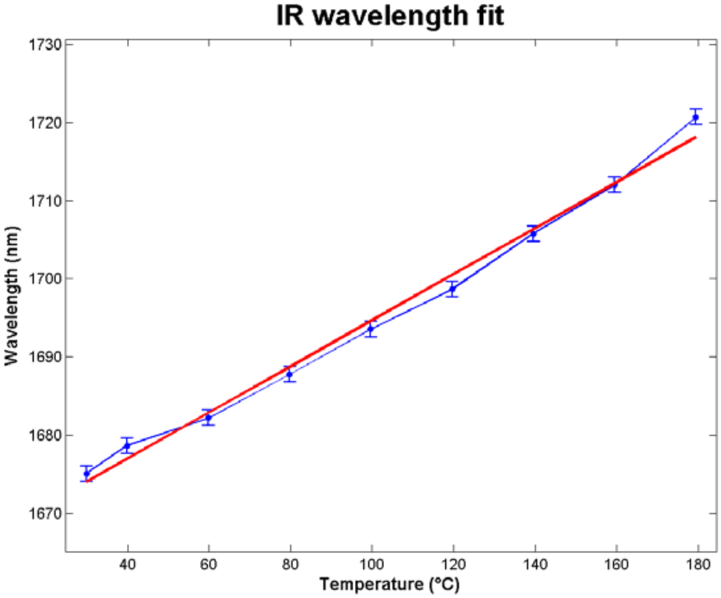

Parameter	**Value**
Fit model	$y = A + Bx$
A	1665.2 ± 1.2
B	0.295 ± 0.011
R^2	0.9915

Figure 5-15: Produced IR wavelength as a function of the PPKTP crystal.

5.5.2 Optical parametric amplification

The optical parametric amplification of the OPG pulse is performed by two KTP crystals pumped with an intense pulse of $1064\,nm$ from the laser. The process involved in the amplification is similar to the OPG, excepting for the extraordinary idler beam and the type-2 phase-matching of the OPA crystals.

$$\left(1064\,nm\right)_{ord} \longrightarrow \left(1650 \div 1700\,nm\right)_{ord} + \left(2996 \div 2884\right)_{ex\,\mathrm{tr}} \tag{5.19}$$

Differently from the BBO crystals operating in the OPA of the ultraviolet breadboard, KTPs have a much higher critical intensity: $2.4\,GW / cm^2$ instead of $500MW / cm^2$. The maximum energy that can be fed in the OPA is

$$E_{\max} = 93\,mJ \tag{5.20}$$

The amplification of only the first crystal (correctly phase-matched) produces a pulse of

$$E_1 = 0.980\,mJ \tag{5.21}$$

After the second crystal, the energy reaches

$$E_2 = 4.5\,mJ \tag{5.22}$$

much above $200\,\mu J$ needed to saturate the transition $3 \to n$. In normal working conditions, an energy of $1\,mJ$ should be obtained.

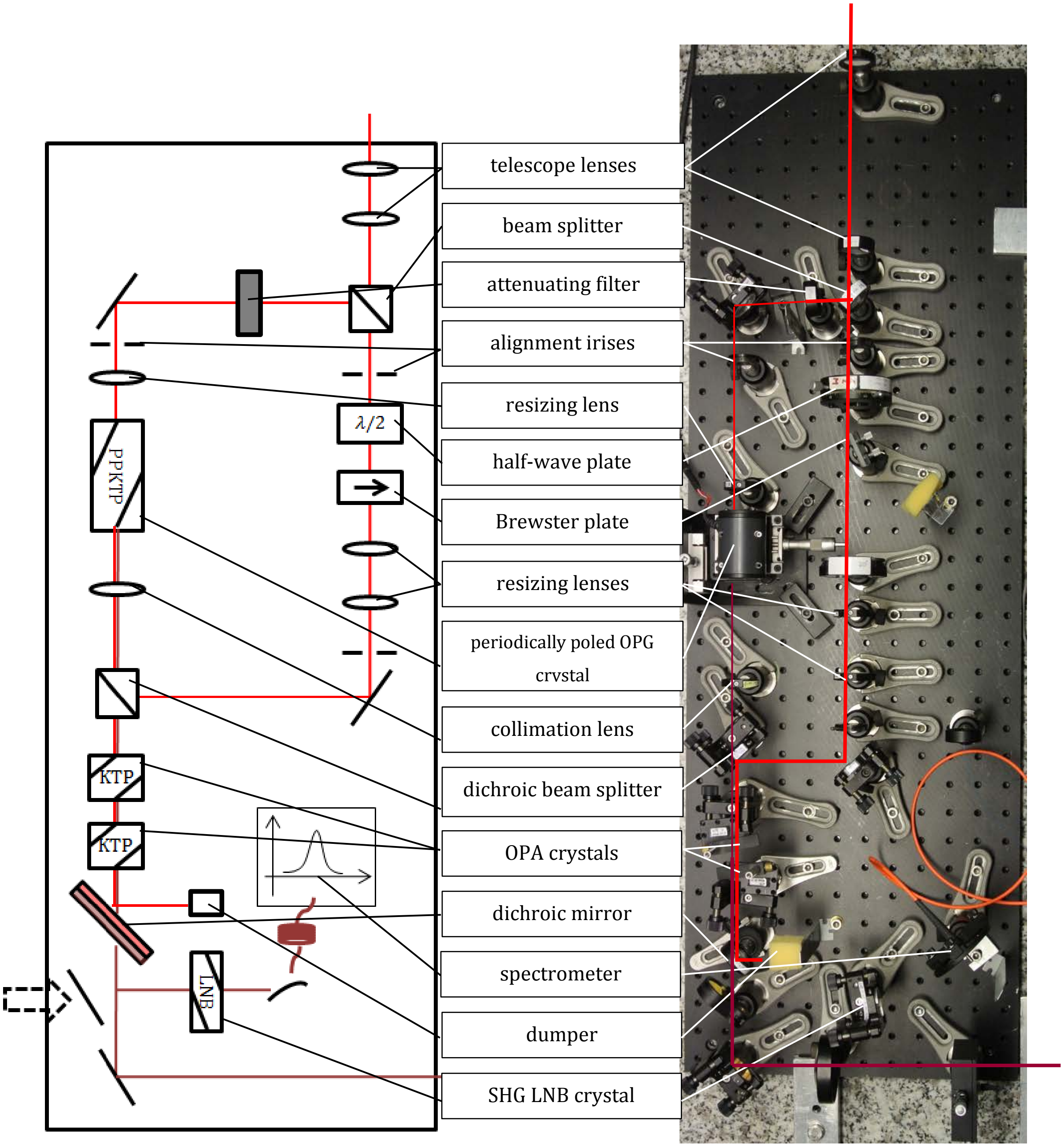

Figure 5-16: Complete schematics and photograph, after the commissioning at CERN, of the IR breadboard to produce 1650-1700 nm radiation.

6 Designing the transfer line to the experimental apparatus

6.1 The laser transfer line to the Positronium experiment

The laser pulses are produced by the laser apparatus in different locations over the optics table, and need to be collected together and carried to the experimental region where the Positronium converter will be placed. In the final organization of the experimental area, the Positronium converter is positioned several meters away from the laser breadboards and at a significantly different height.

A custom optical transfer line was designed, commissioned and tested during this thesis work. The testing of the line, in particular, was first done in the Milano laboratory and later in the experimental area at CERN where the transfer line was installed during February, 2013.

6.2 Design of the transfer line

6.2.1 Structure of the Positronium chamber

The starting point of the transfer line project is the structure of the Positronium experiment chamber. Two UV fused silica windows are intended for laser usage on the two opposite sides of the chamber (see Figure 2-15 and Figure 2-16). Laser beams shine from one side, enter the chamber from one of the windows, travel through the vacuum region hitting the Positronium, leave the camber from the opposite window and are reflected on a final mirror to travel the way back and double the excitation efficiency. The scheme of the beams in the chamber is shown in Figure 6-1.

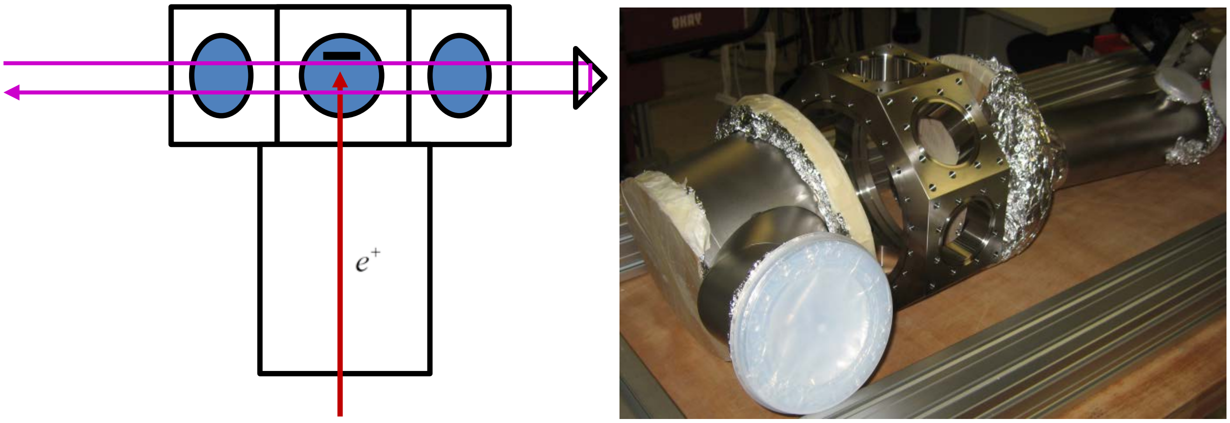

Figure 6-1: Left, structure of the Positronium experiment chamber with the positron beam (red) and the laser beam (violet). Right, a photograph of the current chamber assembly in the Trento laboratory is shown.

6.2.2 Requirements

Besides those imposed by the structure of the Positronium chamber, the laser transfer line must fulfill some other important constraints:

1. Correctly superimpose infrared and ultraviolet beams on the target region;
2. Transmit as much energy as possible for both infrared and ultraviolet wavelengths;
3. Adjust the spatial dimensions to have two circular Gaussian beams;
4. Reduce as much as possible the beams divergence;
5. Guarantee that both pulses shine contemporaneously on the Positronium without delays.

Moreover, it would be particularly comfortable to share at least the last components of the transfer line for both the radiations. In this way the alignment of the beams on the target region is made much easier, since it would be possible to choose freely the direction of the beams with the last mirrors without affecting their relative alignment.

6.2.3 Scheme of the transfer line

In order to discuss the details of all choices made to design the transfer line, it is useful to anticipate its final form with a synthetic scheme. The elements that compose the transfer line are the following (see Figure 6-2):

1. A first UV fused silica corner cube picks the ultraviolet $205\,nm$ radiation and reflects it by 90°;
2. A second UV fused silica corner cube rotates the beam in the vertical direction to send the radiation to the first mirror of the transport line;
3. Simultaneously, the infrared $1650 \div 1700\,nm$ beam is adjusted in size and divergence on the horizontal axis by a telescopic system made of cylindrical lenses;
4. The infrared beam is then reflected up by a gold plated mirror to a NBK-7 corner cube;
5. The corner cube rotates the infrared beam to send it to the first mirror of the transport line;
6. Now, both the beams are reflected by the same high-reflectivity ultra wideband aluminum mirror from the vertical direction to the horizontal direction, travelling in the air all the way to a second aluminum mirror;
7. The second mirror reflects both radiations in the direction of the Positronium experimental region and the final corner cube beyond the chamber.

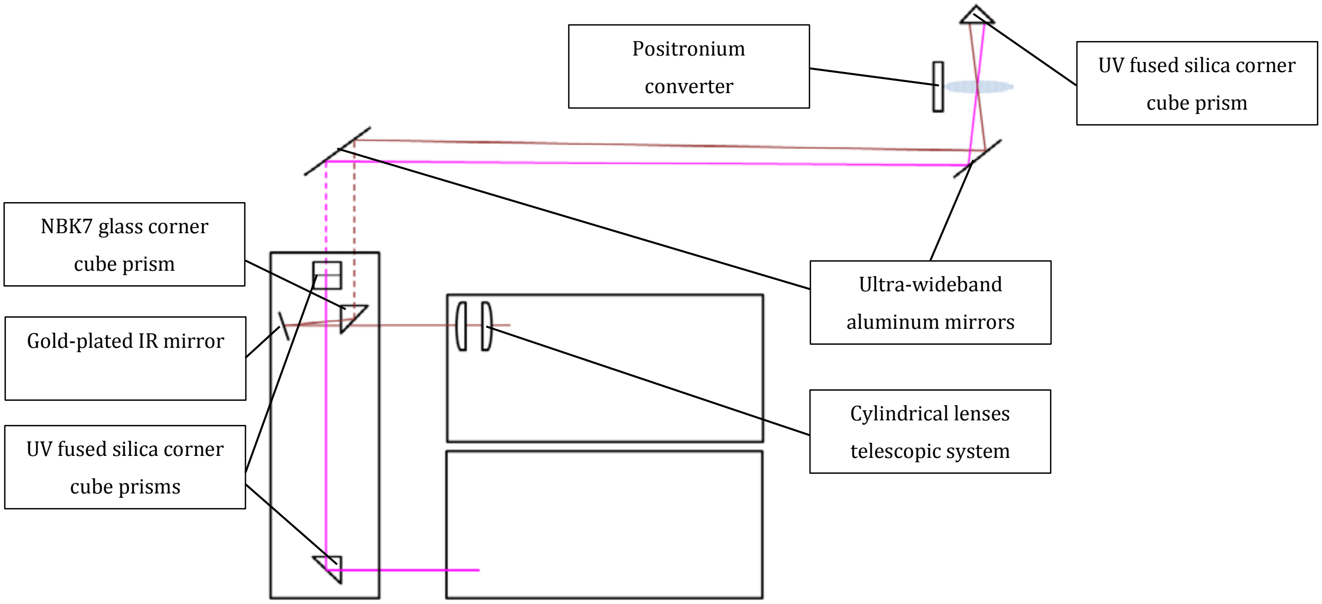

Figure 6-2: Schematics of the transfer line project. The violet line represents the ultraviolet beam, while the brown line the infrared beam. The dashed lines represent vertical rays.

The requirements described in the above list were addressed one by one as described in the following paragraphs.

6.2.4 Superimposing the beams

The pulse superimposition on the target area is a matter of fine relative alignment of the beams. Two different alignment components are needed on the table to adjust their relative direction. This is mandatory to share the same optical components for both wavelengths on the long arms of the transfer line. The relative direction adjustment is carried out by two corner cubes (one for UV and one for IR) at different heights, very close one to each other on the horizontal plane. Each corner cube takes care of addressing its beam to the first mirror of the transfer line with the correct angle so that they intersect in front of the Positronium converter.

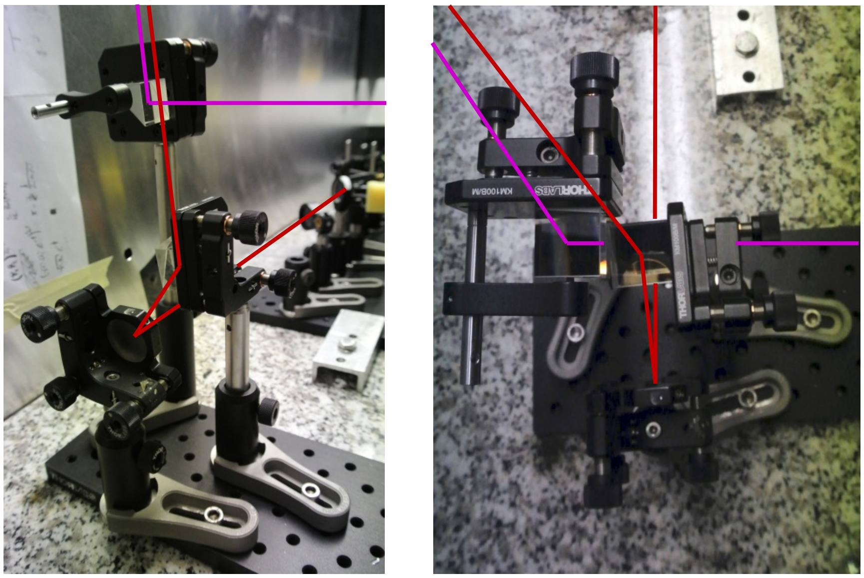

Figure 6-3: The corner cube assembly to align the beams on the first mirror of the transfer line. On the right, the top view showing the vicinity of the two prisms on the horizontal plane; on the left, a lateral view of the assembly. The beams are drawn with the usual color convention.

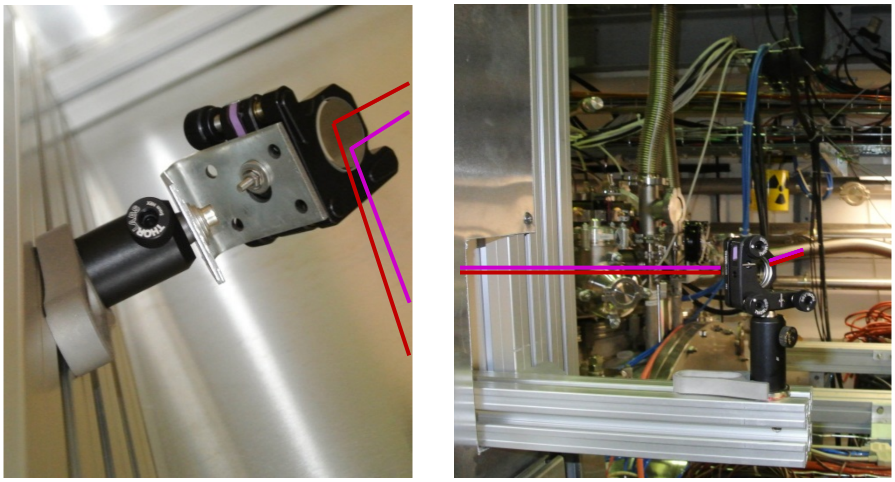

Figure 6-4: On the left, the first aluminum ultra-wideband mirror to reflect both ultraviolet and infrared beams. On the right, the second aluminum mirror that sends the beams in their final directions (chamber not yet in position in the photograph)

6.2.5 Transport efficiency

A high transport efficiency is important on the ultraviolet line, where at the most $200\,\mu J$ of energy can be obtained at the price of quick deterioration of the frequency sum crystal. The infrared line, on the other hand, is not critical since the produced energy is one order of magnitude above the saturation fluency.

Firstly, the fraction of energy lost by the transport line was minimized reducing as much as possible the number of optical elements. Since both spatial quality and divergence of the ultraviolet radiation were found satisfactory, no further lenses were introduced.

Secondly, dedicated optical components where chosen in every part to minimize losses. The most critical components are the transfer line mirrors which must have high reflectivity both in the deep UV region and in the far IR region. Two DUVA-graded aluminum-plated ultra-wideband mirrors from CVI-Melles Griot were chosen, which offer 95% reflectivity in the deep UV region and 90% reflectivity in the IR region. All three reflection corner cubes after the frequency sum crystal are uncoated UV fused silica prisms with a transmittivity of 90%.

With such transmittivities, an overall energy loss of 43% is expected after the transfer line and the fused silica window of the chamber (usually having 87% transmittivity). Adding two UV fused silica lenses to the transfer line would increase the losses to 54%. Substituting all corner cubes with aluminum mirrors, leaving the lenses in place, reduces the losses back to 45%.

This factor 2 reduction in energy caused by the losses compensates the factor-2 increase in excitation efficiency due to the last corner cube that reflects back the ultraviolet beam.

For reference, on the infrared line, both lenses and prism were chosen of NBK-7 glass with anti-reflection coating suitable for operation in the $1650 \div 1750\,nm$ range (coating C); the mirror is gold-plated, with a reflectivity above 95%.

6.2.6 Spatial adjustment of the infrared pulse

The infrared beam leaves the OPA stage on the breadboard slightly divergent in the horizontal direction. The measured beam size close to the OPA crystals is about $3\,mm$ in radius. After $124\,cm$ of travel in free-air the beam size grows to $10\,mm$, thus having a divergence of

$$\vartheta_{div} = 0.16^\circ \tag{6.1}$$

Two cylindrical lenses in telescopic configuration effectively remove the divergence, which needs to be compensated shortly after the OPA, before the beam becomes elliptical. For this reason the lenses were chosen with short and equal focal length to be placed at the end of the IR breadboard.

In the vertical direction, on the contrary, the beam doesn't require any adjustment.

6.2.7 Synchronization of pulses

A de-synchronization of the pulses may happen only before they leave the optical table, since both beams share a common path from the two last corner cubes. The extraction point of the beams (i.e., the position of the corner cubes) was chosen so that the optical path from the laser apertures to the extraction point is the same for both paths within an acceptable $30\,cm$ error, which corresponds to a delay time of $1\,ns$.

The delay time can be adjusted, if needed by the experiment, both delaying the IR pulse and delaying the UV pulse. The former is obtained moving the IR corner cube in the direction of the IR breadboard, which is the opposite direction to the gold-plated IR mirror. The latter, differently, is obtained adding two further mirrors to the transfer line, so that the pulse travels back and forth. This delay line with mirrors, actually, is already present on the table because it is needed by the antihydrogen experiment to compensate the delay introduced by the IR optical fiber. A complete scheme of the UV delay line can be found in [Cerchiari 2013].

It isn't expected, however, to introduce a delay on the UV line in the case of the spectroscopy experiment. The reason is that the beam line on the UV breadboard is already a bit longer than that of the IR breadboard.

6.3 Testing the transfer line

Aside from the geometrical characteristics of the beam, that are easily determined and corrected inserting a screen in any point of the transfer line, for the purposes of the experiment the most critical parameter to determine is the overall delay from the trigger signal to the arrival of the laser pulse in the experimental zone.

In order to excite a significant fraction of the thermalized Positronium emerging from the converter, the laser pulse must be synchronized very carefully to shine on the Positronium cloud at the right moment, when the cloud size is approximately as big as the pulse shape. The timing aspects of the Positronium production, as well as the way to achieve the correct synchronization, are described in detail in the following Chapter 7.

The overall delay time sums up the following sub-delays:

1. Cable delay from the pulse generator to the laser power supply;
2. Internal delay of the laser power supply from the trigger signal to the effective switch of the Pockels cell;
3. Time delay for the formation of the q-switch impulse inside the cavity;
4. Propagation delay from the laser to the end of UV and IR breadboards;
5. Transfer line time delay.

A complete discussion about delays is found in Chapter 7. The focus of the present section is the measurement of the transfer line time delay only and, consequently, the measurement of the transfer line length.

The transfer line delay time was measured in the following way. A fast photodiode (response time $< 0.1 ns$) is connected to a 500 MHz-class oscilloscope, together with the triggering signal fed to the laser power supply. A pulse generator provides the trigger both to the oscilloscope and the power supply (actually the signals were provided by the synchronization device described in the following chapter, acting as a pulse generator with the delay time set to 0). The photodiode is connected to the oscilloscope via a long coaxial cable (10 m in length) and is placed first in the Positronium chamber location, then (using the same cable) at the end of IR breadboard, close to the corner cubes.

Since all the configuration was left untouched, besides the position of the photodiode, the delay time difference isn't affected by systematic errors due to different cable lengths. The average result after 100 repeated acquisitions is

$$t_d = 16.59 \pm 0.30 \ ns \tag{6.2}$$

which corresponds to a length of

$$L_d = 497.8 \pm 9.0\ cm \tag{6.3}$$

At the end of the transfer line, the pulses are synchronized within the expected interval. Two different measurements were performed to estimate the relative delay time, first with IR only, then with UV only. It's more meaningful to report the measurements of the overall delay time from the trigger signal to the detection.

$$\begin{aligned} t_{IR} &= 147.2 \pm 0.3\, ns \\ t_{UV} &= 146.4 \pm 0.3\, ns \end{aligned} \tag{6.4}$$

7 Synchronizing the laser pulses with the Positronium accumulator

7.1 Timing of Positronium production

Experiments conducted by the Trento group during 2010 (see [Mariazzi 2010 PRL]) show that Positronium emerges from porous silica targets on average $\sim 20\,ns$ after positron implantation. The cloud is composed by two different populations: the first fraction thermalizes inside the converter, thus having low temperature, and shines isotropically from the pores; the second, on the other hand, has higher temperature and shines predominantly forward at an unknown aperture angle. As a reference, a silica target thermalized at $150\,K$ shines Positronium with Maxwellian velocity distributions centered around $145 \pm 10\,K$ and $1260 \pm 15\,K$. The cloud then progressively expands in all directions, since the faster Positronium moves ahead the thermalized Positronium.

This raises the question of when time is right to shoot the laser. A typical bunch of implanted positrons has a duration of $20\,ns$. If the delay between implantation and the shot is set too short, not all the Positronium will be released from the target. On the other hand, if the delay is too long, the cloud will become so wide that the laser beam cannot cover it all.

To obtain maximum excitation efficiency, the delay following positron implantation has to be carefully optimized in relation to the given experimental conditions (implantation energy, converter characteristics, etc.). There needs to be a way to adjust synchronization in real time.

Given this, what will the smallest time step to adjust be? Positronium is expected to leave the converter at a temperature within the range $100 \div 1000\,K$, $3.9 \cdot 10^4 \div 1.2 \cdot 10^5\ m\,/\,s$ in terms of velocity. Considering the worst case of a temperature around $1000K$, Positronium travels $1mm$ in $8.1ns$. A granularity of at least $8\,ns$ is thus desirable.

7.2 The need for active synchronization

In light of the above, we can conclude that an accurate clocking device to synchronize the Positronium accumulator with the Q-Switched laser is a prerequisite for the Positronium spectroscopy experiment. There are several other reasons why such a synchronization device is so critical to the apparatus:

1. As mentioned in Chapter 3, Q-Switched lasers have an internal clock rate that cannot be altered during runtime without damaging the power electronics. Laser light can be shot on the Positronium cloud only ten times per second at a precise pace.
2. The positron apparatus produces a signal when the bunch of positrons is ready and needs an external input signal to lower the potential gate, launching them. This input signal must be fed to the positron apparatus several hundred nanoseconds before the laser shoots on the Ps converter.
3. The overall jitter of the launch-implantation-formation-diffusion process must be much lower than the required timing precision to hit the cloud. Otherwise very few Positronium atoms would be hit, on average, by the laser pulse.

The purpose of the synchronization device is to provide the right timing for the launch signal both to the positron apparatus and to the laser, allowing the user to configure the delay in real time. The master laser clock is left unchanged during the whole operation: the positron trap waits to launch the bunch to meet laser timing needs.

7.3 Time scheme of the synchronization device

A final point about time specifications can be neatly summarized in the scheme below (Figure 7-1). Four signals are defined: the $10\,Hz$ master clock of the laser apparatus (internal), the signal from the positron apparatus that a bunch is ready inside the accumulator (input), and the two triggers (output) to the laser power supply and to the positron accumulator. The meaningful time durations are:

- $t_{\max}$: $220\,\mu s$ pulse duration to shoot a full-power laser impulse[8].
- t_d : critical delay time between the laser trigger and the positron trigger that needs to be adjusted in real-time to optimize the excitation efficiency. <u>This delay time can be negative</u>, i.e. the positron trigger may precede the laser trigger.

---

[8] see Chapter 5 for a reference about operating the EKSPLA laser with external triggering.

- t_p : $1\,\mu s$ pulse duration of the trigger signal to the Positronium accumulator.
- t_{off} : $1000\,\mu s$ pulse duration to discharge the capacitor pack on the flash lamp without sending a laser pulse.

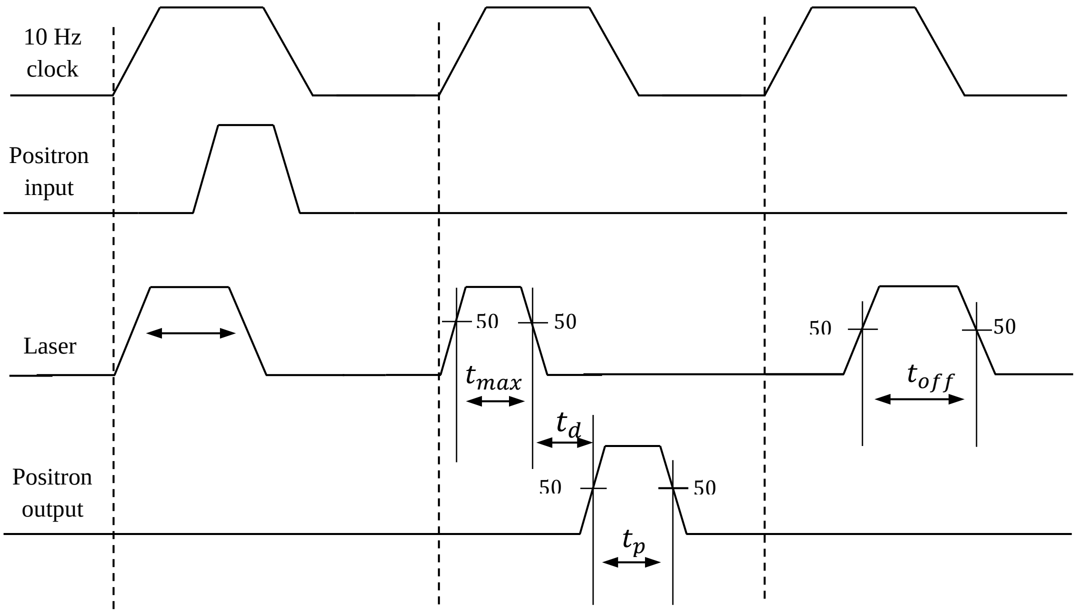

Figure 7-1: Functional time scheme of the synchronization device.

At the beginning, the laser operates in off mode, discharging the capacitor pack at the $10\,Hz$ rate without sending any pulse. At some point, a 'positron ready' signal is received asynchronously from the accumulator. The synchronization device then shoots the laser at full power at the next available $10\,Hz$ tick, at the same time transmitting the 'send positrons' signal to the positron accumulator with the correct timing to synchronize the Positronium cloud with the laser pulse in the experiment area.

7.4 Early prototype

An early implementation of the synchronization circuit was realized with discrete logic components, such as the widely known 74LSxx and 74HCxx series of integrated circuits including logic doors and monostable flip-flops. The prototype, described in [Ferri 2011], effectively reproduces the functional scheme of Figure 7-1. A minor drawback is the analogic regulation of the delay time between laser and positron trigger, which require an oscilloscope for continuous measurement of the delay time and the hand-setting of it, without trivial reproducibility.

7.5 Structure and operation of the device

The final design of the synchronization device presents several advantages over the prototype:

- **Digital device:** the delay value is stored in a digital manner, since in the final design the synchronization device is a fully digital device. This grants trivial reproducibility of the delay value, without the need of using an external oscilloscope to measure the delay every time a change is needed.
- **Re-programmability**: all core logic components are implemented in a programmable logic device, which can be re-configured simply flashing a different firmware via USB interface. No further hardware modification is needed.
- **Integrated design**: using of a commercial solution for the logic part of the device makes easier the maintenance of the device, whose structure is much simpler than the prototype.
- **Higher frequency:** components are rated for high-frequency usage up to $600\,MHz$: shorter rising and falling times are expected.

7.5.1 Overview

The final version of the synchronization device uses a complex programmable logic device (CPLD) as logic core of the circuit. CPLDs are smaller versions of FPGAs, integrated components that include a huge number of general purpose logic components which can be organized and wired together as required by the specific application. They can be programmed to implement any logic function made of logic doors and flip-flops, using a particular specification language called VHDL. Most of the CPLDs, as well as FPGAs, are suitable for high frequency operation thanks to their integrated design.

Differently from FPGAs, for which the device programming needs to be done every power up since all information about configuration and wiring (the *bitmask*) is stored in a volatile RAM memory, CPLDs include a non-volatile FLASH memory to store the bitmask. For this reason, CPLDs are more suitable for stand-alone applications, where the programming is done only once at the time of production. This is of course the case of the synchronization device.

A fast and inexpensive Xilinx CoolRunner-II CPLD, already installed on a development board by Digilent Inc., was chosen to implement all the logic part of the synchronization device. It features 256 logic macrocells, 118 user I/O pins and 600 MHz maximum switching frequency. Each macrocell can be configured to implement a high-level logic function, not differently from the lookup tables in FPGAs. A full explanation on how CoolRunner-II logic core works can be found in [XILINX 2013]. The master clock is provided by a custom 125 MHz quartz oscillator installed on the board.

The input/output signals are managed by a custom daughter card, plugged to the general purpose connectors available on the board called JMODs (see Figure 7-2 for a visual reference). A buffer integrated circuit converts the low-power 3.3V signals into 5V TTL signals suitable for driving a BNC cable. The daughter card also manages the power supply; a voltage-regulated circuit provides the 5V supply voltage both to the CPLD board and the buffer integrate.

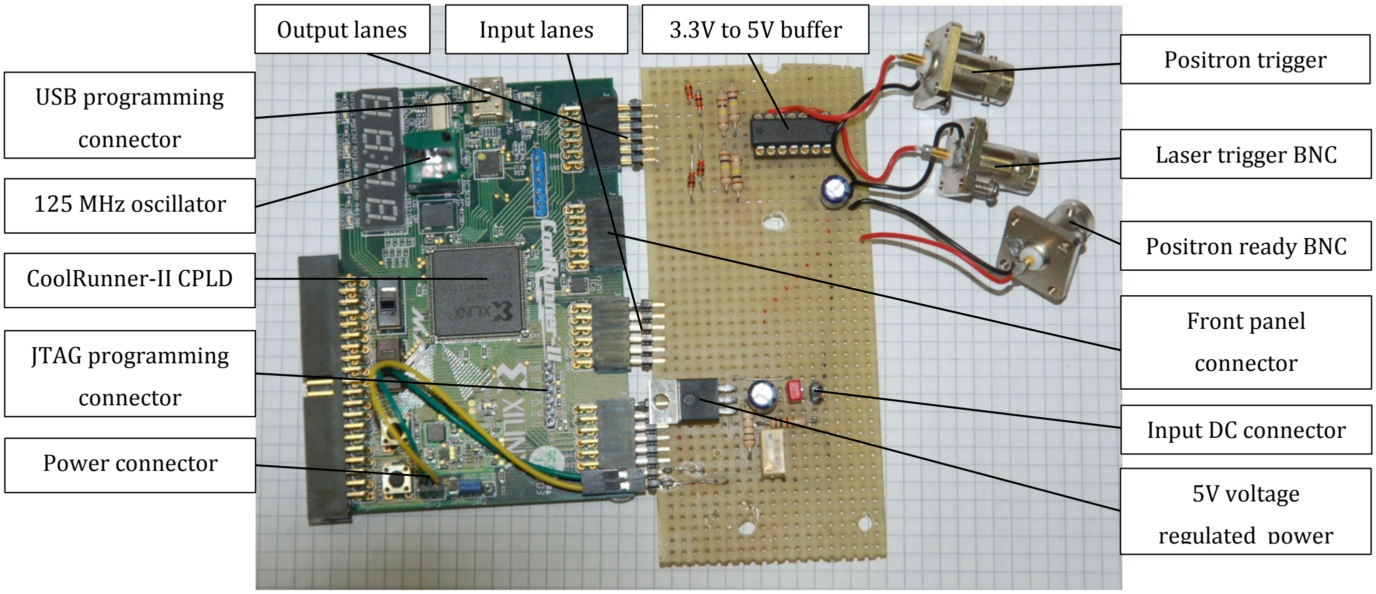

Figure 7-2: Photograph of the internal CPLD board (left) connected with the I/O daughter card (right). In the upper region of the daughter card the buffer integrate is clearly visible. In the lower region the voltage regulated power supply is present, feeding the CPLD board via the removable cables.

The synchronization device was then protected inside a metallic cover (Figure 7-3). The front panel of the box was modified to host a numeric display to show the current delay time and some triggers to change the delay time and laser operation mode, from maximum power mode to adjustment mode, as explained in the following paragraph.

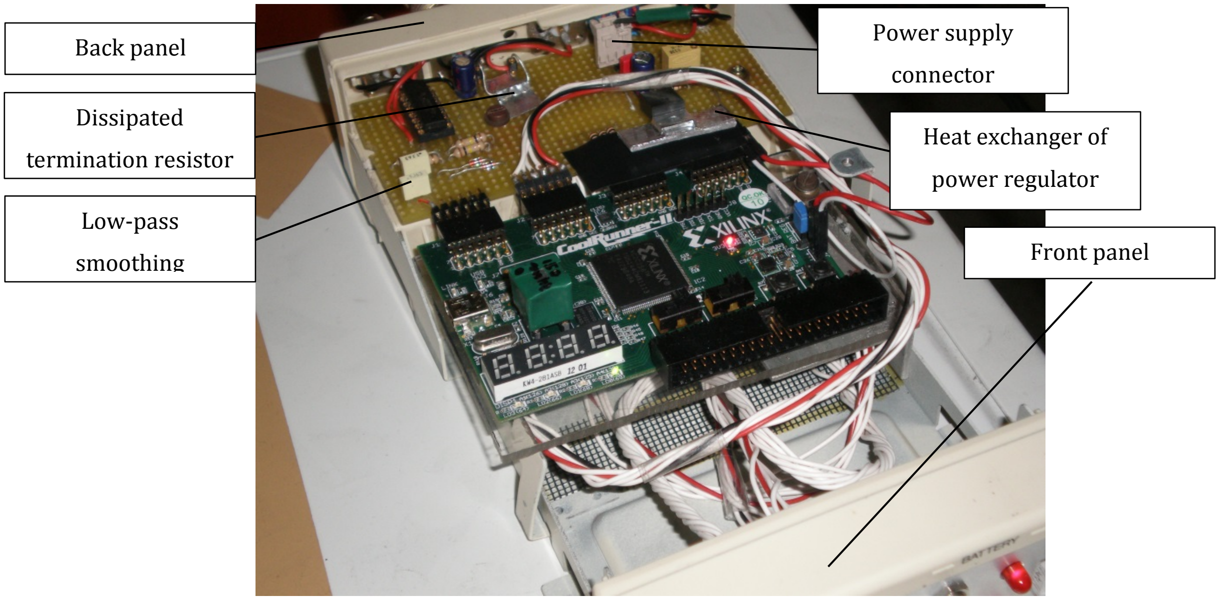

Figure 7-3: The synchronization device inside the metallic box.

7.5.2 Operating the device

The synchronization device operates with the logic described by the time scheme depicted in Figure 7-1. It provides triggering signals both to the laser power supply (that needs to be configured in external trigger mode before connecting the external trigger) and the positron trap with the correct time delay to send the laser pulses on the Positronium cloud at the exact time moment.

The device operates autonomously without the request of user intervention after it has been switched on and the time delay set on the front panel. The flash memory programming with the bitmask has been performed during this thesis work and doesn't need to be done again, unless a device malfunctioning is reported or an upgrade is found necessary. The programming can be performed directly via USB using Digilent Adept-2 software, or via a standard JTAG programmer connected to the black 6-pin jumper close to the power supply circuitry.

7.5.3 Connections

The synchronization device has all the connectors on the back side, including two BNC connectors for outputting the trigger signals and one BNC connector to receive the 'positron ready' signal from the positron accumulator (see Figure 7-4).

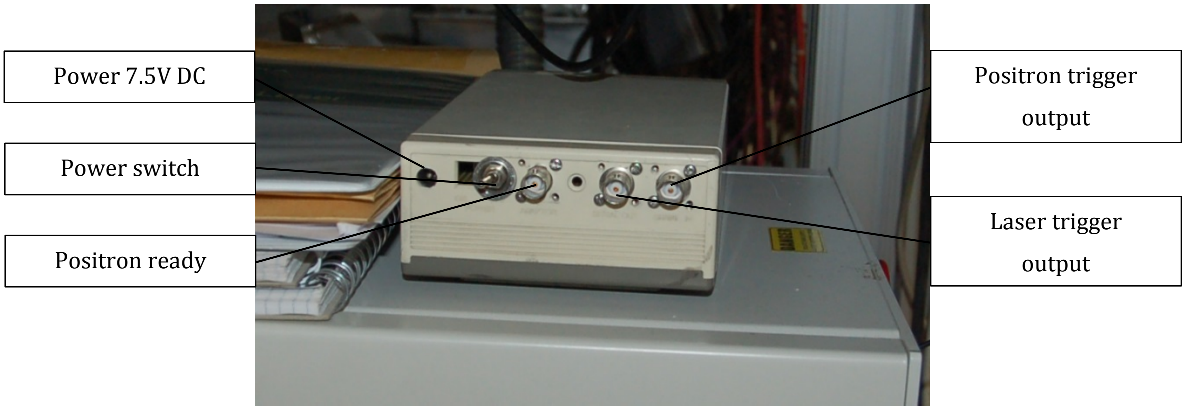

Figure 7-4: Back side of the synchronization device.

Recently, two sets of small wire connectors connect were added to connect the safety interlocks (one for the laser cover box and one for the laser hut tent) required by the safety regulations of CERN. The implementation of the safety interlock is described in the relative section, below.

7.5.4 Front panel

The front panel allows the user to change laser operation mode and read and set the delay time t_d between the falling edge of the laser triggering signal and the raising edge of the Positronium triggering signal. It includes the following components (see Figure 7-5):

- A seven segments display showing the current value for t_d in nanoseconds. This value can also be negative, i.e. the positron trigger signal begins before the end of the laser trigger signal.
- Two press buttons to increment/decrement the value of t_d by one step. Hold down the buttons to quickly increment/decrement the value.
- Two switches to set the current operation mode, as described in the following paragraph.

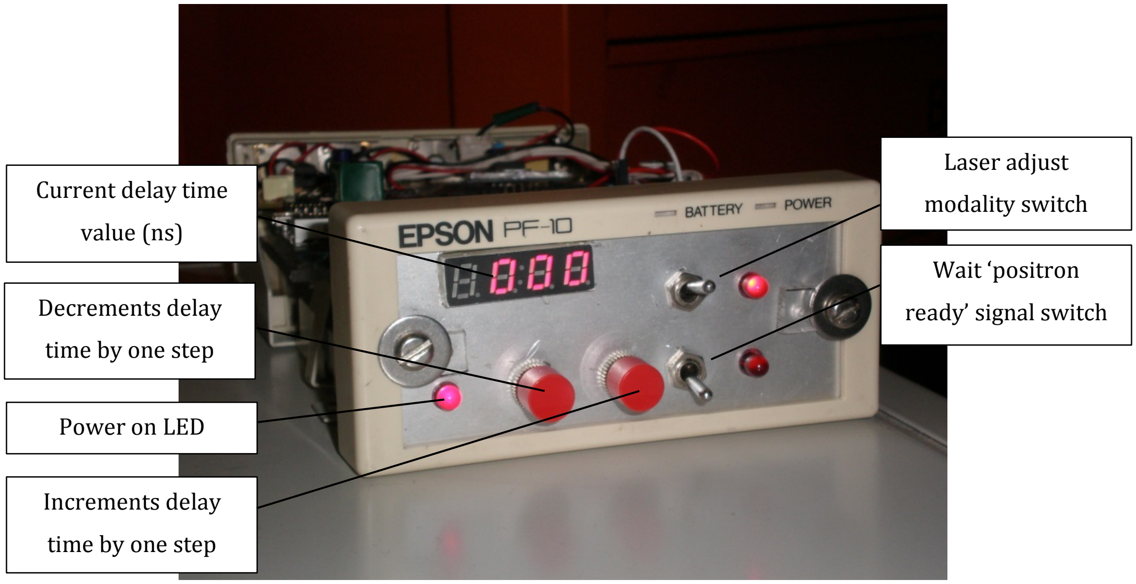

Figure 7-5: Front panel of the synchronization device showing the current delay time between the falling edge of the laser trigger signal and the raising edge of the positron trigger signal.

7.5.5 Operating modes

Once the synchronization device is turned on, the value of the delay time t_d is initialized to zero and the operation mode is read from the front panel triggers.

The upper laser switch, if enabled, tells the device to reduce the laser power to the adjust level to perform maintenance work. In adjust mode, no triggering pulse is sent to the positron apparatus.

The lower switch, if enabled, tells the device to wait for a signal on the 'positron ready' line before shooting the maximum power pulse, otherwise the laser is kept in off mode with the flash lamp working. If disabled, the triggering signal to the positron apparatus is sent continuously and the laser is kept at the maximum power.

The four possible operation modes are summarized in the following Table 5.

Operation mode	Adjust switch	'Positron ready' trigger enable switch	Laser mode	Positron trigger
Shoot continuously modality	OFF	OFF	Maximum power	Every laser pulse
Wait until ready modality	OFF	ON	No power, maximum power after 'ready'	At the next pulse after the 'ready'
Adjust modality	ON	OFF	Low power	None
Adjust modality	ON	ON	Low power	None

Table 5: Summary of synchronization device operation states, as defined by the two frontal switches.

7.6 Implementation details

In this section the details of the implementation of the CPLD synchronization device firmware are presented. The firmware is programmed (or more properly, specified) in VHDL, a high-level language to specify the logic elements to synthesize inside the CPLD. It is not the goal of this thesis to present VHDL in detail. There are both a wide literature on the matter and very good free tutorials available online, such as [PENN 2013].

In the following paragraphs, signal names will be highlighted using italic, for example *CLK_8MHZ*.

7.6.1 Logical structure

The synchronization device is articulated in the following tree of components:

- **CRTrigger:** the main components that defines the connections between the external pins and the internal sub-components. It implements the main temporization and the operation modes.
    - **24bit binary counter:** subcomponent used to generate the timestamp needed to synchronize all the events happening in the device.
    - **24bit signed adder:** subcomponent which calculates the sum between two signed 24bit integers, used to shift the timestamp of the beginning of the positron signal.
    - **24bit binary comparator:** subcomponent needed to compare two 24bit integer numbers.
    - **DigitalDelayLine:** custom VHDL subcomponent that takes care of introducing the delay time shorter than one clock cycle, if required, between the positron signal and the laser signal.
    - **NumDisplay:** custom VHDL subcomponent that handles the user I/O on the front panel, incrementing and decrementing the time delay value (which is stored as a number of nanoseconds) and displaying the current value to the numeric display. It manages also the conversion from binary digits, used internally, and decimal digits, used on the frontal display.
        - **SevenSeg:** custom VHDL subcomponent that converts four decimal numbers into electric signals to provide to the numeric display on the front panel to draw the four numbers. It also manages automatically the refresh of the displays.

7.6.2 Timing scheme

The main component, CRTrigger, receives the clock signal from the external $125\,MHz$ oscillator, *CLK_125MHZ*, and feeds it to a 24bit binary counter. The counter increments by one unity every clock cycle, generating a timestamp whereby synchronize all the events between a laser cycle and the following. The counter is reset to the initial value every $12,500,000$ ticks, corresponding to the laser repetition frequency of 10 Hz. Within the device code, all time measurements are given in counter tick units: for example, a $220\,\mu s$ time corresponds to $27,500$ counter ticks at $125\,MHz$. The internal signal corresponding to the current timestamp value (connected to the counter internal flip-flops) is called *SYNC_COUNTER*.

The reference counter is an effective solution to provide the programmable time delay. Delay is stored in flip-flops as a signed 24bit digital number expressing the number of nanoseconds from the falling edge of laser trigger signal (corresponding to Pockels cell switching) to the raising edge of positron trigger signal. A pulse is sent on the Ps line if the master counter reaches $27,500 + c_d$, where c_d is the time delay t_d expressed in tick units. The internal signal associated to c_d is called *POSIT_START*. A dedicated 24bit comparator subcomponent handles all the comparisons, like *SYNC_COUNTER == 27’500 + POSIT_START*, while a dedicated 24bit signed adder takes care of the sum/difference.

The reference timeline of the synchronization device including the conversion to tick units is shown in Figure 7-6.

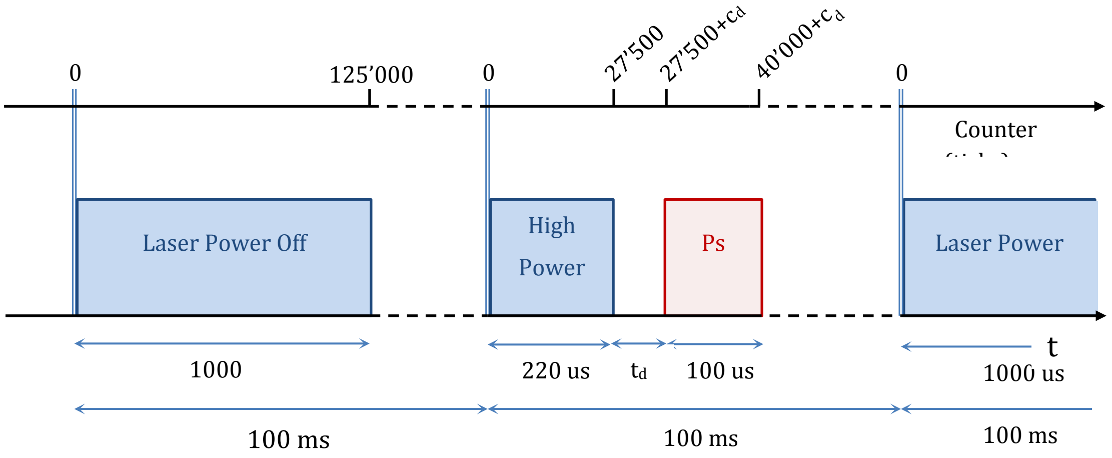

Figure 7-6: Example of synchronization of the pulses to the master counter providing the timestamp, in wait until ready operation modality.

7.6.3 Laser, positron, and input timing signals

Four different internal signals are produced with synchronous logic by comparing the current timestamp value, *SYNC_COUNTER*, with the relevant time delays (see *Chapter 5 – The AEGIS Q-Switched laser – External trigger operation*, for a discussion on the time delay values):

- ***LASER_FIRE***: this signal goes to ‘1’ when *SYNC_COUNTER == 0* and goes to ‘0’ when *SYNC_COUNTER == 27'500*. It’s the $220\,\mu s$ trigger pulse needed to shine the laser at the maximum power.
- ***LASER_LOW***: this signal goes to ‘1’ when *SYNC_COUNTER == 0* and goes to ‘0’ when *SYNC_COUNTER == 50’000*. It’s the $400\,\mu s$ trigger pulse needed to shine the laser at low power, suitable for adjustment operations with no risk of damaging the crystals.
- ***LASER_OFF****:* this signal goes to ‘1’ when *SYNC_COUNTER == 0* and goes to ‘0’ when *SYNC_COUNTER == 125’000*. It’s the $1000\,\mu s$ trigger pulse needed to discharge completely the active medium and don’t send a laser impulse at all.

- ***POSITRON_FIRE***: this signal goes to ‘1’ when *SYNC_COUNTER == 27’500 + POSIT_START* and goes to ‘0’ when *SYNC_COUNTER == 40’000 + POSIT_START*.
- ***ENABLE_INPUT***: this signal goes to ‘1’ for one clock cycle at some random point after *125’000* to avoid collisions with the current cycle. It enables the read of the frontal panel buttons to possibly change the value of *POSIT_START*.

These internal signals, after being stored in flip-flops, feed an asynchronous operation mode selector to produce the device output (described in the next paragraph). The only exception is *ENABLE_INPUT*, which is connected to a de-bouncer component that reads the state of frontal buttons only once per $100\,ms$ cycle to remove the signal fluctuations due to partial pressure of the buttons.

The VHDL code implementation of the described signal production is shown in Figure 7-7.

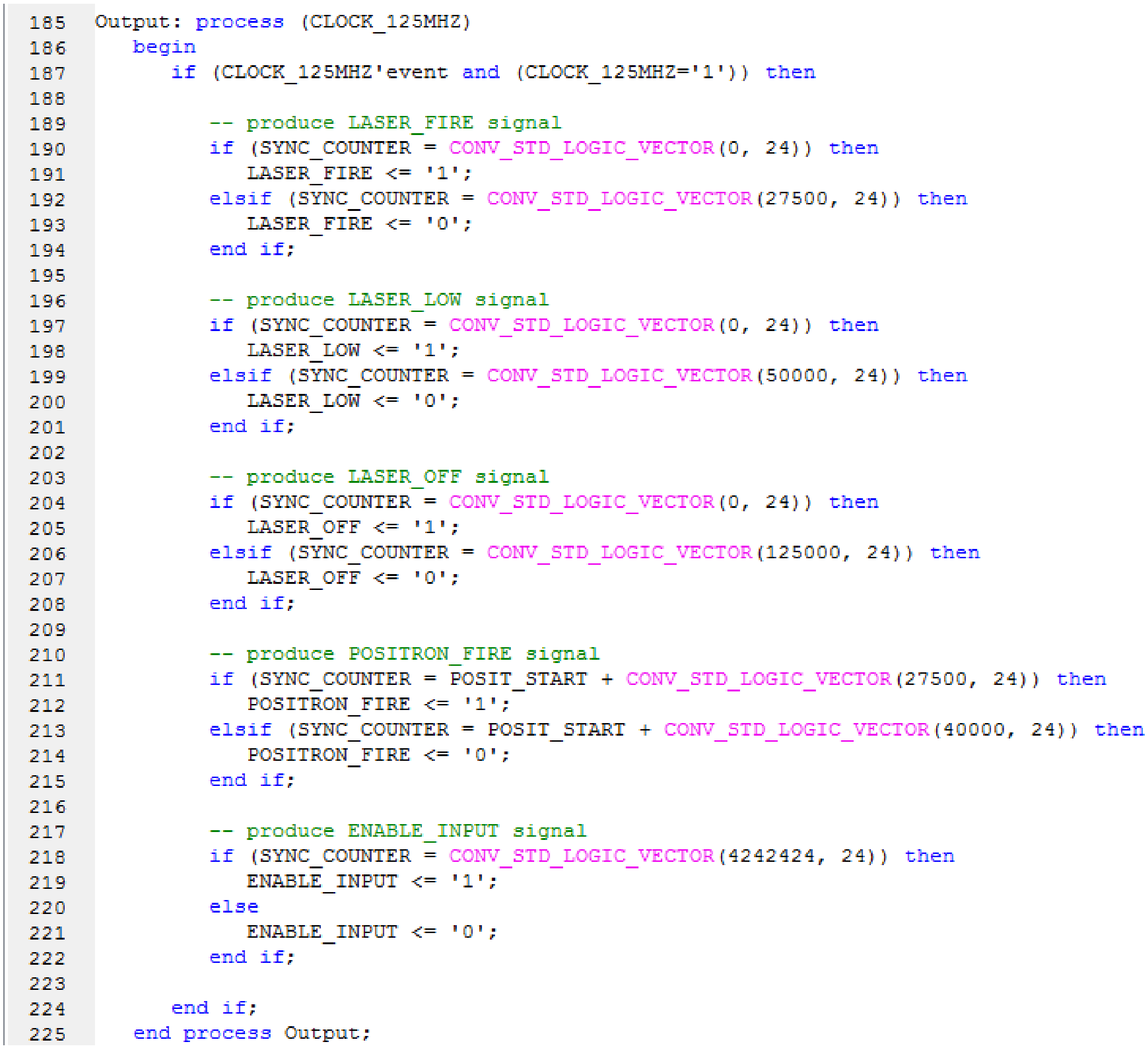

```
Output: process (CLOCK_125MHZ)
   begin
      if (CLOCK_125MHZ'event and (CLOCK_125MHZ='1')) then

         -- produce LASER_FIRE signal
         if (SYNC_COUNTER = CONV_STD_LOGIC_VECTOR(0, 24)) then
            LASER_FIRE <= '1';
         elsif (SYNC_COUNTER = CONV_STD_LOGIC_VECTOR(27500, 24)) then
            LASER_FIRE <= '0';
         end if;

         -- produce LASER_LOW signal
         if (SYNC_COUNTER = CONV_STD_LOGIC_VECTOR(0, 24)) then
            LASER_LOW <= '1';
         elsif (SYNC_COUNTER = CONV_STD_LOGIC_VECTOR(50000, 24)) then
            LASER_LOW <= '0';
         end if;

         -- produce LASER_OFF signal
         if (SYNC_COUNTER = CONV_STD_LOGIC_VECTOR(0, 24)) then
            LASER_OFF <= '1';
         elsif (SYNC_COUNTER = CONV_STD_LOGIC_VECTOR(125000, 24)) then
            LASER_OFF <= '0';
         end if;

         -- produce POSITRON_FIRE signal
         if (SYNC_COUNTER = POSIT_START + CONV_STD_LOGIC_VECTOR(27500, 24)) then
            POSITRON_FIRE <= '1';
         elsif (SYNC_COUNTER = POSIT_START + CONV_STD_LOGIC_VECTOR(40000, 24)) then
            POSITRON_FIRE <= '0';
         end if;

         -- produce ENABLE_INPUT signal
         if (SYNC_COUNTER = CONV_STD_LOGIC_VECTOR(4242424, 24)) then
            ENABLE_INPUT <= '1';
         else
            ENABLE_INPUT <= '0';
         end if;

      end if;
   end process Output;
```

Figure 7-7: VHDL implementation of the internal temporized signals to be fed to the operation modality selector.

7.6.4 Operation modes

The synchronization device offers currently three different operation modes, as described in Operation modes: shoot continuously mode, wait until ready modality and adjustment modality. Operation modalities, selected by the user with the frontal switches, are implemented within the synchronization device using simple asynchronous logic.

The most important input signal is *POSIT_READY*. This signal is stored in a reserved flip-flop to decouple the reading moment from the laser operation timeline. This is effectively a completely asynchronous signal with respect to the whole laser operation. It is set to ‘1’ when an event on the positron line is detected and is set to '0' when an impulse on the positron trigger line is sent. The flip-flop containing the value of *POSIT_READY* is read from the operation modality selector that decides whether to send an high-energy laser pulse or not.

Two other internal signals related to user inputs are produced when *ENABLE_INPUT* is set to '1'. The two frontal switches states are read in the same debouncer component used to read the frontal buttons, producing:

- ***INPUT_ENABLE_ADJUST_MODALITY****:* if 1, the operation modality is set to adjustment mode. Otherwise, the operation modality is left unchanged;
- ***INPUT_ENABLE_POSITRON_TRIGGER****:* if 1, the operation modality is set to wait until ready. Otherwise, the operation modality is set to shoot continuously.

These signals feed an asynchronous logic component, the operation modality selector, which produces the two output signals *LASER_OUTPUT* and *POSITRON_OUTPUT*. The selector, basically, is just a chain of AND logic doors to choose the correct laser signal and enable/disable the positron signal depending on the current operation modality state defined by *INPUT_ENABLE_ADJUST_MODALITY* and *INPUT_ENABLE_POSITRON_TRIGGER.*

Signal selection follows the same rules shown in Table 6.

INPUT_ENABLE_ POSITRON_TRIGGER	INPUT_ENABLE_ ADJUST_MODALITY	POSIT_READY	LASER_OUTPUT	POSITRON_OUTPUT
1	0	0	*LASER_OFF*	0
1	0	1	*LASER_FIRE*	*POSITRON_FIRE*
0	0	any	*LASER_FIRE*	*POSITRON_FIRE*
any	1	any	*LASER_LOW*	0

Table 6: Logic of asynchronous signal selection operated by the modality selector component.

The VHDL code implementation of the described operation modality selector is shown in Figure 7-8.

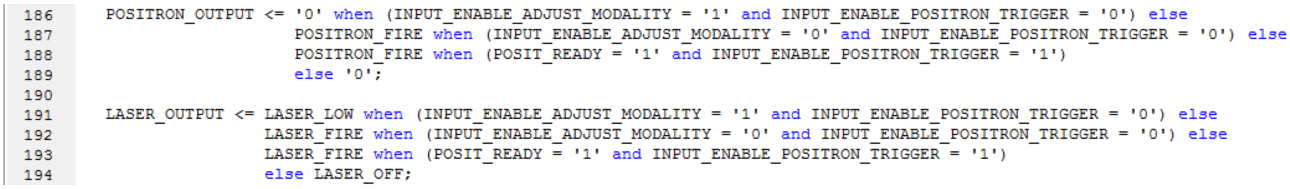

```vhdl
POSITRON_OUTPUT <= '0' when (INPUT_ENABLE_ADJUST_MODALITY = '1' and INPUT_ENABLE_POSITRON_TRIGGER = '0') else
                   POSITRON_FIRE when (INPUT_ENABLE_ADJUST_MODALITY = '0' and INPUT_ENABLE_POSITRON_TRIGGER = '0') else
                   POSITRON_FIRE when (POSIT_READY = '1' and INPUT_ENABLE_POSITRON_TRIGGER = '1')
                   else '0';

LASER_OUTPUT <= LASER_LOW when (INPUT_ENABLE_ADJUST_MODALITY = '1' and INPUT_ENABLE_POSITRON_TRIGGER = '0') else
                LASER_FIRE when (INPUT_ENABLE_ADJUST_MODALITY = '0' and INPUT_ENABLE_POSITRON_TRIGGER = '0') else
                LASER_FIRE when (POSIT_READY = '1' and INPUT_ENABLE_POSITRON_TRIGGER = '1')
                else LASER_OFF;
```

Figure 7-8: VHDL implementation of the operation modality selector, which produces device output signals from the internal temporized signals.

7.6.5 Increasing step precision down to 2 ns or even 1 ns

A technique to push the precision of the synchronization device down to $2\,ns$ time steps instead of $8\,ns$ was demonstrated during this thesis work, and a technique to reach the $1\,ns$ precision is currently under development. This is quite a remarkable achievement for a $600\,MHz$ -rated device. This technique may become useful in the future if the experiment requires more precision in shining the laser over the Positronium cloud.

The primary idea behind this improvement uses the three least significant binary digits in the delay time value as enable signals for three custom delay lines. If enabled, each delay line introduces $4\,ns$, $2\,ns$ or $1\,ns$ delays depending on the connected digit. Three tasks must then be accomplished:

1. Find a way to build a $4\,ns$ delay line;
2. Find a way to build a $2\,ns$ delay line;
3. Find a way to build a $1\,ns$ delay line;

The problem is then all around building the custom delay lines. $4\,ns$ and $2\,ns$ delay lines was addressed in the same way. It was observed that the time needed for a signal to leave the CPLD from one pin, reach the first pin on the closest JMOD connector, re-enter in the adjacent pin on the same JMOD and be read back by the CPLD is very close to $2\,ns$. Similarly, if the farthest JMOD connector is used and a piece of ~10 cm wire is added, this delay grows to $4\,ns$. This is a very simple but effective way to build the delay lines. For example, if a $6\,ns$ delay time is needed, the pulse is sent first to the farthest JMOD, then is read back by the CPLD, then is sent to the closest JMOD and finally is read back to the CPLD to be outputted from the master output.

Building a $1\ ns$ delay line is a trickier task. Different approaches are being tested, but only one gives satisfying results. The trick consists in conditioning the output signal on the value of a dummy input pin on the opposite side of the CPLD with respect to the output pin. This dummy input pin is forced to 0 via an external pull-down resistor. During VHDL design optimization, the software cannot known that the value of the input pin is fixed by outside, so it is forced to synthesize a long propagation line inside the CPLD to implement the conditioning logic operation, which introduces the time delay. This conditioning operation is performed only when the last digit of the delay time number is 1; in this way, no delay is introduced when the number is 0. The delay line is thus enabled by the last digit of the number. Practically, if the dummy input is set to zero, the conditioning operation is just a simple binary XOR (a simpler OR is more dangerous, because the synthesizer may decide to implement it via a wired OR).

With all such techniques combined together the synchronization precision was increased to $1ns$ with the bare CPLD board. Both $4ns$ and $2ns$ delay lines were thoroughly tested in the Milano laboratory and are ready to be implemented in the production device at CERN, which is currently still programmed with a $8ns$ time step. Differently, the $1ns$ delay line still requires further tests with the daughter board before being committed.

The present implementation in VHDL of the custom component to obtain a delay line with $1ns$ granularity is shown in Figure 7-9.

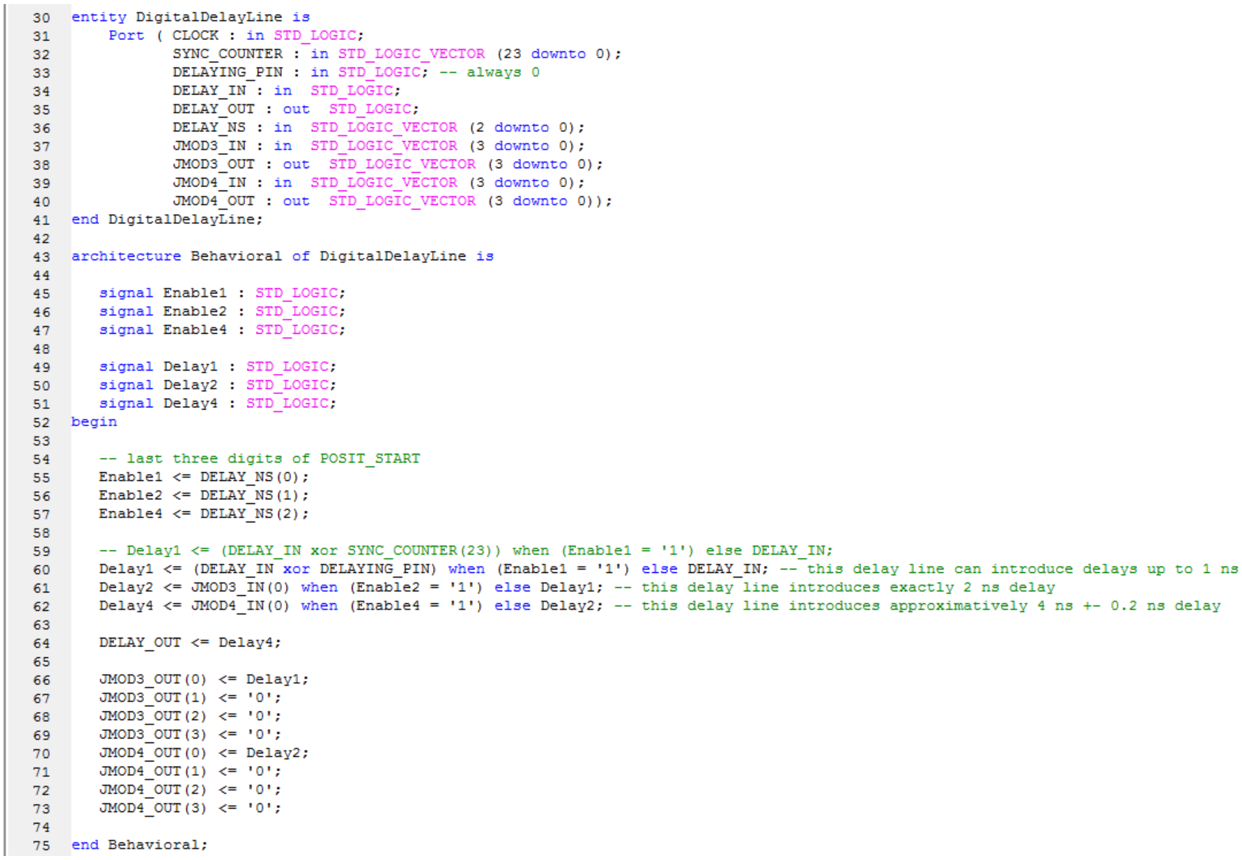

```vhdl
entity DigitalDelayLine is
    Port ( CLOCK : in STD_LOGIC;
           SYNC_COUNTER : in STD_LOGIC_VECTOR (23 downto 0);
           DELAYING_PIN : in STD_LOGIC; -- always 0
           DELAY_IN : in  STD_LOGIC;
           DELAY_OUT : out  STD_LOGIC;
           DELAY_NS : in  STD_LOGIC_VECTOR (2 downto 0);
           JMOD3_IN : in  STD_LOGIC_VECTOR (3 downto 0);
           JMOD3_OUT : out  STD_LOGIC_VECTOR (3 downto 0);
           JMOD4_IN : in  STD_LOGIC_VECTOR (3 downto 0);
           JMOD4_OUT : out  STD_LOGIC_VECTOR (3 downto 0));
end DigitalDelayLine;

architecture Behavioral of DigitalDelayLine is

   signal Enable1 : STD_LOGIC;
   signal Enable2 : STD_LOGIC;
   signal Enable4 : STD_LOGIC;

   signal Delay1 : STD_LOGIC;
   signal Delay2 : STD_LOGIC;
   signal Delay4 : STD_LOGIC;
begin

   -- last three digits of POSIT_START
   Enable1 <= DELAY_NS(0);
   Enable2 <= DELAY_NS(1);
   Enable4 <= DELAY_NS(2);

   -- Delay1 <= (DELAY_IN xor SYNC_COUNTER(23)) when (Enable1 = '1') else DELAY_IN;
   Delay1 <= (DELAY_IN xor DELAYING_PIN) when (Enable1 = '1') else DELAY_IN; -- this delay line can introduce delays up to 1 ns
   Delay2 <= JMOD3_IN(0) when (Enable2 = '1') else Delay1; -- this delay line introduces exactly 2 ns delay
   Delay4 <= JMOD4_IN(0) when (Enable4 = '1') else Delay2; -- this delay line introduces approximatively 4 ns +- 0.2 ns delay

   DELAY_OUT <= Delay4;

   JMOD3_OUT(0) <= Delay1;
   JMOD3_OUT(1) <= '0';
   JMOD3_OUT(2) <= '0';
   JMOD3_OUT(3) <= '0';
   JMOD4_OUT(0) <= Delay2;
   JMOD4_OUT(1) <= '0';
   JMOD4_OUT(2) <= '0';
   JMOD4_OUT(3) <= '0';

end Behavioral;
```

Figure 7-9: VHDL implementation of the custom delay line component, used to introduce a user-definable delay time with 1 ns granularity in time.

7.6.6 Safety issues

CERN safety regulations impose that any class-4 laser equipment must have two different protection systems to avoid the light shine in the environment with potential safety risk for people passing-by without protective glasses, even while an expert operator is working on the apparatus. This problem is usually addressed by building a protective box around the whole apparatus and an external hut in which the laser operator can stand while working on the open box. Both the box and the external hut have to provide an interlocking system to shut down immediately the laser if both the security systems are compromised at the same time.

The easiest and most effective way to fulfill these requirements was to add to the synchronization device two connectors on the back side, each of which connected to an interlocking system. It is very easy to implement a safety subcomponent that handles the interlocks. Simply, the laser signal is set immediately to *LASER_OFF* if both the interlocks are found open at the same time.

This solution is particularly effective because:

- Turns off the laser immediately, thus removing any safety risk;
- Stops the radiation without turning the laser completely off.

Leaving the laser active (but in OFF modality) both preserves the capacitor pack of the power supply if the stop is issued in the middle a pulse, preserves the flash lamp from an unnecessary thermal shock due to abrupt shutdown and eliminates the need to run the power-on procedure every time the interlock is opened.

7.7 Test and results

7.7.1 Quality of rising and falling edges

Rising and falling times were both measured using a fast oscilloscope to verify that the CPLD implementation of the synchronization device fulfills reasonable requirements about the slope of the edge. In order to perform these measurements, the oscilloscope was configured to trigger the sweep on the falling edge of the laser signal (corresponding to the switch of the Pockels cell) and record the raising edge of the positron signal. The delay time was set before to $0\,ns$.

The results are shown below in Figure 7-10. Both raising and falling edges exhibit high steepness in the point corresponding to half voltage.

$$\begin{aligned} m_{rise} &= 0.35 \pm 0.04 \ \frac{V}{ns} \\ m_{fall} &= 0.42 \pm 0.03 \ \frac{V}{ns} \end{aligned} \tag{7.1}$$

These values verify the validity of the high-frequency CPLD implementation on this matter.

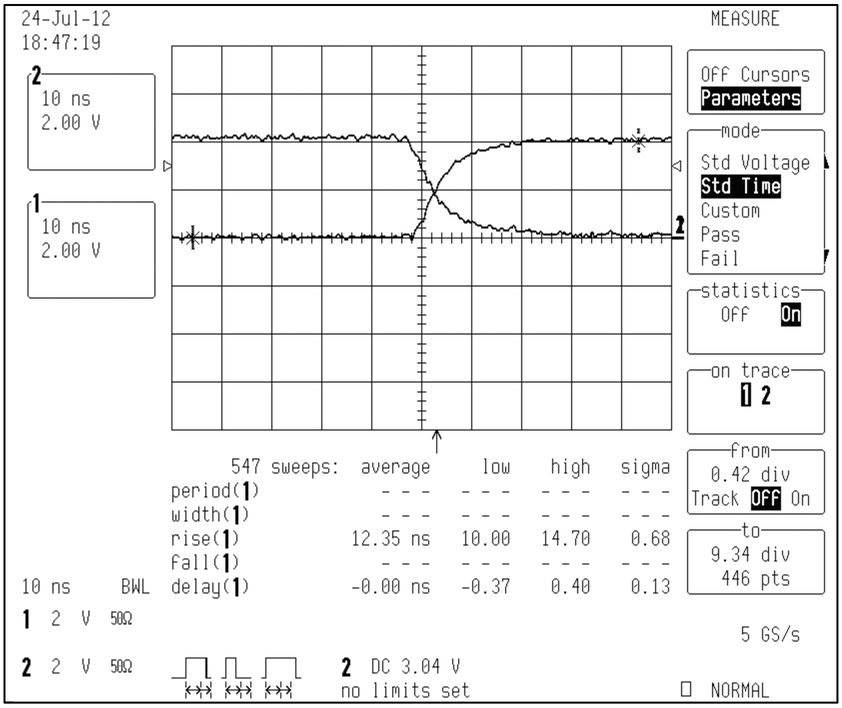

```
24-Jul-12
18:47:19                                              MEASURE

      547 sweeps:  average     low    high   sigma
period(1)            - - -    - - -   - - -   - - -
width(1)             - - -    - - -   - - -   - - -
rise(1)           12.35 ns    10.00   14.70    0.68
fall(1)              - - -    - - -   - - -   - - -
delay(1)          -0.00 ns    -0.37    0.40    0.13
```

Figure 7-10: Oscilloscope screen dump showing the falling edge of laser trigger signal and the rising edge of positron trigger signal. The delay time set on the front screen of the synchronization device was 0.

If required by the experiment, the rising and falling times can be reduced even more by substituting the present line driver integrate, which is a simple logic AND door – 74AC08 – able to drive a 5V TTL cable, with an faster 3.3V tolerant line driver, like for instance the 74LCX541 from Fairchild Semiconductor.

7.7.2 Synchronization capabilities

Having verified the stability in time of the rising and falling edges, it is now possible to assess the synchronization precision of the device. Both trigger lines were connected to a fast digital oscilloscope with two BNC cables of the same length to avoid measurement systematics. The delay time between the pulses was determined as a function of the delay time set on the front panel. Figure 7-11 shows the difference between the measured delay time and the ideal delay time set on the front panel; vertical error bars represent the fluctuation of the measurement. The measured delay time shows a systematic error within the range $0.4 \div 1.1 ns$ over the entire time interval, with a linear behavior with respect to the time set on the front panel.

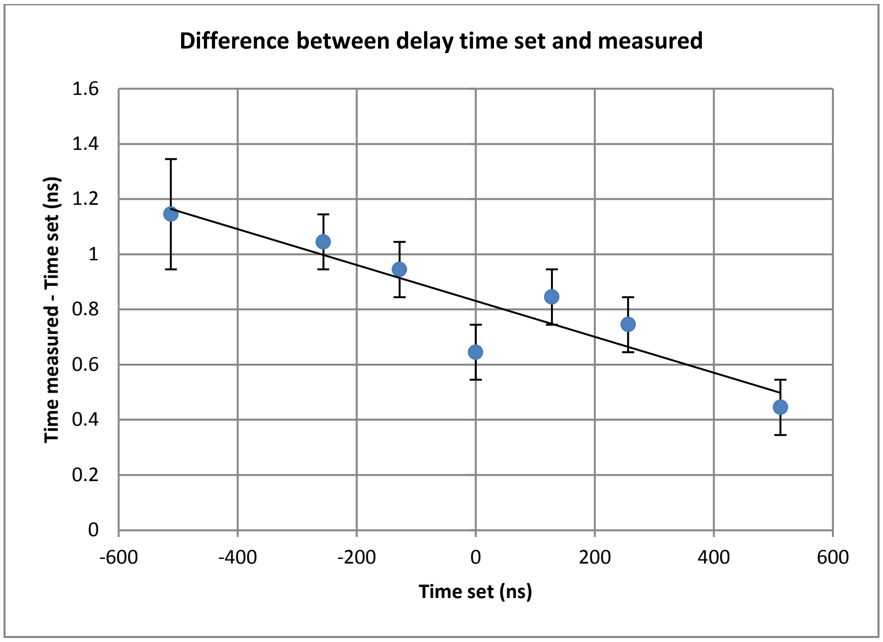

Figure 7-11: Difference between the measured delay time and the time set on the front panel, as a function of the time set on the front panel. In ideal conditions, a constant value of 0 is expected.

The systematic error is ~ 8 times smaller than the required precision of $8\,ns$ (see “Timing of Positronium production”), with an even smaller fluctuation in time. The average systematic error in determining the delay time for small values of $t_d \sim 0\,ns$ is

$$t_s = 0.83 \pm 0.11\,ns \tag{7.2}$$

It is already possible to conclude that both the synchronization precision and the fluctuation in time without external noise on the line are within the accepted range of precision needed to perform the experiment.

As a further development, it can be considered of carefully optimizing the VHDL code of the trigger to remove this systematic error in delay time, as described in the following paragraphs.

7.7.3 Testing laser synchronization

The last test performed with the synchronization device was the measurement of the delay time precision of the produced laser pulse. The laser trigger signal was connected to the laser power supply, while the positron trigger signal was connected to a fast oscilloscope on its external trigger line. A fast photodiode was placed in front of the $1064\,nm$ laser aperture. This configuration allows changing the delay time on the synchronization device and measuring the delay of the laser pulse with respect to the positron signal. It is expected to find a 1:1 linear dependency between delay times set on the device and measured from the photodiode.

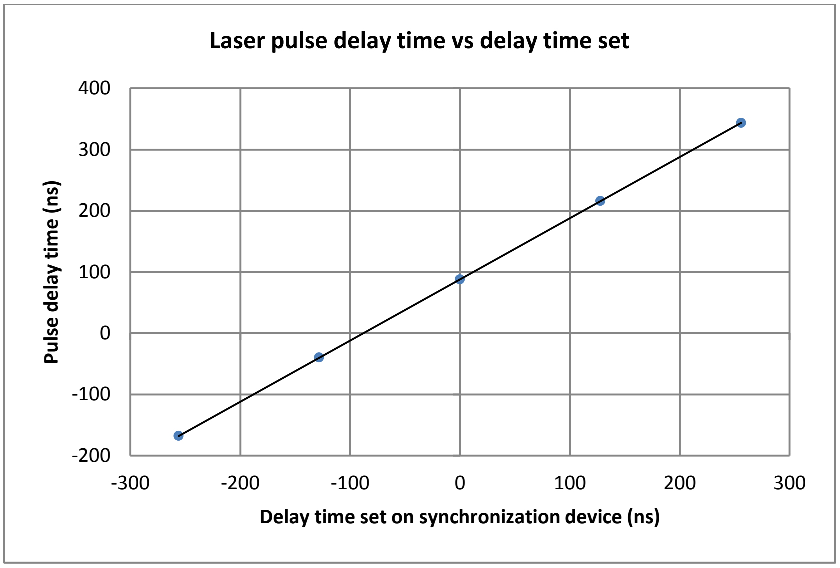

Parameter	Value
Fit model	$y = A + Bx$
A	87.895 ± 0.027
B	0.9991 ± 0.0015
R^2	1.0000

Figure 7-12: Delay time between reception of the trigger signal from the laser supply and detection of the laser pulse from the photodiode. Error bars are smaller than the marks.

In order to free the measurements from any setup dependency, the delay times were measured starting from the reception of the laser trigger signal by the laser power supply, instead of the sending by the synchronization device. In this way, the resulting delay measurements are independent of the cables chosen to interconnect the devices. Accurate measurements of the delays introduced by the cables were performed with more than 1000 oscilloscope sweeps, obtaining an overall $36.645 \pm 0.007\,ns$ to be removed from the data. Figure 7-12 shows the collected measurements with cable delays removed as a function of the time set on the synchronization device, together with the resulting parameters obtained by a weighed linear fit.

First of all, the angular coefficient of the line is compatible with the expected value of 1 within 0.6σ, meaning that the time step set on the device is the same obtained after the laser. Secondly, the accurate value of laser delay time from the trigger signal to the sending of the pulse can be obtained subtracting from the intercept the systematic error determined in the last section, (7.2).

$$t_{laser} = 87.07 \pm 0.11 ns \tag{7.3}$$

Finally, the average fluctuation of the sample (RMS) is constant over the whole dataset (i.e. is independent of the delay time set by the user), and is found to be

$$\delta t_{fluct} = 0.6 ns \tag{7.4}$$

7.8 Conclusions

In conclusion, the final design of the synchronization device shows very good performance in several scenarios:

- Good granularity of the time step, with $2 ns$ currently achieved and $1 ns$ under development;
- High accuracy setting the delay time (7.2), with a systematic error below $1 ns$;
- A very low overall fluctuation in time of the laser pulse (7.4).

The result obtained for the average fluctuation in time (7.4) is extremely important for the experiment. It states that the combination synchronization device-laser apparatus shows very little jitter in time, much below the $8 ns$ level required by the constraints. Fluctuation in time due to the laser equipment is thus negligible when it comes to synchronize it to the positron apparatus.

8 Conclusions and future prospects

This thesis centers on work to complete a pulsed laser apparatus based on a Q-Switched Nd:YAG cavity. The apparatus is expected to be used for a dedicated experiment about exciting Positronium to Rydberg levels in late 2013. The experiment, based on a two-step laser excitation scheme, will take place at the AEGIS experimental area in the AD building at the CERN laboratory near Geneva.

This is a part of the larger AEGIS antihydrogen experiment described in Chapter 2, currently being developed at CERN along with several other academic institutions throughout Europe, including the Universities of Bern and Zurich, the Max Planck Institute of Heidelberg, the INFN sections in Milan, Genoa, Pavia and Trento, and many others (see [AEGIS 2013], the complete list of institutes that make up the AEGIS collaboration). Positronium, the bounded system of electron and positron, is synthesized via a beam of positrons produced by the AEGIS positron apparatus and implanted, in the final layout of the experiment, in a silicon-oxide target, which acts as the Positronium converter. Shortly after the Positronium cloud is produced by the converter, two different laser pulses shine on it to stimulate, first, the transition from ground state to the excited level n=3 ($205\,nm$ wavelength)) and, then, the transition from n=3 to Rydberg levels (with wavelength in the range $1650 \div 1750\,nm$). This is an important experiment into the scarcely known spectroscopy of Positronium. Moreover, this is only the first step toward the final purpose of AEGIS, which is to produce antihydrogen through charge exchange, for gravity measurement.

The first part of this thesis, mostly theoretical, presented some elements of laser physics and the theory of Positronium excitation. An overview of laser physics and Q-Switched laser operation was given in Chapter 3. In particular, an analytical model for determining laser-pulse shape as a function of primary cavity parameters was developed. This analytical model proved its validity by fitting the shape of the real laser-pulse profile measured with a fast photodiode. It also allowed primary cavity parameters to be determined in a statistically robust way.

The theory of two-step Positronium excitation by a Q-Switched laser was then reviewed in Chapter 4, focusing on the aspects most relevant to the upcoming experiment.

Positronium's energy structure was described, focusing on its main contributions to energy-level splitting, as well as its expected lifetime at excited levels within 10% error. Analysis of the possible laser wavelengths involved and of the possible transition paths' efficiency led to the choice of a two-step transition scheme, first to n=3, then to Rydberg levels. The laser apparatus's energy requirements were reported. Finally, the measurement method to be used in the experiment was reviewed, analyzing the results obtained by previous experiments published in the literature.

The second part of this thesis concerns the laboratory activities to prepare the laser apparatus for the upcoming experiment. The first phase of experimental work, carried out at the Quantum Optics and Laser Laboratory at the University of Milan Department of Physics, consisted of completing and testing the laser apparatus, which had been planned and assembled in recent years (see [Chang 1985] and [Mills 2002]).

A detailed description of the laser apparatus's final configuration for normal operating conditions was given in Chapter 5. That description included results from several measurements performed on the apparatus to verify its functionality:

- pulse shape and cavity characteristics;
- pulse energies measured at the laser apertures as a function of pump power;
- energies and beam sizes of the secondary beams all around the breadboards;
- energy of the $205\,nm$ pulse produced;
- energy and wavelength of the $1650 \div 1750\,nm$ pulse produced as a function of crystal temperature.

The laser apparatus achieved expected performance in all these tests. Compared to the energy per pulse required to saturate both Positronium transition lines, $32\,\mu J$ for ultraviolet $205\,nm$ radiation and $350\,\mu J$ for infrared $1650 \div 1750\,nm$ radiation, the apparatus was able to provide $100\,\mu J$ of UV radiation and $2\,mJ$ of IR radiation within the range $1670 \div 1720\,nm$ under normal operating conditions. These pulse energies became $4.5\,mJ$ of IR radiation and $300\,\mu J$ at peak operating conditions, close to damage threshold of the frequency sum crystal. Results of several stress tests performed in Milan were reported, showing that both the frequency sum non-linear crystal and the laser flash lamp are subject to severe degradation during full-power operation, so future use of the apparatus at peak operating power must be limited to no longer than needed for the experiment.

The second phase of laboratory work was carried out at the AEGIS site at CERN. First, the experiment area was prepared to house the laser equipment, which was put in place at the beginning of November, 2012. The apparatus was then installed and commissioned, taking care to satisfy CERN security regulations, which included installing a cover box on the apparatus, raising a protection tent around the table, and set up an interlocking system on both box and tent. The planning and construction of the optical transport line was carried out at the same time as the commissioning, and it was installed in February, 2013.

Plans for the laser transfer line were described in Chapter 6, along with a review of the tests performed. Results showed that the transfer line meets expected synchronization requirements: UV pulse and IR pulse were found synchronized up to $1 ns$ in the position where the experiment is to take place. The expected energy loss for the current setup is 43%, corresponding to $57\,\mu J$ of UV under normal operating conditions, ignoring the factor 2 gain due to the last retro-reflecting prism. This leaves plenty of UV energy to saturate the transition from the ground state to n=3.

The issue of synchronizing the laser pulses with the apparatus that produces Positronium was also addressed during the Milan laboratory work, which led to devising the high-accuracy synchronization device described in Chapter 7. The device, based on a complex programmable-logic device (CPLD), was designed to allow the user – in real time – to advance or delay the formation of the Positronium cloud, as required by experimental conditions. It stores digitally the delay time, which can be adjusted by the user in steps down to $2\,ns$ during the final implementation. Moreover, it allows laser power to be reduced to preserve the frequency sum crystal and handles the interlocking system required by CERN safety regulations.

The synchronization device was tested both in Milan, where its output signals were analyzed with a GHz-class oscilloscope, and at CERN, where its ability to trigger the laser pulse was verified on the commissioned laser apparatus. Oscilloscope results show the synchronization device can synchronize the laser pulses to the positron trigger signal with an average error of $0.83 \pm 0.11 ns$ against the absolute value set on the front panel. This systematic error, although removable, is far below the required precision of $8 ns$.

However, this systematic error of the absolute value of the delay is not meaningful in the experiment context. Only the relative delay between two different values is significant: it corresponds to a different travel distance of the Positronium cloud. An accuracy estimate of relative delay time was given. The delay time of the laser pulse, measured with the fast photodiode, was fitted with a linear model with respect to the delay set on the frontal panel. The resulting slope coefficient calculated from the fit, 0.9991 ± 0.0015, is extremely accurate. For instance, adding $100 ns$ to the delay on the front panel would delay the laser pulse by $99.91 \pm 0.15 ns$, which is far more accurate than considering $0.83 ns$ as the ultimate precision bound.

Finally, the fluctuation in time of the laser pulses, with respect to the positron trigger signal, is found to be $0.6 ns$, which, in terms of distance traveled by Positronium, is $0.074 mm$. This is a remarkably low result for both the synchronization device and the high-energy Q-Switched laser apparatus, showing very little jitter in time.

We can conclude, thanks to the results achieved with the synchronization device and the transfer line, that the laser apparatus is ready for operation in the Positronium excitation to Rydberg levels experiment. Commissioning of the experiment will begin as soon as the experiment chamber is moved from the Trento laboratory to CERN, approximately May, 2013. The experiment will begin collecting data during the summer of 2013 and will continue throughout autumn and winter. For the duration, after graduating it is to be hoped, the author of this thesis will be involved in the experiment, operating the laser equipment to perform the two-step excitation of Positronium. After this experiment, the prospects for coming years include planning for the more ambitious goal of producing antihydrogen, bringing the dreamed-of “anti-“gravity measurements a step closer.

9 Bibliography

AEGIS Collaboration, *http://aegis.web.cern.ch/aegis/Collaboration.html*, excerpt of the website (2013).

AEGIS Collaboration, *Proposal for the AEGIS experiment at CERN Antiproton Decelerator* (2007).

ALPHA Collaboration, *http://alpha.web.cern.ch/*, excerpt of the website (2013).

ATHENA Collaboration, *http://athena.web.cern.ch/athena/*, excerpt of the website (2013).

ASACUSA Collaboration, *http://asacusa.web.cern.ch/ASACUSA/asacusaweb/main/ main.shtml*, excerpt of the website (2013).

Bethe H. A. and Salpeter E.E., *Quantum mechanics of one- and two-electron atoms*, Springer-Verlag, Berlin-Gottingen-Heidelberg (1957).

Cassidy D. B., Hisakado T. H., Tom H. W. K. and Mills A. P. Jr., Efficient production of Rydberg Positronium, *Physical Review Letters 108* (2012) 043401.

Castelli F. and Giammarchi M.G., *Proceedings of International School of Physics "Enrico Fermi"*, Società Italiana di Fisica, Varenna (2009).

Castelli F., *Notes on models for radiation-atom interaction*, unpublished (2013).

Cerchiari G., Master Thesis, unpublished (2013).

Chang E. S., Radiative lifetime of hydrogenic and quasi-hydrogenic atoms, *Physical Review A 31 (1)* (1985).

Cialdi S., Boscolo I., Castelli F., Villa F., Ferrari G., Giammarchi M. G., Efficient two step Positronium laser excitation to Rydberg levels, *Nuclear Instruments and Methods in Physics Research B 269* (2002) 1527-1533.

Close F., *Antimatter*, Oxford University Press, USA (2010).

Dirac P. A. M., The Quantum Theory of the Electron, *Proceedings of the Royal Society of London. Series A, Containing Papers of a Mathematical and Physical Character 117* (1928) 610-624.

Einstein A., On the Quantum Theory of Radiation, *Zeitschrift fur Physik 18 (121)* (1917).

Ferri F., *Progettazione e realizzazione di un sistema laser per l'eccitazione efficente del Positronio a livelli Rydberg,* Undergraduate Thesis, unpublished (2011).

Gidley D. W., Peng H. G., Vallery R. S., Positron annihilation as a method to characterize porous materials, *Annual Review of Materials Research 36 (49)* (2006).

Kellerbauer A. et al., Proposed antimatter gravity measurement with an antihydrogen beam, *Nuclear Instruments and Methods in Physics Research B 266* (2008) 351-356.

Mariazzi S., Bettotti B. and Brusa R. S., Positronium cooling and emission in vacuum from nanochanels at cryogenic temperature, *Physical Review Letters 104* (2010) 243401.

Mariazzi S., Bettotti B., Larcheri S., Toniutti L and Brusa R. S., High Positronium yield and emission into the vacuum from oxidized tunable nanochannels in silicon, *Physical Review B 81* (2010) 235418.

Mills A. P. Jr. and Leventhal M., Can we measure the gravitational free fall of cold Rydberg state Positronium? *Nuclear Instruments and Methods B 192 (1-2)* (2002).

ON semiconductors, *SN74LS00 datasheet* (2013).

PENN, *http://www.seas.upenn.edu/~ese171/vhdl/vhdl_primer.html*, excerpt of website (2013).

Philips semicondutors, *75HC4538 datasheet* (2013).

Pineda A. Soto J., Potential NRQED: The Positronium case, *Physical Review D 59* (1999) 016005.

Storry C.H. et al., First laser-controlled antihydrogen production, *Physical Review Letters 93* (2004) 263401.

Svelto O., *Principles of Lasers, fifth ed.,* Springer New York Dordrecht Heidelberg London (2010).

UCSD, *http://positrons.ucsd.edu/positron/trappingframe.html*, excerpt of the website (2013).

Villa F., *Laser system for Positronium excitation to Rydberg levels for AEGIS Experiment*, PHD dissertation Thesis (2010).

Villata M., CPT symmetry and antimatter gravity in general relativity, *Eur. Phys. Lett. 94* (2011) 20001.

XILINX Corporation , *http://www.xilinx.com/support/documentation/application_notes/ xapp376.pdf*, excerpt of website (2013).

Ringraziamenti

Questo lavoro non sarebbe mai stato possibile senza l'entusiasmo e l'onestà del grandissimo Marco Giulio, che ringrazio in modo sentito e profondo: promise che l'esperimento della spettroscopia sarebbe iniziato in Aprile, e così è stato.

Un caloroso ringraziamento a Fabrizio, per i preziosi auguri ricevuti all'1:29 del mattino del giorno di Pasqua.

Come non ringraziare Simone, che mi ha insegnato come si tirano le viti?

Per fortuna che Philip ha deciso di darmi una mano, altrimenti che fine avrei fatto con il mio povero e stiracchiato inglese?

Conosco la metà della collaborazione AEGIS solo a metà, e ringrazio meno della metà di loro solo metà di quanto meriterebbe: Sebastiano per non coltivare il suo *gruppo* di pecore, ma darsi ai giri in bicicletta, Martin per il pollo, il caballito e le partite di DotA, Luca il santo che mi ha mostrato che cosa sia veramente la pazienza, Francesco per la sua misericordia ed i suoi monarchi che parlano, Rafael per la sua papale parlantina, Daniel per i treni che non esistono, Sergio anche se non ho ancora capito cosa ci facesse li.

Ma soprattutto, tutti quanti per le (wait for it) MILLETRECENTOSESSANTAQUATTRO email in dodici mesi tondi tondi.

Come ogni bravo ciclista all'arrivo della tappa, non si manca mai di ringraziare la mamma, il papà e gli amici del bar sport. La lista sarebbe lunga e non vorrei scontentare nessuno. Ma un ringraziamento in particolare va a Giò per tutto l'aiuto nei mesi di lavoro.

... ah, dimenticavo, grazie anche a "i ginocchi" che ti mollano a una settimana dalla consegna.

Ruggero Caravita, Milano, 2 Aprile 2013